Signal Processing Advances in Radar-Based Identification and High-Accuracy Range Estimation

Zur Erlangung des akademischen Grades einer

DOKTORIN DER INGENIEURWISSENSCHAFTEN (Dr.-Ing.)

von der KIT-Fakultät für Elektrotechnik und Informationstechnik des Karlsruher Instituts für Technologie (KIT)

angenommene

DISSERTATION

von

M.Sc. Theresa Antes

Tag der mündlichen Prüfung: 26.06.2026

Hauptreferent: Prof. Dr.-Ing. Dr. h.c. Thomas Zwick
Korreferent: Prof. Dr.-Ing. Martin Vossiek

Zusammenfassung

Fortschreitende Automatisierung bedarf der immer detaillierteren Wahrnehmung und Interpretation der Umgebung durch autonome Systeme. Ein entscheidender Faktor ist hierbei die Identifizierung, sei es von anwesenden Akteuren, relevanten Objekten oder definierten Referenzpunkten. Radarsensoren finden verbreitet Anwendung im industriellen Kontext, inbesondere in autonomen Arbeitsumgebungen, die Möglichkeiten einer eindeutigen Objektidentifizierung sind jedoch begrenzt. Eine Kombination von Radaren mit Doppler Tags ermöglicht hingegen inherent Objektspezifität. Die Tags erweitern die Funktionsweise von Chirp Sequence Radaren um eindeutige Identifizierung bei hochgenauer Entfernungsschätzung und eröffnen neue Anwendungsoptionen aus dem Bereich der industriellen Automatisierung und darüber hinaus.
Den Kern dieser Arbeit bilden die Idee des Doppler Tags sowie eine umfassende Analyse der grundlegenden Eigenschaften, Spezifikationsanforderungen und anwendungsspezifischen Implementierung. Die Arbeit dient als initiale Machbarkeitsstudie für Radar-Doppler-Tag-Systeme mit Schwerpunkt auf Erkenntnissen und Entwicklungen in der Signalverarbeitung hin zu hochgenauen Entfernungsschätzungen. Doppler-Tags emulieren eine Doppler-ähnliche Frequenzverschiebung des Radarsignals und identifizieren so das markierte Objekt eindeutig. Auch unmarkierte Ziele sind im gesamten Sichtfeld des Radars detektierbar, da Störechos in der Signalverarbeitung unterdrückt werden und die Sensitivität der Hardware für Umgebungsreflexionen erhalten bleibt. Gleichzeitig wird die Schätzgenauigkeit deutlich verbessert. Tags liefern derweil zusätzliche Informationen über ihre zugehörigen Objekte. Die Frequenzverschiebung wird so aufgebracht, dass Tageinflüsse in zwei Seitenbändern enthalten sind. Durch deren Trennung und mathematische Neukombination stehen durch die Tags unverfälschte Signalkomponenten für nachfolgende Verarbeitungsschritte jenseits der Identifizierung zur Verfügung. Inbesondere erlaubt diese Kombination aus Hardware und Signalverarbeitung die Auswertung des ursprünglichen, laufzeitbedingten Phasenversatzes und damit eine hochgenaue Entfernungsschätzung zu markierten und unmarkierten Objekten ohne wesentliche Auflösungsanfor-

derungen.
Die genannten Funktionen werden zum ersten Mal simulativ und in Messungen mit Laboraufbauten sowie realitätsnahen Szenarien validiert. Doppler-Tags mit hochgenauer Entfernungsschätzung zeigen darin zuverlässig vielversprechende Ergebnisse für industrielle Anwendungen wie die räumliche Orientierung mobiler Systeme. Sie sind damit prädestiniert als vielseitige Bestandteile autonomer Umgebungen in einem breiten Spektrum aktueller und zukünftiger Anwendungen.

Abstract

Advancing automation requires autonomous systems to perceive and interpret their environment. A key factor is identification, whether of present actors, objects of interest, or defined reference points. Radar sensors are widely applied in industrial environments and particularly expedient in autonomous applications, however, their ability for unique object identification is limited. Where object specificity is crucial, Doppler tags enable this and unlock further potential of radar-tag systems. Not only do they extend chirp sequence sensing to include unique identification of multiple tags, but thereby enable new functionalities and widen radar applicability.

Herein lies the notion of this work – initially introducing the idea of Doppler tags and presenting comprehensive analysis about characteristics, specification challenges, and scenario-aware implementation. From the key focus on signal processing advances in highly accurate range estimation to exemplary demonstrations, it presents a fundamental feasibility study for radar-Doppler-tag systems with pinpoint accuracy. Doppler tags apply an artificial frequency shift to the radar signal, uniquely identifying the tagged object. Any part of the radar-visible surroundings is detectable, whereat tag responses contain additional information, from just a single quantity to tiered data. Clutter is suppressed in signal processing instead of hardware to enhance estimation accuracy but remain receptive. The Doppler tag applies a frequency shift such that any tag impact is comprised in two sidebands. Separating and recombining those allows for the retrieval of unimpaired signal components for subsequent processing steps alongside identification. Preserved delay-dependent phase-offset information from this complementary combination of hardware and signal processing particularly enables highly accurate ranging toward tagged and untagged objects without substantial resolution requirements.

These functionalities are demonstrated for the first time in simulations and validation measurements including expressive laboratory setups and close-to-reality scenarios. Doppler tags with high-accuracy range estimation therein evince reliable performance and promising characteristics for industrial app-

lications. They are hence predestined as versatile building blocks for robust, high-performance autonomous systems across a broad spectrum of emerging applications.

Acknowledgement

This thesis was created during my time as a research associate at the Institute of Radio Frequency Engineering and Electronics (IHE) at the Karlsruhe Institute of Technology (KIT).

Therefore, my first thanks go to Prof. Dr.-Ing. Dr. h.c. Thomas Zwick for giving me the opportunity to write this thesis and the scientific freedom to explore my ideas. He always encouraged me in my work and sent me around the world to get to know the groups next door. I would also like to thank Prof. Dr.-Ing. Martin Vossiek for his interest in my work and for accepting the co-lecture.

My heartfelt thanks to Benjamin Nuß, who always had an open ear for my questions and plenty of answers. Furthermore, I would like to thank Axel Diewald and Georg Gramlich for sharing an office and my musical atmosphere and Mario Pauli for the unicorn. I would like to extend this thanks to the whole radar team in its ever-changing composition for in-depth technical discussions, exchange of ideas, and countless types of cookies I got to try. In general, it is a pleasure to thank all my colleagues at KIT for making this time and the collaboration so wonderful and memorable.

My very special thanks to my parents, my brother, and my friends for supporting me wholeheartedly in achieving whatever goal I set. Above all, I would like to thank Jonas for everything he is to me and for sharing life.

Karlsruhe, May 2026

Theresa Antes

Declaration

The author declares that the findings reported in this work are the result of her original research. The manuscript's clarity and language have been enhanced with the assistance of AI-based tools, including generative AI.

Table of Contents

Abbreviations and Variables

Abbreviations

AoA	Angle of Arrival
AWGN	Additive White Gaussian noise
(P)CRLB	(Positioning) Cramér-Rao lower bound
CS	Chirp sequence
CZT	Chirp Z-transform
DFT	Discrete Fourier transform
FFT	Fast Fourier transform
FMCW	Frequency-modulated continuous wave
FoV	Field of view
GNSS	Global navigation satellite system
IFFT	Inverse fast Fourier transform
LNA	Low noise amplifier
LO	Local oscillator
mRTS	Miniature radar target simulator
(R)MSE	(Root) Mean square error
PA	Power amplifier

RCS	Radar cross section
RDM	Range-Doppler map
Rx	Receive
SINR	Signal-to-interference-and-noise ratio
SNR	Signal-to-noise ratio
STFT	Short-time Fourier transform
Tx	Transmit
USRP	Universal software radio peripheral
Wi-Fi	Wireless fidelity
2D	Two-dimensional
3D	Three-dimensional

Constants

$c_0 = 299\,792\,458\,\mathrm{m/s}$	Speed of light
$\exp = \mathrm{e} = 2.71828\ldots$	Euler's number
$\mathrm{j} = \sqrt{-1}$	Imaginary unit
$k_\mathrm{B} = 1.380649 \cdot 10^{-23}\,\mathrm{m^2\,kg/(s^2\,K)}$	Boltzmann constant
$\pi = 3.14159\ldots$	Pi

Latin Symbols and Variables

Lower Case Letters

a	Auxiliary distance used in A.2
b_{R}	Range bin index
b_{D}	Doppler bin index
c	Speed of light in medium
d	Object dimension
f	Frequency
f_{s}	Sampling rate
i	Summation index
i, j	Matrix indices
k	Time step index
m	Chirp index
n	Sample index
$\mathbf{p}_{\mathrm{r}}$	Radar position, $\mathbf{p}_{\mathrm{r}} \in \mathbb{R}^3$
$\mathbf{p}_{\mathrm{i}}$	Reference position, $\mathbf{p}_{\mathrm{i}} \in \mathbb{R}^3$
r	Auxiliary distance used in A.2
s	Signal
s_{R}	Signal after range DFT
s_{D}	Signal after Doppler DFT
t	Time
u	Reduction factor
v	Target velocity
w	Number of CZT iterations
z	Zero-padding factor

Upper Case Letters

A	Signal amplitude
B	Sampled bandwidth
$\mathbf{C}$	Covariance matrix
CL	Conversion loss
E	Expected value
F	Noise figure
G_{P}	Processing gain
$G_{\mathrm{tx/rx}}$	Transmit/Receive antenna gain
$\mathbf{I}$	Identity matrix
$\mathbf{I}_{\mathrm{F}}$	Fisher information matrix
$\mathbf{J}$	Jacobian matrix
L	Loss factor
N_{c}	Number of chirps
N_{it}	Number of iterations
N_{s}	Number of samples
P	Power
P_{n}	Noise power
R	Target range
R_0	Initial target range
R_{f}	Frequency-based range estimate
R_{φ}	Phase-offset-based range estimate
R_{fin}	Combined $f\varphi$ range estimate
T	Sampled chirp duration
T_{cr}	Chirp repetition time

Greek Symbols and Variables

α	Object orientation angle
β	Auxiliary angle used in A.2
γ	Auxiliary angle used in A.2
Γ	Equivalent noise bandwidth
δ	Error
Δ	Resolution
ε	Measurement uncertainty
η	Input SNR
$\boldsymbol{\theta}$	Parameter vector
ι	System temperature
κ	Auxiliary angle used in A.2
λ	Wavelength
Λ	Step size
$\boldsymbol{\mu}$	Mean vector used in A.1.1
ν	Refractive index
ϱ_{t}	Target RCS
σ^2	Noise variance
σ_{I}^2	Interference variance
τ	Signal delay
τ_0	Initial signal delay
Υ	Cross-term variables used in A.1.2
φ	Phase offset
φ_{st}	Random start phase
Φ	Signal phase
Ψ	Cross-term variables used in A.1.2
ω	Complex AWGN

Operators and Mathematical Symbols

$\tilde{\cdot}$	Sampled value
$\hat{\cdot}$	Estimated value
$\bar{\cdot}$	Mean value
$\lvert\cdot\rvert$	Absolute value
$\lVert\cdot\rVert$	Euclidean norm
$\lfloor\cdot\rceil$	Rounding function
$(\cdot)^*$	Hermitian conjugate
$\mathcal{N}$	Gaussian distribution
$\mathfrak{R}$	Real part
$\mathbb{R}^3$	3D Euclidean space
Bold symbols	Vectors or matrices

General Indices

az	azimuth
A / B / C	associated to tag A / B / C
b	beat
D	Doppler
DT	Doppler tag
el	elevation
id	identification
lin	linear
max	maximum
min	minimum
rx	receive

set	setpoint, denoting a nominal value
tx	transmit
ua	unambiguous

1 Introduction

Radar (radio detection and ranging) is long since more than just detection and ranging. Building on Hülsmeyer's basic idea of detecting objects and estimating their parameters [Hül04a, Hül04b], applications evolved from air monitoring over automotive adaptive cruise control to industrial and even consumer products. Radars can be used wherever non-contact measurement systems are required. They offer distinct advantages, particularly in challenging environmental conditions, due to their resilience to visual interference, including but not limited to dust, smoke, and occlusion. Given adequate hardware and signal processing, radar sensors inherently provide information about the object distance, relative velocity, azimuth and elevation angle, and radar cross section (RCS). Thereby, they offer promising estimation capabilities for spatial awareness and precise movement. However, identifying the object to which these parameters belong uniquely is beyond the capabilities of classical radars.

1.1 Idea and Motivation

In complex and crowded scenarios with multiple objects, unique identification is crucial to pinpoint the object of interest among several targets, correctly assign parameter estimations, and use them effectively. Current development is driven by radar properties like multi-parameter estimation and environmental robustness and particularly enhanced by performance features such as high accuracy in range estimation. The latter can be accomplished through signal processing, however, without simultaneous resolution enhancement if the radar configuration remains unchanged, imposing limitations to the separability of objects. Unique object identification resolves ambiguities and allows for the differentiation of objects despite insufficient resolution. In combination, highly accurate ranging to an identified object is favorable for multiple and even essential for some applications. It forms the basis for tasks in the context of

automation, human-machine interaction, and generally Industry 4.0 but also for applications in autonomous driving, medical imaging, or augmented reality [VS20, SSSW17, KHJH88, NHS24]. Particularly the industrial and medical sectors benefit, where identification and localization of certain objects of interest are crucial [DVC+17]. Radar sensors provide the required information to determine object positions and trajectories and are commonly used in corresponding applications such as tracking or monitoring [WZZ+21, LJLC17]. Concomitant identification opens new fields of applications where radar sensors provide extensive information about the environment and thereby deliver the data basis for advanced tasks wherever the autonomy of systems or subsystems is intended.
Radar-based identification, however, requires extensive knowledge about the surroundings to infer from the estimated parameters to the object itself. Radar tags are a compelling alternative interoperating with radar sensors and enabling the identification of tagged objects. Different fields of application give rise to correspondingly different, and in some cases mutually exclusive, requirements. A variety of tag technologies is hence available, aiming at various applications with different characteristics. Thereby, tailored approaches improve performance and avoid unnecessary complexity.

This work introduces a new tag concept - the Doppler tag. The focus is on unique object identification and highly accurate range estimation with moderate hardware requirements. The concept includes an advanced signal processing chain and corresponding hardware that is tailored precisely to the intended functionality and processing, enabling identification and pinpointing of a tag while simultaneously being receptive to untagged surroundings. The tag emulates the Doppler phenomenon and, by using different identification frequencies, allows for unique identification of tagged objects with conventional radar hardware. It is designed for operation with chirp sequence (CS) radars, which are, alongside the related frequency-modulated continuous wave (FMCW), the standard in industrial radar applications. They are already used in a multiplicity of tasks in this context such as distance measurement, hidden object detection, or positioning [ASB+15, SRB+07, VRH99]. Using CS, a newly developed phase analysis in addition to standard processing provides highly accurate range estimation without high bandwidths. Simultaneously, tags allow for object identification and differentiation even in scenarios with targets unresolvable in range and velocity. They are read at once without requiring multiple access schemes, which eliminates blind times and makes them well-suited for multi-tag settings. Compact

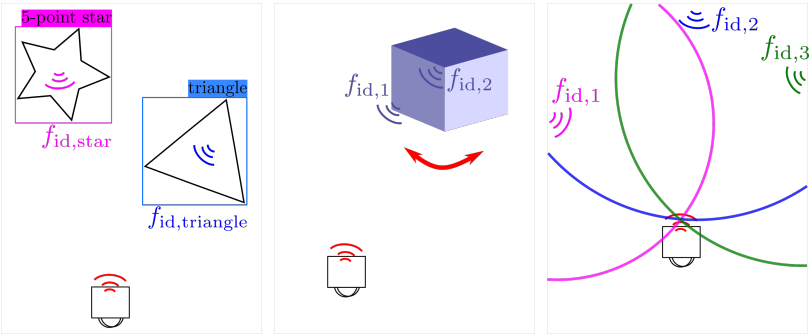

(a) (b) (c)

Figure 1.1: Application examples for Doppler tags in an industrial context, including object identification (a), orientation estimation (b), and self-positioning (c).

and low-cost fabrication allows for mass application. Classical radar sensing is not impaired and can be applied to both tagged and untagged objects. Therein, surroundings are only suppressed during tag processing but remain available for untagged object detection. Doppler tags thus provide a comprehensive overview of the radar environment, encompassing both identified tag markers and sensing information about the surrounding area.

This allows for a whole range of possible applications, all of which exploit specific features of Doppler tags with pinpoint ranging. A robot independently identifies tools or objects to proceed with (Fig. 1.1a), using the high accuracy of range estimation to precisely grab and handle them, while classical radar sensing equips it with an overview of its surroundings, enabling further sensing and collision avoidance. When approaching a Doppler tag, wake-up functionalities allow for the start of object-specific sensing or processing tasks. Unmodified radar hardware offers subsequent functionalities, for which the tag provides a trigger. Even the orientation of an object of interest can be determined (Fig. 1.1b) and support handling, as an autonomous arm that is supposed to pick up an object must know its exact orientation in order to avoid errors or damage. The accuracy of range estimation to multiple, uniquely distinguishable tags enables robust and reliable (self-)positioning (Fig. 1.1c) so that the robot can autonomously navigate through its surroundings without optical markers or guiding wires. Recalibration processes are streamlined by approaching a Dopp-

ler tag at a known position and pinpointing the distance, thereby eliminating the need for time-consuming manual recalibration.

1.2 State of the Art

The most widely used tag concept for radar at present is the harmonic tag, enabling the identification of objects otherwise hidden or showing insufficient RCS to be differentiated from the surroundings [CB04, PMC+08, SL10, GSBLL13, HBBP21]. These tags not only require the tag hardware but also a tailored radar transceiver, differing from common hardware by a frequency multiplication between transmit and receive paths. With a few exceptions, e.g., [NVN20], simultaneous radar sensing of tagged and untagged objects is not possible with these radars, which impedes a comprehensive supervision of complex scenarios. Furthermore, tags can only be distinguished from their environment but not from each other, as typically a single harmonic frequency is evaluated. Hence, differentiation of multiple tagged objects and, therefore, real identification is not possible using harmonic tags. For this reason, harmonic tags are well-suited to detect and potentially track a specific kind of target, but not for overall monitoring of intricate environments as often demanded in an industrial setting.
Similar to harmonic tags, other principles of clutter-suppressing tags are discussed, enabling identification and radar sensing solely for tagged objects [SHK+21, KXW22, TE00]. Active and passive reflector tags of different architecture are considered in [SE11, SBH+22] and [WMB+93, ISN+23]. Similarly, passive, frequency-coded landmarks are proposed, e.g., in [JSSEA+20] and [AAZAK22]. In [BSCB04], a radar tag to enhance detection and circumvent the minimum detectable velocity of a pulsed radar is introduced.

Another approach are code-based tags, which combine identification and radar sensing with the exchange of information about the object. Modulated backscattering tags enable, e.g., communication with FMCW [COTKR15] or synthetic aperture radars [FPEA+18]. In [DHC+17], the proposed active tag is introducing a frequency shift with binary phase shift keying modulation to the reflected signal. Switching between modulation frequencies allows for communication. A similar approach is proposed in [SFH+17], also enabling communication via frequency switching. At first glance similar to introducing an artificial Dopp-

ler, the shift is considerably higher than motion-caused Doppler shifts that are mimicked with the Doppler tag, so that coupling terms become significant and impair range estimation.
In [VG08], a switched injection-locked oscillator is utilized as active transponder, providing a response signal similar to that of a Doppler tag. However, the transponder function differs fundamentally from a Doppler tag, as do the ways information is encoded in the response signal and the radar processing required to extract it.

Beside radar tags, a variety of tag technologies not relying on radar, such as the widely used barcode, is available. They all come with their own tag and corresponding reader architecture. Most tag technologies only offer identification, but a number of wireless techniques are under investigation also for ranging. The mostly targeted application is indoor positioning, e.g., with wireless fidelity (Wi-Fi), Bluetooth low energy, ultrasound, ultra wideband, and radio frequency identification (RFID) [BCL+14, BD03, DAMC+15, AOJRT24, SN11]. All approaches come with dedicated advantages and limitations and particularly accuracies differ significantly, ranging from sub-centimeters to meters, dependent on the used positioning technique and system design. A comprehensive overview is given, e.g., in [VWG+03].
Some technologies, such as Wi-Fi, utilize existing nodes, hence requiring little to no additional hardware effort. They are of particular interest if an additional communication channel is sought for. As a drawback, most systems require synchronization between transmitting and receiving nodes and multiple tags are not actually read at the same time, but one after the other in quick succession. Camera-based systems partly even follow a tagless approach [MT11], but require preliminary information about the surroundings and are sensitive to lighting conditions.

Therefore, all technologies come with characteristics tailoring them for certain applications, and so does the Doppler tag. It is structurally different from the aforementioned radar tags as it exploits the Doppler phenomenon for identification and, using a customized processing chain, benefits from several inherent radar features despite tag influence. The accurate range estimation, not reached yet with other tag concepts, allows for new applications such as orientation estimation. No specialized radar transceivers are required, thus both tagged and untagged objects are detected with a single radar and comparable accuracy. The simultaneous functionality for multiple tagged and untagged objects provides

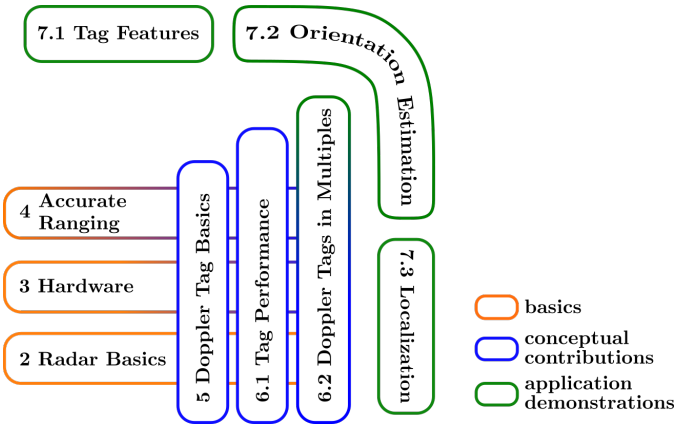

Figure 1.2: The structure of this work builds on the basics of radar, existing hardware, and extended signal processing approaches for enhanced estimation accuracy. The central contributions are the Doppler tag introduction and its combination with highly accurate ranging. Performance evaluation and exemplary application demonstrations complete the work. The given numbering corresponds to the chapters.

a flexible system for monitoring. It is hence a promising concept for various fields of application and for in-depth investigation.

1.3 Objectives and Structure of this Work

The objective of this work is to introduce Doppler tags with highly accurate range estimation, from the basic idea to exemplary applications. The Doppler tag is developed from scratch, based on the objectives of a tag allowing for unique identification and highly accurate ranging to tagged and untagged objects with simple tag and conventional radar hardware. Although hardware implementations are developed and discussed, emphasis is placed on signal processing. Thereby, this work is a signal processing perspective on current challenges in the field of radar and forms the basis for customized developments. It demonstrates signal processing in advanced radar applications and showcases possibilities beyond complex hardware solutions.

The work discusses the Doppler tag idea, its combination with accurate ranging, its implementation, and exemplary application as well as requirements and limitations of the proposed approach. Basic considerations and conceptual contributions span the space for advanced applications as visualized in Fig. 1.2. Well-known radar basics are given (Ch. 2) to allow for the comprehension of subsequent concepts and the used radar hardware as well as reference systems are introduced (Ch. 3). Required preparatory work (Ch. 4) comprises the development of a signal processing chain for highly accurate range estimation using a CS radar and a thorough analysis of occurring bin effects. This processing is extended to dynamic setups and appropriate bounds for the estimation accuracy in relevant scenarios are derived. On the basis of this foundation, the Doppler tag concept is introduced (Ch. 5) and fundamental principles are investigated. The complete processing chain and considerations for multiple tags are elaborated. Guidance is provided on application-specific tag design and two different hardware realizations and their applicability within this work are presented. The performance of radar-tag systems is validated in static and dynamic scenarios and with multiple tags (Ch. 6) to highlight characteristics and features of the Doppler tag. This demonstrates the ability of operation without hardware modifications to existing CS radar platforms, the elimination of tag-induced artifacts through complex-domain processing, and the feasibility of employing double-sideband mixing for accurate range extraction. Collectively, these attributes simplify system integration and reduce the overall complexity while achieving outstanding accuracy. Exemplary applications are realized (Ch. 7) with Doppler tags in different functions, which convey an impression of the versatility of these tags. Finally, a conclusion summarizes the achievements of this work (Ch. 8).

Through these objectives, the work at hand seeks to establish both the technical contributions and the practical relevance of the proposed Doppler tag approach. It is a fundamental applicability study for the entire concept with a strong emphasis on original algorithms for highly accurate range estimation. Doppler tags can become a versatile building block for robust, high-performance monitoring systems across a broad spectrum of emerging applications and advance the applicability of radar-tag systems with highly accurate range estimation to new functionalities.

2 Radar Principles

Radar, introduced in the early 20th century, describes the original idea of detection and localization of objects using radio waves. Radar terminology starts with the patent of Christian Hülsmeyer 1904, discussing a maritime radar, although major developments enabling this technology were achieved prior. From military deployment during World War II, radar evolved finding applications in various fields such as air traffic control, weather forecasting, maritime navigation, and autonomous driving. From its military origins, radar has become an indispensable tool in civilian and scientific domains, continually pushing the boundaries of detection and monitoring.

This chapter addresses the theoretical fundamentals of radar including the classical signal processing approach following chapters will build upon. Starting from the radar range equation, which is valid for all types of radar, subsequent derivations focus on CS radar. A generic signal model and corresponding signal processing steps are presented, which enable the estimation of target range and velocity. Finally, the resolution and measurement region of a CS radar are discussed.

2.1 Radar Equation

Radar detection is based on emitting electromagnetic waves and analyzing the reflected signals to determine the presence, distance, and speed of targets. The basic functionality is quantified in the radar equation (2.1), assuming far-field conditions [Lud98].

The radar sensor transmits an electromagnetic wave, eventually of certain modulation, in direction of an object to be detected. The wave is reflected at the target and received back with the power

$$P_{\mathrm{rx}} = \frac{P_{\mathrm{tx}} G_{\mathrm{tx}} G_{\mathrm{rx}} \lambda^2}{(4\pi)^3 R^4} \varrho_{\mathrm{t}}, \tag{2.1}$$

where P_{tx} denotes the transmitted power, $G_{\mathrm{tx/rx}}$ the transmit/receive antenna gains, λ the wavelength of the transmitted wave, R the distance between radar and target, and ϱ_{t} the RCS of the target [Göb01].

2.2 Chirp Sequence Radar

Regarding modulation, CS is the prevailing standard in industrial radar applications and focused on hereinafter. However, the introduced approaches are mostly not limited to CS but applicable to other radar modulation schemes as well.
CS is a derivative of the classical FMCW approach, consisting of a single chirp of millisecond duration. FMCW is most suitable in single-target scenarios and can only cope with moving targets to a limited extent, which highly limits the field of possible applications. CS radars transmit multiple chirps of shorter duration, hence they are also referred to as fast chirp FMCW. Doppler analysis is performed over consecutive chirps, which, to some extent, decouples range and Doppler estimation and enables the separation of multiple targets in range and velocity while preserving a similar processing gain.

CS radars transmit a continuous signal consisting of multiple chirps of linear frequency slope as depicted in Fig. 2.1. The same chirp configuration is assumed for all chirps hereinafter, although variations are possible and implemented for specific applications [Ala25]. Considering a saw-tooth modulation, the phase of a single chirp is determined from the required linear frequency course by integration:

$$\Phi_{\mathrm{tx}}(t) = 2\pi \int_0^t f(t')dt' = 2\pi \left(f_{\min} t + \frac{B}{2T} t^2 \right) + \varphi_{\mathrm{st}} \tag{2.2}$$

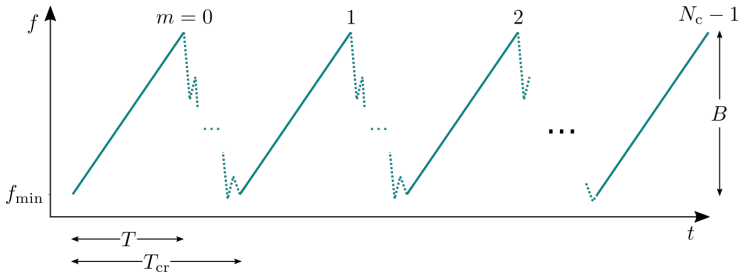

Figure 2.1: CS radar signal in saw-tooth modulation, consisting of N_c chirps of bandwidth B.

The chirp starts at a frequency f_min and covers a bandwidth B with N_s samples of accumulated duration T. Consecutive chirps differ solely by their random start phase φ_st caused by the reset to f_min between chirps. This phase cancels out in the beat signal allowing a steady phase to be assumed between subsequent chirps $\Phi(T, m) = \Phi(0, m+1)$, neglecting discontinuities between the chirps during idle times. The phase of the complete transmit signal is determined to

$$\Phi_\mathrm{tx}(t, m) = 2\pi \left(f_\mathrm{min} t + \frac{B}{2T} t^2 + \left(f_\mathrm{min} + \frac{B}{2} \right) mT \right), \tag{2.3}$$

for a signal consisting of N_c chirps, where $m \in [0, N_\mathrm{c} - 1]$ denotes the slow time index, and $t \in [0, T]$ the fast time. The first two summands describe the current chirp, while summands depending on m describe past chirps.
Following propagation through free space, the signal is reflected off a target and received by the radar. The phase of the received signal is thus time-shifted with respect to the phase of the transmitted signal by the delay τ as

$$\Phi_\mathrm{rx}(t, m) = \Phi_\mathrm{tx}(t - \tau, m). \tag{2.4}$$

This delay is dependent on the initial target range R_0, hence

$$\tau_0 = \frac{2R_0}{c}, \tag{2.5}$$

and the relative velocity of the target v. Assuming the latter to be constant, the time-dependent delay $\tau(t,m)$ is

$$\tau(t,m) = \frac{2R(t,m)}{c} = \tau_0 + \frac{2v}{c} \cdot (t + mT)\,, \tag{2.6}$$

where c is the speed of light in free space and negative relative velocity $v < 0$ describes a target approaching the radar.
Transmitted and received signals are mixed to form the beat signal, which is subsequently low-pass filtered and discretized. The phase of the beat signal is given using (2.3), (2.4), and (2.6):

$$\begin{aligned}
\Phi_\mathrm{b}(t,m) &= \Phi_\mathrm{tx}(t,m) - \Phi_\mathrm{rx}(t,m) \\
&= 2\pi\Bigg(\overbrace{\left(\frac{B}{T}\tau_0 - \frac{2v}{c}\frac{B}{T}\tau_0 + f_\mathrm{min}\frac{2v}{c}\right)t}^{\text{Range estimation}} \\
&\quad + \overbrace{\left(\frac{2v}{c}f_\mathrm{min} - \frac{2v}{c}\frac{B}{T}\tau_0\right)mT}^{\text{Doppler estimation}} \\
&\quad + \left(\frac{B}{T}\frac{2v}{c} - \frac{B}{T}\frac{4v^2}{c^2}\right)tmT \\
&\quad + \left(\frac{B}{T}\frac{2v}{c} - \frac{B}{T}\frac{2v^2}{c^2}\right)t^2 \\
&\quad + \left(-\frac{B}{T}\frac{2v^2}{c^2}\right)(mT)^2 \\
&\quad + \overbrace{\tau_0\left(f_\mathrm{min} - \frac{B}{2T}\tau_0\right)}^{\text{Phase offset } \varphi_\mathrm{b}} \Bigg)
\end{aligned} \tag{2.7}$$

The first term contains the range information in the τ_0-dependency along t. Using the second term, the Doppler information can be extracted from the v-dependency along m. Both terms contain range-Doppler coupling, offsetting one quantity in dependency of the other one as range and Doppler are not completely separated [Fit74]. The third term describes range Doppler migration. Due to its motion, the range of the target is migrating over multiple range

bins during a single measurement. As the Doppler shift is dependent on the increasing instantaneous frequency during a chirp, the detected Doppler is migrating over multiple Doppler bins. The fourth term describes the movement of the target during one chirp, which also affects the range, however, to a minor extent. A corresponding behavior cannot be observed for the Doppler domain, hence the fifth term only contains the squared velocity dependency over multiple chirps. The last term independent of t and m is a constant phase offset, which is omitted in classical ranging, but will be exploited for highly accurate range estimation in Ch. 4. In this form, the signal model represents solely the part of the signal that is sampled and used for signal processing. This is the case when both the transmit and receive signals are present for mixing, while beginning and end of the ramp are omitted, hence $\tau \ll T$ and $B \ll f_{\min}$.

Finally, the beat signal is given by

$$s_{\mathrm{b}}(t,m) = \exp\left(\mathrm{j}\Phi_{\mathrm{b}}(t,m)\right), \tag{2.8}$$

disregarding the signal amplitude.

2.2.1 Classic Signal Processing

For the classic signal processing, the beat phase is reduced to

$$\Phi_{\mathrm{b}}(t,m) \approx 2\pi\left(\frac{B}{T}\tau_0 \cdot t + \frac{2v}{c} f_{\min} \cdot mT\right) \tag{2.9}$$

using

$$\begin{aligned} v &\ll c \\ B &\ll f_{\min} \\ \tau_0 &\ll T. \end{aligned} \tag{2.10}$$

After dechirping, the beat signal is low-pass filtered and discretized with the sampling rate f_{s}, resulting in

$$\Phi_{\mathrm{b}}(n,m) \approx 2\pi\left(\frac{B}{N_{\mathrm{s}}}\tau_0 \cdot n + \frac{2v}{c} f_{\min} \cdot mT\right), \tag{2.11}$$

with $t \rightarrow \frac{n}{f_\mathrm{s}}$, where n is the sample index, and $N_\mathrm{s} = T \cdot f_\mathrm{s}$.

Frequency-based Range Estimation

The information about the target range is contained in the frequency of the beat signal which corresponds to the difference of the instantaneous frequencies between the transmit and receive signal and hence to the time delay. To extract the frequency, a discrete Fourier transform (DFT) is applied to the signal along the fast time t:

$$\begin{aligned} s_\mathrm{R}(b_\mathrm{R}, m) &= \sum_{n=0}^{N_\mathrm{s}-1} s_\mathrm{b}(n, m) \cdot \exp\left(-\mathrm{j}2\pi b_\mathrm{R} \frac{n}{N_\mathrm{s}}\right) \\ &= \exp\left(\mathrm{j}2\pi \frac{2v}{c} f_\mathrm{min} m T\right) \cdot \sum_{n=0}^{N_\mathrm{s}-1} \exp\left(\mathrm{j}2\pi (B\tau_0 - b_\mathrm{R}) \frac{n}{N_\mathrm{s}}\right), \end{aligned} \tag{2.12}$$

with the range bin index $b_\mathrm{R} \in [0, N_\mathrm{s} - 1]$. The behavior of this term can be approximated with a sinc-function whose maximum carries the range information of the target as

$$\widehat{R}_0 = b_{\mathrm{R}_\mathrm{max}} \cdot \frac{c}{2B}, \tag{2.13}$$

with $b_{\mathrm{R}_\mathrm{max}}$ being the index of the maximum in the discrete range spectrum. This classical processing approach is henceforth referred to as frequency-based range estimation.

Frequency-based Doppler Estimation

The relative velocity between target and radar is estimated from the phase shift over the chirps. To extract this phase shift, a second DFT is applied along the slow time index m:

$$s_\mathrm{D}(b_\mathrm{R}, b_\mathrm{D}) = \sum_{m=0}^{N_\mathrm{c}-1} s_\mathrm{R}(b_\mathrm{R}, m) \cdot \exp\left(-\mathrm{j}2\pi b_\mathrm{D} \frac{m}{N_\mathrm{c}}\right), \tag{2.14}$$

with the Doppler bin index $b_{\mathrm{D}} \in [0, N_{\mathrm{c}} - 1]$. As for the range estimation, a sinc-function can be used to approximate the behavior of (2.14) and the Doppler shift is determined from its maximum to be

$$\widehat{f_{\mathrm{D}}} = \frac{b_{\mathrm{D}_{\max}}}{N_{\mathrm{c}} T_{\mathrm{cr}}} \tag{2.15}$$

and

$$\widehat{v} = \widehat{f_{\mathrm{D}}} \frac{c}{2 f_{\min}} = \frac{b_{\mathrm{D}_{\max}} c}{N_{\mathrm{c}} T_{\mathrm{cr}} 2 f_{\min}}, \tag{2.16}$$

with $b_{\mathrm{D}_{\max}}$ being the index of the maximum in the discrete Doppler spectrum and T_{cr} the chirp repetition time.
More detailed derivations of the classical signal processing for CS radar, also including angle of arrival estimation and other measures, can be found, e.g., in [WBG25].

Both DFTs add signal processing gain according to the DFT length (N_{s} in range and N_{c} in Doppler), enhancing the target detectability. In general, processing gain is considered any improvement in the signal-to-noise ratio (SNR) achieved through coherent processing methods. The full processing gain of CS is comparable to that of FMCW as two short DFTs are applied instead of a single long one. If, however, only a single DFT is applied, e.g., to estimate the Doppler shift, the processing gain is reduced and target detectability deteriorates. Signal processing techniques to preserve the full processing gain in case of only a single DFT are discussed in Ch. 4.
Within this work, all DFTs are implemented as fast Fourier transforms (FFTs) according to [FJ98] and, hence, denoted as such.

2.2.2 Limitations

Depending on the radar parameterization, different limitations arise with regard to its achievable accuracy, resolution, and measurement regions. It is important to strictly distinguish between resolution and accuracy. The resolution of a radar is defined as its ability to separate two objects and cannot be improved solely through signal processing. Accuracy, however, describes the degree of closeness of estimated quantities to their true values and can be augmented through adequate processing techniques [RSH10].

The maximum unambiguous value of a parameter is the highest possible determination that can be obtained without introducing ambiguity in its interpretation. It is to be distinguished from maximum values, in excess of which detection or parameter estimation is not possible anymore. These limitation measures are subsequently discussed for CS radar.

Accuracy

Accuracy is defined in the ISO 5725-1:1994 norm to be a measure for the closeness of a test result to the accepted reference value. According to this definition, accuracy is a combination of trueness and precision. Trueness rates the error in a test procedure and is expressed as a bias, that is to be minimized. It is the systematic component of the accuracy. Precision is the random component, that depends solely on the distribution of random errors and does not relate to the true value. It is expressed as variation or standard deviation of the test result. [ISO94]

Three accuracy measures are used within the scope of this work:

- Repeatability: describes precision under repeatability conditions. This term is specified as uni- and bidirectional repeatibility for motorized stages.
- Relative accuracy: accuracy gained in relative measurements relying on each other for reference.
- Absolute accuracy: accuracy gained in calibrated measurements, referring to a reference system.

It should be noted that the relative accuracy primarily assesses the stability of the range estimation rather than its absolute accuracy. Thereby, it isolates the internal consistency of the system from calibration and external (reference) uncertainties, which form an own field of research and are not investigated in detail within this work. In the ideal case of a perfectly stable system with a constant and well-characterized bias, relative and absolute accuracy coincide after proper calibration. However, calibration is not applied for most measurements as highly accurate calibration is challenging and the relative accuracy provides meaningful information about the intrinsic estimation behavior, independent of

calibration uncertainties.
As a measure of accuracy, range error and variance or standard deviation are predestined as they represent the two constituents of accuracy. Zero range error is optimal and aimed at, indicating unbiased estimation. For the variance, the Cramér-Rao lower bound (CRLB) is a qualified theoretic limit. It assumes an unbiased estimator, thus maximum trueness, and defines a lower limit for the precision, what makes it applicable to rate the overall achievable accuracy of a system. Scenario specific CRLB derivations are given in Ch. 4, Ch. 5, and A.1.

Resolution

The range resolution specifies the minimum distance between two objects in the range domain at which they can still be separated. Separability by any other mean is not considered in this measure. The range resolution is limited by the minimal resolvable beat frequency of a range-FFT, resulting from the chirp duration T [PLK12], hence

$$\frac{1}{T} = \Delta f_\mathrm{b} = \frac{2}{c}\frac{B}{T}\Delta R. \tag{2.17}$$

Thus, the range resolution is dependent solely on the bandwidth as

$$\Delta R = \frac{c}{2B}. \tag{2.18}$$

The Doppler resolution defines the separability of two objects in the Doppler domain. In analogy with the range resolution, it is dependent on the overall measurement duration $N_\mathrm{c} \cdot T_\mathrm{cr}$ corresponding to the minimal resolvable beat frequency of a Doppler-FFT as

$$\Delta f_\mathrm{D} = \frac{1}{N_\mathrm{c} T_\mathrm{cr}}. \tag{2.19}$$

From the Doppler resolution, the velocity resolution is derived to be

$$\Delta v = \frac{c}{2N_\mathrm{c} T_\mathrm{cr} f_\mathrm{min}}. \tag{2.20}$$

Unambiguity

The maximum unambiguous range is limited by the Nyquist-Shannon sampling theorem [Whi15], defining the maximum unambiguous frequency of the beat signal to be

$$f_{\mathrm{b_{ua}}} = \frac{f_\mathrm{s}}{2}, \tag{2.21}$$

and hence

$$R_\mathrm{ua} = \frac{f_\mathrm{s} T c}{4B}. \tag{2.22}$$

As only positive ranges are valid, the maximum unambiguous range corresponds to twice this value.

The sampling theorem also restricts the maximum unambiguous Doppler shift in dependency of the chirp repetition rate

$$f_{\mathrm{D_{ua}}} = \frac{1}{2T_\mathrm{cr}}. \tag{2.23}$$

For the maximum unambiguous velocity results

$$v_\mathrm{ua} = \frac{c}{4T_\mathrm{cr} f_\mathrm{min}}. \tag{2.24}$$

The factor of two is caused by the phase unambiguousness in the interval $[-\pi, \pi]$ due to the need for detecting positive and negative velocities.

Maximum Detectable Range

The maximum unambiguous range does only limit the assignment of one range value to each bin index. Ranges above R_ua are detectable and folded into the second or higher Nyquist region. Given adequate preknowledge about the target and measurement surroundings, they may even be quantified correctly. However, beyond the maximum detectable range, the target signal disappears under the noise floor and cannot be detected anymore. The maximum detectable range is derived from the radar equation in (2.1) and depends on a multiplicity of parameters. In theory, it is the range at which the SNR including the signal processing gain equals 0 dB. However, an SNR_min of around 10 dB is conside-

red necessary for robust target detection.
The SNR at detection level is defined as the ratio between signal power, including achieved processing gains G_{P}, and noise power according to

$$SNR_{\mathrm{G_P}} = \frac{P_{\mathrm{rx}} \cdot G_{\mathrm{P}}}{P_{\mathrm{n}}}, \tag{2.25}$$

with the noise power $P_{\mathrm{n}} = k_{\mathrm{B}} \Gamma \iota F L$, where k_{B} denotes the Boltzmann constant, Γ the equivalent noise bandwidth, ι the system temperature, F the noise figure, and L the loss factor. For a minimum required SNR_{min}, the maximum detectable range is determined to

$$\begin{aligned} R_{\mathrm{max}} &= \left(\frac{P_{\mathrm{tx}} G_{\mathrm{tx}} G_{\mathrm{rx}} \lambda^2 \varrho_{\mathrm{t}}}{(4\pi)^3 P_{\mathrm{rx_{min}}}} \right)^{1/4} \\ &= \left(\frac{P_{\mathrm{tx}} G_{\mathrm{tx}} G_{\mathrm{rx}} \lambda^2 \varrho_{\mathrm{t}} G_{\mathrm{P}}}{(4\pi)^3 SNR_{\mathrm{min}} k_{\mathrm{B}} \Gamma \iota F L} \right)^{1/4} \end{aligned} \tag{2.26}$$

In the Doppler domain, there is no equivalent effect. Doppler shifts beyond $f_{\mathrm{D_{ua}}}$ are detectable in a higher Nyquist region without a certain limit. However, with increasing Doppler shift, coupling and migration impacts increase, deteriorating range estimation performance if no preventive processing is applied.

3 Verification and Reference Hardware

The reliability of any experimental study depends on the quality of the hardware used to generate, reference, and verify measurement data. In this chapter, an overview of the hardware used for measurements, as reference, and as supportive systems is given. Relevant information about technical specifications of each component are detailed to present the baseline capabilities of the measurement setups. Beyond specifications, behavioral anomalies and performance under realistic operating conditions are investigated. This combination enables a well-founded interpretation of measurement results in following chapters.

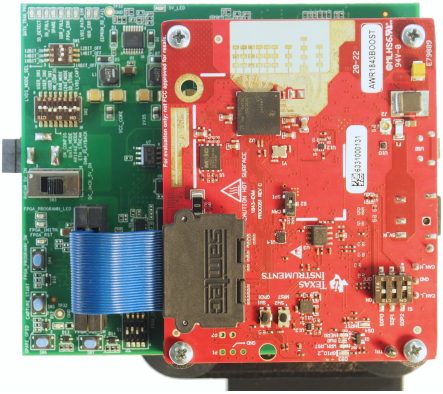

Figure 3.1: AWR1843BOOST radar (red board) with DCA1000 capture card (green board) for measurements with passive targets and mRTS tags.

Table 3.1: Measurement parameters for AWR1843BOOST used for passive targets.

Minimum frequency $f_{\min}$	77.0 GHz
Sampled bandwidth B	3.79 GHz
Number of samples N_{s}	256
Number of chirps N_{c}	255
Range resolution ΔR	0.04 m
Maximum unambiguous range R_{ua}	10.1 m
Velocity resolution Δv	0.07 m/s
Maximum unambiguous velocity v_{ua}	9.21 m/s
Frequency resolution Δf_{D}	37.1 Hz
Maximum unambiguous frequency $f_{\mathrm{D_{ua}}}$	4.73 kHz

3.1 Radar Sensors

Two different radar sensors are used depending on the requirements of each set of measurements. Both are manufactured by Texas Instruments, AWR1843BOOST and IWR6843ISK, and primary differ in the applicable frequency band.

3.1.1 AWR1843BOOST

The AWR1843BOOST from Texas Instruments shown in Fig. 3.1 is a commercial CS radar operating from 76 to 81 GHz and tailored to automotive applications in this frequency band. The farfield conditions for the integrated antennas are met after just a few centimeter and, hence, in all measured setups. When employed for measurements with passive targets, the configuration given in Table 3.1 is used within this work.
The AWR1843BOOST is additionally used for measurements with the mRTS tag originally designed for the automotive sector (Ch. 5.3). Due to the different focus of this investigation, the utilized configuration is adjusted as given in Table 3.2, mainly to provide higher unambiguous frequency and hence support more tags simultaneously.

To gain access to raw radar data, the AWR1843BOOST is used together with a DCA1000 capture card. Data capture is triggered via software, which allows for

Table 3.2: Measurement parameters for the AWR1843BOOST used for active targets.

Minimum frequency $f_{\min}$	77.0 GHz
Sampled bandwidth B	3.20 GHz
Number of samples per chirp N_{s}	256
Number of chirps N_{c}	255
Range resolution ΔR	0.05 m
Maximum unambiguous range R_{ua}	12.0 m
Velocity resolution Δv	0.23 m/s
Maximum unambiguous velocity v_{ua}	29.5 m/s
Frequency resolution Δf_{D}	119 Hz
Maximum unambiguous frequency $f_{\mathrm{D_{ua}}}$	15.2 kHz

an automated measurement routine. Alternatively, a hardware trigger is available to synchronize multiple devices within the measurement setup. The transfer of data to the PC is unsupervised and therefore prone to data loss. While such losses can be reduced, they cannot be entirely avoided, so the link is continuously monitored and affected measurements are discarded. Occasionally, individual frames of a measurement are corrupted, resulting in a significantly higher noise as exemplified in Fig. 3.2 for the raw data and range profiles of an unaffected ((a), (b)) and a corrupted measurement ((c), (d)) taken under identical conditions. The cause of this corruption currently remains unknown and cannot be further investigated as no hardware internals are accessible. Although it occurs rarely, monitoring ensures that compromised measurements are identified and excluded, preserving the integrity of the overall results.

Additionally, a temperature dependency of the range estimation is observed as depicted in Fig. 3.3. The temperature of the radar chip is monitored with an infrared camera. 300 measurements are recorded within around 10 s without interruption and without any change in the measurement setup and surroundings. The radar heats up during these measurements, which results in a drift in the measured frequency following the temperature and the range estimated from it. The effect arises as soon as more than one measurement is recorded without sufficient time for the radar to cool down. Over time, temperature and range estimation change less and approach a constant value. If the ambient tempera-

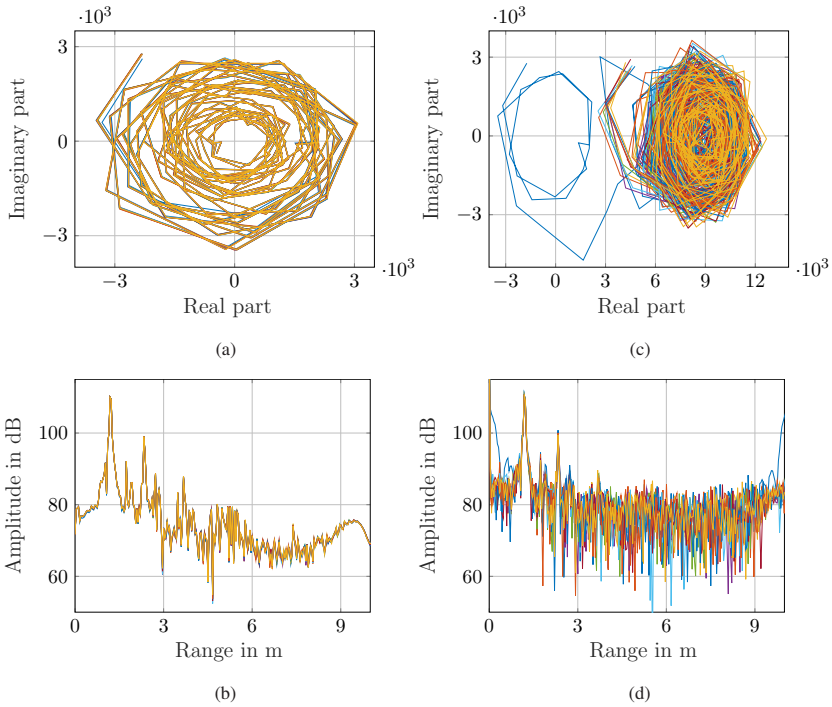

Figure 3.2: Raw data ((a) and (c)) and range profiles ((b) and (d)) of two measurements in the configuration of Table 3.1. 10 out of the 255 recorded chirps are depicted. The intended target causes the strongest peak in both measurements, however, IQ imbalances arise for the corrupted measurement ((c) and (d)) and the noise floor is significantly increased.

ture remains constant, the temperature-dependent range drift is very systematic and can be calibrated to avoid implications on the results.

3.1.2 IWR6843ISK

The IWR6843ISK (Fig. 3.4) is another commercial CS radar from Texas Instruments, operating in the frequency band from 60 to 64 GHz. With the exception of the frequency band, both radars are highly comparable, and the aforementioned considerations for the AWR1843BOOST are equally applicable to the

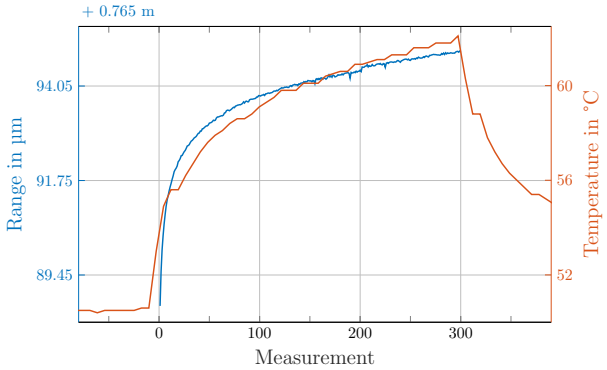

Figure 3.3: Drift of range estimation and temperature over 300 consecutive measurements, showing clear correlation. Range estimates are depicted with an offset of 0.765 m.

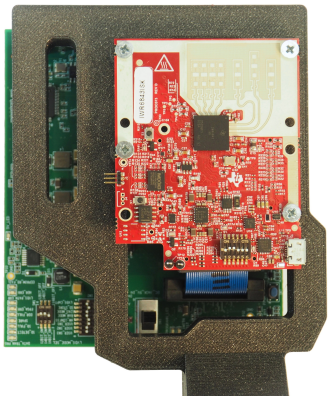

Figure 3.4: IWR6843ISK radar (red board) with DCA1000 capture card (green board) for measurements with the assembled Doppler tag.

Table 3.3: Measurement parameters for IWR6843ISK.

Minimum frequency f_{min}	60.0 GHz
Sampled bandwidth B	1.50 GHz
Number of samples per chirp N_{s}	256
Number of chirps N_{c}	255
Range resolution ΔR	0.10 m
Maximum unambiguous range R_{ua}	25.5 m
Velocity resolution Δv	0.21 m/s
Maximum unambiguous velocity v_{ua}	26.2 m/s
Frequency resolution Δf_{D}	82.4 Hz
Maximum unambiguous frequency $f_{\mathrm{D_{ua}}}$	10.5 kHz

IWR6843ISK. It is used together with the assembled Doppler tag in the ISM frequency band, better suited for industrial applications, with the configuration given in Table 3.3.

3.2 Reference Systems

To reference conducted measurements, three linear motors, coming with different range, velocity, and accuracy restrictions, and a rotation stage for angular reference are utilized. For most measurements, the radars are used without run-time calibration, therefore not providing an expressive absolute range estimate. Range references are hence established relatively: Two range estimates at known distance, defined by a linear motor, are compared against each other. Consequently, the accuracy of the linear motor serves as reference accuracy. In contrast, frequency and velocity references are absolute using nominal values as no additional calibration is required.

3.2.1 M-683 Piezo Motorized Precision Translation Stage

The M-683 piezo motorized precision translation stage depicted in Fig. 3.5 is a small linear motor from Physik Instrumente. It provides a travel range of 50 mm

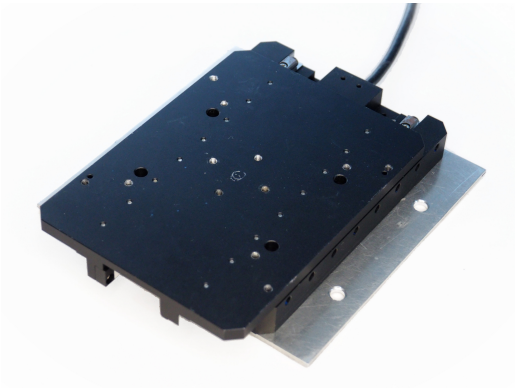

Figure 3.5: M-683 piezo motorized precision translation stage as a reference for highly accurate range estimation.

with a sensor resolution of 0.1 µm, unidirectional repeatability of 0.2 µm, as well as bidirectional repeatability of ± 1 µm. Therewith, it is well suited to reference highly accurate range measurements in static scenarios, demonstrating rather the performance capabilities of a setup than realistic applications.

As only resolution and repeatability values are specified for this stage, a custom-build Michelson interferometer is used for accuracy evaluation. Its achievable resolution is in the order of half the wavelength of the light used (here $\lambda = 532\,\mathrm{nm}$), so that it is an adequate reference system for the translation stage in radar measurements. The setup on a small optical table is depicted in Fig. 3.6a with one of the interferometer mirrors mounted on the translation stage. The stage was moved with a step size of 1 mm, as planned for in the radar measurement setup, and three exemplary motor positions in the center of the stage as well as at the boundaries of the travel range were evaluated. Fig. 3.6b shows the recording of one of the conducted measurements. From 0 to around 1.1 s, the stage is in motion, causing an oscillation pattern in the photodiode voltage. At the end of the motion, there is significant residual vibration visible in the voltage but systematically different and thereby differentiated from the oscillations. The zero crossings of the oscillation are evaluated to determine the range passed. The achieved range errors confirm proper stage operation over the whole travel range. Most conducted measurements include errors below 1 µm up to a few µm, however, there were outliers. These are most likely caused not

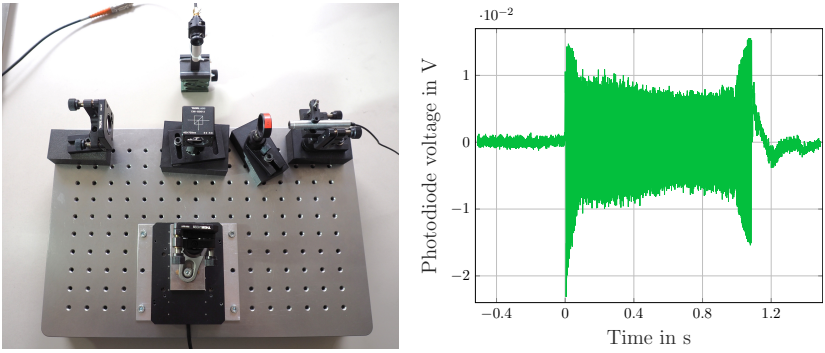

(a) (b)

Figure 3.6: Michelson interferometer with one of the interferometer mirrors mounted on the translation stage for traveling distance measurements (a) and measurement results of the photodiode voltage during movement from one static position to another (b).

by the stage itself, but movement in the interferometer, which is very sensitive to even smallest vibrations. Additionally, the interferometer resolution limits the achievable accuracy in these measurements. For the purpose of this work, the accuracy of the M-683 translation stage is thus assumed to be sufficiently close to its sensor resolution and repeatability, with only unidirectional movement used during radar measurements.

3.2.2 M-414.3DG Precision Linear Stage

The M-414.3DG precision linear stage from Physik Instrumente is shown in Fig. 3.7. With the travel range of 300 mm, larger setups can be realized. This stage is used as part of the referencing for self-positioning presented in Ch. 7.3. The provided unidirectional repeatability of 0.5 µm is sufficient as the overall accuracy in this application is not as high as for one-dimensional measurements. Nevertheless, this stage is also evaluated using the Michelson interferometer discussed in Ch. 3.2.1. Due to the larger size of the stage, the whole setup is moved to a larger optical table, reducing motion in the setup. However, the movement of the stage itself causes significant vibrations, particularly during starting and slow down. These influence the interferometer measurements and make it more difficult to appoint an accuracy based on the measurements. As

Figure 3.7: M-414.3DG precision linear stage as a reference for self-positioning.

the errors are still mostly below 10 µm and variations are primary accounted to the setup, the accuracy is again assumed to be close to the unidirectional repeatability. Despite the weaker evidence for the accuracy of this stage, it is a suitable reference for multidimensional measurements, whose errors are in millimeters.

3.2.3 LTSE165.3280.2K.MS2 Linear Rail

To allow for dynamic radar measurements, a stage with significant length and velocity is required. This is provided by the LTSE165.3280.2K.MS2 linear rail from SKF (Fig. 3.8) with a length of 3.3 m and a maximum velocity of 5 m/s. However, this velocity is only reached in a small length segment in the center of the rail, which has to be taken into consideration during setup design. The accuracy of the rail is specified to ± 10 µm/m. In velocity, the rail oscillates around the setpoint value, a behavior observed and investigated in more detail in Ch. 4.3.2.
This rail is used together with the M-683 stage for dynamic measurements of passive and active targets.

Figure 3.8: LTSE165.3280.2K.MS2 linear rail as a reference for dynamic radar measurements.

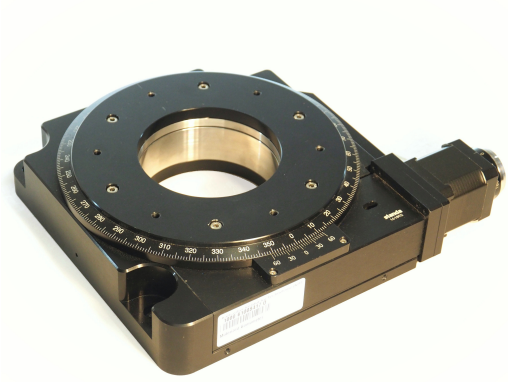

Figure 3.9: 8MR190-90 motorized rotation stage as a reference for orientation estimation.

3.2.4 8MR190-90 Motorized Rotation Stage

To reference rotations in Ch. 7.2, an 8MR190-90 motorized rotation stage from Standa, shown in Fig. 3.9, is used. It references the orientation estimation discussed in Ch. 7.2 with a resolution of up to $6.75'' \approx 1.0 \cdot 10^{-3\circ}$ and a bidirectional repeatability of $72'' \approx 0.02°$. Accuracy is expected to be in similar range and hence well below expected angular accuracy using dual-point ranging as developed in Ch. 7.2.

3.3 Atmospheric Parameter Monitoring

3.3.1 LOG32THP

According to (2.7), range as well as velocity estimation require knowledge about the speed of light in the medium the wave is propagating in. For highly accurate measurements, vacuum does not constitute a sufficient approximation, hence atmospheric parameters are monitored with a LOG32THP Thermo-Hygro-Pressure Data Logger from Dostmann electronic. Temperature, relative huminity, and air pressure are tracked and averaged during each measurement. The uncertainties of the measuements are ±0.5 K, ±3.0 %rH, and ±1.0 hPa, respectively. Based on these parameters, the refractive index ν is calculated according to [PKJP22] and the propagation velocity of the electromagnetic wave is determined to be

$$c = \frac{c_0}{\nu}. \tag{3.1}$$

This propagation velocity in air is utilized throughout the whole signal processing chain instead of c_0.

The hardware discussed constitutes the main parts of the measurement setups used within this work. Detailed information on the different setups and their focus is given in the corresponding chapters together with the respective measurement results.

4 Highly Accurate Range Estimation with Moderate Bandwidths

High-accuracy range estimation is an emerging field and indispensable to many areas. In the context of industry 4.0, it can form the data basis for further automation as well as safe human-machine interaction and cooperation. Range estimation with µm accuracy is of interest in both static and dynamic scenarios and enables derived applications such as position or orientation estimation.

In this chapter, the signal processing chain for highly accurate, phase-offset-based range estimation for CS is initially derived, considering static and dynamic targets. It utilizes the fact that two independent range estimates can be gained from the radar signal. The first coarse one determines the range bin of interest, while the second one is used to pinpoint the range within this bin. Simulative investigation demonstrates the suitability and theoretical capability of the system and allows for a thorough analysis of effects and influence factors. Metrological verification proves the practical applicability with achieved accuracies, which do not reach the theoretic prospects, but contextualize the proposed processing as a precious way of improving the range estimation accuracy in signal processing without demanding hardware requirements. The CRLB is derived for static and dynamic scenarios and applied to the results as a performance measure.

4.1 $f\varphi$ Range Estimation for CS Radar

A highly accurate, phase-offset-based range estimation was first introduced for FMCW in [APK+11], based on an idea of [WMM93]. However, limitations in estimation and scenario coverage, particularly regarding multiple objects in motion, favor CS radars. Due to the similarity of CS and FMCW, the approach can be modified to be applicable in CS. Thus, this work builds on the existing knowledge and proposes a new signal processing chain that enables highly

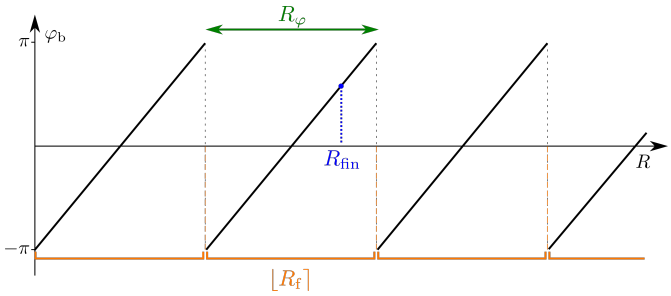

Figure 4.1: Visualization of highly accurate $f\varphi$ range estimation. The coarse range estimation, containing the complete phase rotations, is determined from R_f, and R_φ is added to gain the highly accurate range estimation R_fin.

accurate range estimation for static and dynamic targets using a CS radar.
The approach was first published in [10] for static targets and extended to cover dynamic scenarios in [9] and [13].

According to (2.7), the signal delay and hence, range information, is comprised in multiple subterms of the signal. In frequency-based estimation, the range is determined from the delay-dependent fast-time frequency, resulting in a coarse range estimate R_f. R_ua is in the range of several to tens of meters according to (2.22). The phase offset φ_b contains a more accurate range information, but is only unambiguous within 2π, at 77 GHz corresponding to 2 mm. By combining both terms, a highly accurate final range estimate R_fin, whose unambiguity is determined by the frequency evaluation, is obtained. The number of complete phase rotations and the corresponding range are determined using the frequency-based range estimate and the remaining phase rotation in the phase offset yields a range estimate R_φ to be added as visualized in Fig. 4.1. The combined analysis is henceforth referred to as $f\varphi$ range estimation, referencing to the parameter estimation of f and φ, respectively.
Only the linear share of the phase offset is used, gained by eliminating the quadratic term $2\pi \frac{B}{2T} \cdot \widehat{\tau}_0^2$, where R_f provides a first estimate for τ_0 according to (2.5). The linearization provides higher sensitivity and allows for suppression of systematic disturbances by averaging over multiple measurements. From the remaining linear offset

$$\varphi_\mathrm{b,lin} = 2\pi f_\mathrm{min} \cdot \tau_0, \tag{4.1}$$

R_φ is determined to

$$R_\varphi = \frac{c}{4f_{\min}} \frac{\varphi_{\mathrm{b,lin}}}{\pi} \tag{4.2}$$

and unambiguous in the interval

$$R_\pi - R_{-\pi} = \frac{c}{2f_{\min}}. \tag{4.3}$$

To combine both range estimates, the observable range is divided into bins of size $\frac{c}{2f_{\min}}$ and R_f is used to choose the bin the target is located in. Within this bin, the phase offset is unambiguous and used to determine the exact target range. The final range estimate results to be

$$R_{\mathrm{fin}} = \left\lfloor \frac{2f_{\min}}{c} \cdot R_\mathrm{f} \right\rceil \cdot \frac{c}{2f_{\min}} + R_\varphi, \tag{4.4}$$

where $\lfloor \cdot \rceil$ denotes the rounding function, rounding the enclosed value to the next integer.

To identify the correct range bin, the frequency-based estimate requires sufficient accuracy. A range error equal to the bin size is not sufficient and can result in an offset of one bin. If, however, the error after frequency-based estimation is restricted to half the bin size, an erroneous bin choice can be detected and corrected as discussed in [Sch17]. Hence, a maximal range error of $\frac{c}{4f_{\min}}$ is required. To reach this, not only an FFT is applied to the signal as discussed in Ch. 2.2.1, but an additional chirp Z-transform (CZT). The CZT computes the Z-transform along spiral contours in the z-plane as depicted in Fig. 4.2. With evenly spaced samples around the unit circle, the CZT corresponds to a zero-padded FFT in a specified region of the frequency spectrum. This region is chosen symmetrically around the estimate of an FFT without zero padding. With its size equal to the resolution of the range spectrum, the CZT operates in one bin. This approach is significantly more efficient than comparably zero padding the FFT over the complete signal. The CZT is applied multiple times, iteratively choosing the new starting point and region size from the results of the previous CZT. In theory, the spectral resolution can be arbitrarily improved with this approach, however, systematic errors limit the effect on range estimation. In measurement processing, two to three iterations were found to be beneficial while no enhancement was observed for more iterations. It is important to distinguish between the spectral resolution, corresponding to a

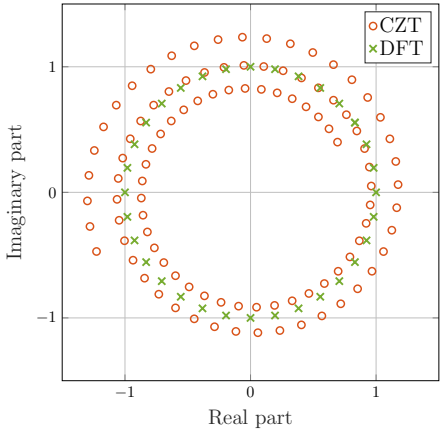

Figure 4.2: Comparison of DFT and CZT contours in the z-plane.

digital zoom, and the actual radar resolution as discussed in Ch. 2.2.2. The latter cannot be improved in processing and hence, targets that are closer to each other than this resolution cannot be resolved using a CZT or comparable processing methods. Only the value of a single detection is refined, improving its accuracy [GDBCV21].

The application of the proposed processing necessitates the separate determination of the phase offset. Therefore, (2.7) is fractionized:

$$\begin{aligned}
\Phi_{\mathrm{b}}(t,m) &= \Phi_{\mathrm{tx}}(t,m) - \Phi_{\mathrm{rx}}(t,m) \\
&= 2\pi\Bigg(\Bigg(\underbrace{\frac{B}{T}\tau_0}_{\mathrm{V}} - \underbrace{\frac{2v}{c}\frac{B}{T}\tau_0}_{\mathrm{I}} + \underbrace{f_{\min}\frac{2v}{c}}_{\mathrm{IV}}\Bigg)t \\
&\quad + \Bigg(\underbrace{\frac{2v}{c}f_{\min}}_{\mathrm{IV}} - \underbrace{\frac{2v}{c}\frac{B}{T}\tau_0}_{\mathrm{I}}\Bigg)mT \\
&\quad + \Bigg(\underbrace{\frac{B}{T}\frac{2v}{c}}_{\mathrm{IV}} - \underbrace{\frac{B}{T}\frac{4v^2}{c^2}}_{\mathrm{III}}\Bigg)tmT \\
&\quad + \Bigg(\underbrace{\frac{B}{T}\frac{2v}{c}}_{\mathrm{IV}} - \underbrace{\frac{B}{T}\frac{2v^2}{c^2}}_{\mathrm{III}}\Bigg)t^2 \\
&\quad + \underbrace{\Bigg(-\frac{B}{T}\frac{2v^2}{c^2}\Bigg)(mT)^2}_{\mathrm{II}} \\
&\quad + \overbrace{\tau_0\Bigg(f_{\min} - \underbrace{\frac{B}{2T}\tau_0}_{\mathrm{VI}}\Bigg)}^{\varphi_{\mathrm{b}}}\Bigg)
\end{aligned} \tag{4.5}$$

Roman numbers mark subterms that are processed jointly as discussed hereinafter, equal numbers do not indicate same phenomenal origin or value. Assuming a static target, all velocity-dependent terms in (4.5) vanish and an elimination of the estimated term $2\pi\frac{B}{T}\widehat{\tau}_0 \cdot t$ yields the phase offset φ_{b}. For targets in motion, Doppler correction is required: The occurring Doppler shift is estimated using an FFT along the chirps as discussed in 2.2.1. Together with the range estimate after the FFT, it is used to perform a coarse phase correction of the two coupling terms (4.5)-I as well as the largest of the three quadratic terms, (4.5)-II. The other two quadratic terms, (4.5)-III, are negligible due to $v^2 \ll c^2$,

so a correction is not necessary. However, $(mT)^2 \gg tmT \gg t^2$ so that (4.5)-II impairs estimation if uncorrected. The Doppler shift is estimated again with a CZT to improve the estimation accuracy. The Doppler-CZT is applied on each sample across the chirps so that one estimate per sample is gained, which is averaged to further improve the estimation. The final velocity estimate is used for the correction of all remaining Doppler-dependent terms (4.5)-IV and delivers additional information about the target, e.g., for tracking. This original correction allows for highly accurate range estimation despite target motion and is extended to artificial Doppler shifts in Ch. 5.1.

Assuming an ideal estimation, the remaining phase after all Doppler-related corrections is

$$\Phi_\mathrm{b}(t,m) = 2\pi\left(\underbrace{\frac{B}{T}\tau_0 \cdot t}_{\mathrm{V}} + \overbrace{\tau_0 f_\mathrm{min} - \underbrace{\frac{B}{2T}\tau_0^2}_{\mathrm{VI}}}^{\varphi_\mathrm{b}}\right), \tag{4.6}$$

which is exactly the phase of a static target. The frequency-based range estimation and subsequent range-CZT is applied anew to the corrected signal (4.6) to minimize the influence of coupling and migration terms. Correcting the term (4.6)-V yields the phase offset and allows for phase-offset-based range estimation. Both estimates are subsequently combined according to (4.4). Figure 4.3 depicts the complete processing chain schematically, including formulaic explanations.

Although Doppler-FFT and -CZT are used to estimate the Doppler, the corresponding processing gain is not included in the subsequent $f\varphi$ range estimation. To preserve the complete processing gain and enhance estimation results, the chirps are summed up prior to frequency-based range estimation. This is valid under the assumption of a perfect Doppler correction because without motion impact, each chirp contains the same information about the initial range. However, the estimation of occurred Doppler shifts and their correction is never ideal, hence errors propagate from Doppler to range estimation. For the correction of the small terms (4.5)-I and (4.5)-II, this effect is negligible. For the terms (4.5)-IV, a faulty velocity estimation $v + \delta v$ results in an error term

$$\delta\Phi_\mathrm{b} = \frac{2\delta v}{c}\left(f_\mathrm{min}\left(t + mT\right) + \frac{B}{T}\left(tmT + t^2\right)\right), \tag{4.7}$$

coarse phase correction

$$\Phi_\mathrm{b}(t,m) = 2\pi\Bigg(\Bigg(\frac{B}{T}\tau_0 - \underbrace{\frac{2v}{c_0}\frac{B}{T}\tau_0}_{\text{I}} + f_\mathrm{min}\frac{2v}{c_0}\Bigg)t + \Bigg(\frac{B}{T}\frac{2v}{c_0}\Bigg)t^2 + \Bigg(\frac{2v}{c_0}f_\mathrm{min} - \underbrace{\frac{2v}{c_0}\frac{B}{T}\tau_0}_{\text{I}}\Bigg)mT + \Bigg(\frac{B}{T}\frac{2v}{c_0}\Bigg)tmT + \Bigg(\underbrace{-\frac{B}{T}\frac{2v^2}{c_0^2}}_{\text{II}}\Bigg)(mT)^2 + \tau_0\Bigg(f_\mathrm{min} - \frac{B}{2T}\tau_0\Bigg)\Bigg)$$

velocity correction

$$\Phi_\mathrm{b}(t,m) = 2\pi\Bigg(\Bigg(\frac{B}{T}\tau_0 + \underbrace{f_\mathrm{min}\frac{2v}{c_0}}_{\text{IV}}\Bigg)t + \underbrace{\Bigg(\frac{B}{T}\frac{2v}{c_0}\Bigg)}_{\text{IV}}t^2 + \underbrace{\Bigg(\frac{2v}{c_0}f_\mathrm{min}\Bigg)}_{\text{IV}}mT + \underbrace{\Bigg(\frac{B}{T}\frac{2v}{c_0}\Bigg)}_{\text{IV}}tmT + \tau_0\Bigg(f_\mathrm{min} - \frac{B}{2T}\tau_0\Bigg)\Bigg)$$

phase of static target

$$\Phi_\mathrm{b}(t,m) = 2\pi\Bigg(\frac{B}{T}\tau_0 \cdot t + \tau_0 f_\mathrm{min} - \frac{B}{2T}\tau_0^2\Bigg)$$

fine phase correction

$$\Phi_\mathrm{b}(t) = 2\pi\Bigg(\underbrace{\frac{B}{T}\tau_0 \cdot t}_{\text{V}} + \tau_0 f_\mathrm{min} - \underbrace{\frac{B}{2T}\tau_0^2}_{\text{VI}}\Bigg)$$

isolated phase offset

$$\varphi_\mathrm{b,lin} = 2\pi\tau_0 f_\mathrm{min} \;\Leftrightarrow\; R_\varphi = \frac{c_0}{4f_\mathrm{min}}\frac{\varphi_\mathrm{b,lin}}{\pi}$$

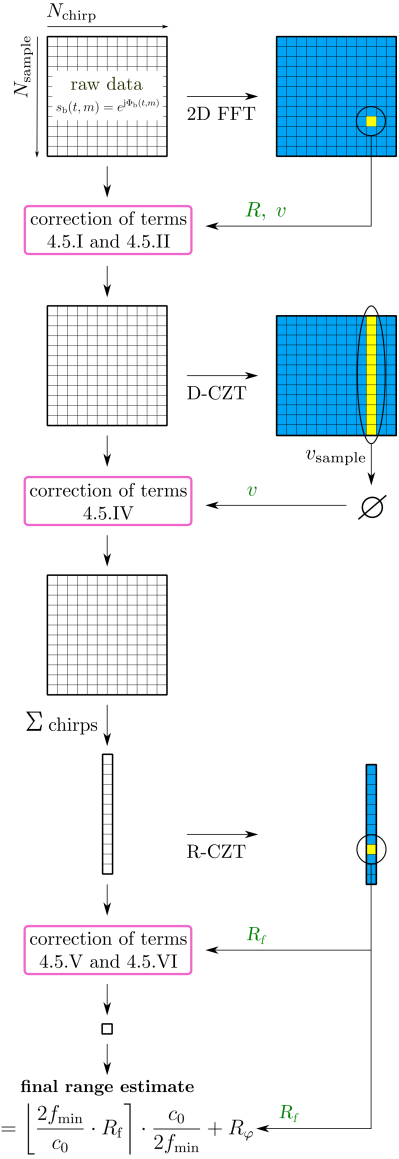

Figure 4.3: Complete processing chain for highly accurate $f\varphi$ range estimation.

which adds to the remaining phase after correction of (4.6).
From (4.6) and (4.7), it is obvious that the phase offset φ_b, and hence R_φ, is not directly affected by a velocity error but is the frequency-based estimate R_f, which could lead to an erroneous bin assignment. Furthermore, the summation of all chirps suffers phase shifts, which influence both frequency- and phase-based range estimation. Nevertheless, a direct comparison shows that the sum of all chirps outperforms the usage of only the first chirp due to the increased SNR, disregarding the erroneous impact of leftover Doppler terms. Additionally, the rounding function suppresses error propagation in frequency analysis and mostly allows for correct bin estimation. As the defective R_f is also used to correct the (4.6)-V term prior to phase determination, the final estimate is still deteriorated, emphasizing the importance of accurate Doppler correction. The correction additionally suppresses targets with velocities other than the evaluated one, which mainly augments the signal-to-interference-and-noise ratio (SINR) and enhances the achievable estimation accuracy. Particularly, static clutter is efficiently suppressed for moving objects of interest. If the object is purely static, the Doppler correction can be omitted, however, dispensable correction does not deteriorate the estimation.

This approach is an extension of existing phase-based processing for FMCW and could, without modifications, also be applied to FMCW, provided a reliable Doppler estimation. However, not all considerations are required as in FMCW, similar bandwidths are covered in significantly larger sampling time compared to CS, hence $\frac{B}{T_\mathrm{FMCW}} \ll \frac{B}{T_\mathrm{CS}}$. In combination with $m = 1$, the signal model can be simplified and corrections steps can be omitted, which is why they were first introduced for CS.

4.1.1 CRLB for Static Estimation

As discussed in Ch. 2.2.2, the CRLB is a measure of the achievable accuracy of an unbiased estimator, formulated as a lower bound of its variance. To apply statistical measures to the range estimation results of radar measurements, radar range estimation is interpreted as a statistical estimator using repeated measurements of the same relative range as samples of a population. For the measurements, targets with a high RCS such as a corner reflector or an active tag are used at medium distances of up to a few meters, so that a good SNR is ensured. The CRLB is hence better suited in this scenario than other bounds

such as the Ziv-Zakai lower bound, representing a scenario with low SNR.
In [Kay93], the CRLB is given for frequency and phase estimation of a complex signal. The derivation assumes a single sine wave superimposed by additive white Gaussian noise (AWGN), neglecting additional factors such as interference, multiple reflections, or nonlinear distortions. Using a transformation of parameters (A.9), the CRLB for range estimation from frequency and phase-offset analysis is derived to be

$$\mathrm{var}_{\mathrm{CS}}(R_{\mathrm{f}}) \geq \frac{3c^2 N_{\mathrm{s}}}{8\pi^2 B^2 \eta (N_{\mathrm{s}}^2 - 1)} \approx \frac{3c^2}{8\pi^2 B^2 \eta N_{\mathrm{s}}} \tag{4.8}$$

and

$$\mathrm{var}_{\mathrm{CS}}(R_{\varphi}) \gtrapprox \frac{c^2 T}{8\pi^2 B \eta N_{\mathrm{s}}} \frac{1}{\frac{T}{B} f_{\mathrm{min}}^2 - f_{\mathrm{min}} \frac{4R}{c} + \frac{B}{T} (\frac{2R}{c})^2}, \tag{4.9}$$

where η denotes the input SNR without processing gain from range estimation and N_{s} the number of samples per chirp, $N_{\mathrm{s}} \gg 1$. Instead of N_{s}, the number of samples per measurement $N_{\mathrm{s}} \cdot N_{\mathrm{c}}$ is applicable if a continuous processing over all samples is applied. However, for the given processing chain (Fig. 4.3), a potential Doppler shift is eliminated and the chirps are subsequently summed up prior to range estimation. Hence, only N_{s} samples are available for range estimation, although the coherent summation augments the SNR by a factor of N_{c}, so that this processing results in the same CRLB as range estimation over all samples without summation. A detailed derivation of the CRLBs for different scenarios can be found in the addendum.

Other than for FMCW, for CS the bandwidth is still included in (4.9), but has minor effects as the influence of the quadratic phase-offset term leading to this dependency is small. Hence, the assumption $\mathrm{var}_{\mathrm{CS}}(R_{\varphi}) \approx \mathrm{var}_{\mathrm{FMCW}}(R_{\varphi})$ can be justified, with

$$\mathrm{var}_{\mathrm{FMCW}}(R_{\varphi_{\mathrm{b}}}) \gtrapprox \frac{c^2}{8\pi^2 f_{\mathrm{min}}^2 \eta N_{\mathrm{s}}} \tag{4.10}$$

similar to [SAPZ12]. The described CRLB for frequency and phase-offset analysis assumes a separate estimation, which is only true for frequency analysis. Standalone phase analysis does not provide a valid range estimate, which is why the CRLB for R_{fin} needed to be derived from a combined estimation approach. However, the major limitation in accuracy originates from phase-based analysis as R_{f} is primary used to determine the correct range bin, and the

reached accuracy of R_f is not exploited. Assuming a correct bin assignment, $\mathrm{var}(R_{\varphi_\mathrm{b}}) \approx \mathrm{var}(R_\mathrm{fin})$ is hence valid.

Applicability Considerations

This derivation contains several assumptions which cannot be realized in measurements. The first and foremost is the assumption of an unbiased estimator. Even with the proposed combined signal processing and relative measurement procedure, the range estimation is not truly unbiased. This also applies to most radar applications unless special precautions have been taken, such as in [Sch17]. Already quantization introduces systematic errors if the measurement steps are not multiples of the range resolution or the bin size is negligibly small. The CRLB can be extended to biased estimators [Eld04], assuming a bias

$$\boldsymbol{b}(\boldsymbol{\theta}) = E(\widehat{\boldsymbol{\theta}}) - \boldsymbol{\theta}, \tag{4.11}$$

with the expected value E and the parameter vector $\boldsymbol{\theta}$. The corresponding covariance is bounded by

$$\mathrm{var}(\widehat{\boldsymbol{\theta}})_\mathrm{biased} \geq \left(\mathbf{I} + \frac{\partial \boldsymbol{b}(\boldsymbol{\theta})}{\partial \boldsymbol{\theta}}\right) [\mathbf{I}_\mathrm{F}]^{-1} \left(\mathbf{I} + \frac{\partial \boldsymbol{b}(\boldsymbol{\theta})}{\partial \boldsymbol{\theta}}\right)^* , \tag{4.12}$$

where $(\cdot)^*$ denotes the Hermitian conjugate. The unbiased CRLB is a special case of (4.12) with $\boldsymbol{b}(\boldsymbol{\theta}) = 0$. The bound can be lower for certain bias as for an unbiased estimator and a biased estimator can generally have mean square error (MSE) values below the unbiased CRLB [SM90]. As a border case, an estimator that always returns the same (incorrect) value is considered. For this estimator, (4.12) vanishes, giving zero variance disregarding any bias the estimator might have. Similarly, assuming a bias not dependent on $\boldsymbol{\theta}$, the influence of the bias vanishes and the unbiased CRLB is applicable:

$$\mathrm{var}(\widehat{\boldsymbol{\theta}})_\mathrm{biased} = \mathrm{var}(\widehat{\boldsymbol{\theta}}) \tag{4.13}$$

Assuming a relative measurement procedure or adequate radar calibration and sufficient SNR, the error in range measurements can be considered independent of the measured range, hence the unbiased CRLB according to (4.13) is maintained hereinafter.

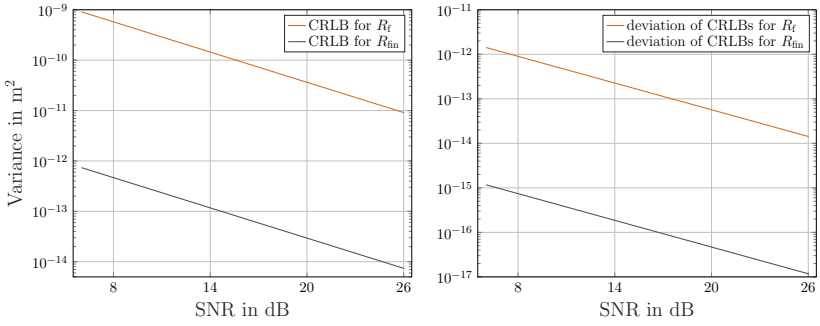

Figure 4.4: CRLB for R_f and R_fin (a) and deviation of both CRLBs from numerically calculated bounds including the first multiple reflection of the target (b).

Another assumption not justified in measurements is the one target hypothesis. Even if the reflection of the target of interest is much stronger than all other reflections, at least multiple reflections of the same target remain significant and scale with the strength of the first reflection, so that they cannot be avoided completely. Including the first multiple reflection as a second target, the Fisher information matrix is given in A.1.2. The structure of the matrix remains unchanged in comparison to the single target derivation and contains two submatrices describing the influence of the first and the second target, respectively. Only the cross-terms contain parameters from both targets, in the form of the frequency difference $f_{\mathrm{b},2} - f_{\mathrm{b},1}$ and the phase difference $\varphi_{\mathrm{b},2} - \varphi_{\mathrm{b},1}$. Considering two distinct targets, they are typically much smaller than the other terms and hence negligible. As a result, the CRLB for the estimated parameters is hardly affected. Even if $f_{\mathrm{b},2} = 2 \cdot f_{\mathrm{b},1}$ is assumed, representing a target and its first multiple reflection, and the terms $f_{\mathrm{b},2} - f_{\mathrm{b},1}$ and $\varphi_{\mathrm{b},2} - \varphi_{\mathrm{b},1}$ become significant, the cross-terms are still small and hardly impact the CRLB. This is shown in Fig. 4.4, depicting the single target CRLBs for R_f and R_fin as well as the deviation of those from numerically calculated bounds including the first multiple reflection of the target. The deviation is small and negligible.
However, if multiple target influences of different origin are included in the

signal, effects can become significant. Considering that, an approximate CRLB behavior can be described by using the estimated SINR instead of the SNR with

$$SINR = \frac{A^2}{2\left(\sigma_{\mathrm{I}}^2 + \sigma^2\right)}, \tag{4.14}$$

where A denotes the signal amplitude, σ_{I}^2 the interference variance, and σ^2 the noise variance. The original derivation assumes the SNR, which corresponds to a single target scenario with no unmodelled signal components. If multiple reflections, clutter, and other unwanted target reflections act as additional interference sources that degrade the estimation performance, the SINR is favored as the SNR does not reflect the true quality of the observation. The SINR provides a more realistic measure of the effective information content available for parameter estimation. Substituting SNR by SINR in the CRLB expression yields a lower bound that better represents the estimation variance achievable in interference-limited radar environments, although it is an approximation, not a stringent mathematical derivation. For most setups within this work, the first multiple reflection of a target is dominant, however, strongly reflecting components in the measurement setup can have significant impact, particularly in the setup used for dynamic measurements.

The CRLB is defined as a lower bound of the estimated parameter, here the estimated range. Nonetheless, the variance of the range error is also of interest, particularly if the trueness of a system is in question. For unbiased estimation, the variance of range and range error are strictly related to each other. However, this is not the case in most radar applications as discussed above. As both stochastic and systematic implications are present in realistic measurement scenarios and cannot be differentiated and quantified exactly, the variance of the range error cannot be confined with a bound such as the CRLB. However, under certain conditions, limitations can be given.
For the measurements hereinafter, the relation

$$\delta R = \widehat{R}_{k+1} - \widehat{R}_k - \Lambda \tag{4.15}$$

is used and hence,

$$\mathrm{var}(\delta R) = \mathrm{var}(\widehat{R}_{k+1} - \widehat{R}_k - \Lambda). \tag{4.16}$$

Λ is the step of the reference system and thus assumed to be perfectly stable in the order of magnitude considered ($\mathrm{var}(\Lambda) = 0$) and uncorrelated to the range estimation, thereby

$$\mathrm{var}(\delta R) = \mathrm{var}(\widehat{R}_{k+1} - \widehat{R}_k) + \mathrm{var}(\Lambda) = \mathrm{var}(\widehat{R}_{k+1} - \widehat{R}_k), \tag{4.17}$$

where

$$\mathrm{var}(\widehat{R}_{k+1} - \widehat{R}_k) = \mathrm{var}(\widehat{R}) + \mathrm{var}(\widehat{R}) - 2 \cdot \mathrm{Cov}(\widehat{R}_{k+1}, \widehat{R}_k). \tag{4.18}$$

Two cases can be differentiated for (4.18): If white noise is predominant, $\widehat{R}_{k+1}$ and $\widehat{R}_k$ can be assumed to be uncorrelated, hence $\mathrm{Cov}(\widehat{R}_{k+1}, \widehat{R}_k) = 0$. This case simplifies the variance of the range error to

$$\mathrm{var}(\delta R) \approx 2 \cdot \mathrm{var}(\widehat{R}). \tag{4.19}$$

If, in contrast, systematic effects are predominant, $\widehat{R}_{k+1}$ and $\widehat{R}_k$ are correlated, $\mathrm{Cov}(\widehat{R}_{k+1}, \widehat{R}_k) \neq 0$. However, positive correlation can be assumed as systematic errors influence range estimates similarly, hence

$$\mathrm{var}(\delta R) \leq 2 \cdot \mathrm{var}(\widehat{R}). \tag{4.20}$$

As a special case, if $\widehat{R}_{k+1}$ and $\widehat{R}_k$ are perfectly correlated, $\mathrm{Cov}(\widehat{R}_{k+1}, \widehat{R}_k) = \mathrm{var}(\widehat{R})$ and

$$\mathrm{var}(\delta R) = 0. \tag{4.21}$$

As discussed prior, measurements contain a systematic error, hence dominant white noise cannot be assumed. Further, the correlation between two range estimations $\widehat{R}_{k+1}$ and $\widehat{R}_k$ cannot be quantified so that no bound is found for the variance of the range error, but the relation

$$\mathrm{var}(\delta R) \leq 2 \cdot \mathrm{var}(\widehat{R}) \tag{4.22}$$

is valid. Henceforth, both variances $\mathrm{var}(\delta R)$ and $\mathrm{var}(\widehat{R})$ are used to investigate the range estimation behavior and dependencies, although the CRLB only refers to $\mathrm{var}(\widehat{R})$.

4.1.2 CRLB for Dynamic Estimation

The bounds described previously only consider range estimation without taking into account Doppler shifts and the corresponding processing. For the chain proposed in Fig. 4.3, this is a valid assumption as Doppler shifts are eliminated and the range processing is performed separately. Remaining Doppler shifts can deteriorate the estimation as the summation does not yield the complete processing gain, however, this decrease is included in the SINR. Additionally, phase-offset estimation is affected by non-ideal Doppler elimination as residual terms are treated as part of the phase offset and skew range estimation. A combined CRLB can be derived that contains both estimates as well as mutual influences (A.1.4). The bounds for range and velocity estimation in dynamic scenarios are given by

$$\mathrm{var}_{\mathrm{CS,D}}(R_{\mathrm{f}}) \gtrapprox \frac{57c^2}{8\pi^2 B^2 \eta N_{\mathrm{c}} N_{\mathrm{s}}}, \tag{4.23}$$

$$\mathrm{var}_{\mathrm{CS,D}}(R_{\mathrm{fin}}) \gtrapprox \frac{13c^2}{(4\pi)^2 f_{\mathrm{min}}^2 \eta N_{\mathrm{c}} N_{\mathrm{s}}}, \tag{4.24}$$

and

$$\mathrm{var}_{\mathrm{CS,D}}(\widehat{v}) \gtrapprox \frac{57c^2 f_{\mathrm{s}}^2}{8\pi^2 f_{\mathrm{min}}^2 \eta N_{\mathrm{c}}^3 N_{\mathrm{s}}}, \tag{4.25}$$

where $N_{\mathrm{c}}, N_{\mathrm{s}} \gg 1$.
The dependencies of R_{f} and R_{fin} resemble those observed in the static scenario. The dominant factors are bandwidth and minimum frequency, respectively, while N_{c} and N_{s} contribute equally. For the CRLB of v, the primer dependence is on N_{c} while N_{s} influences the bound in the same manner as it does for range estimation. A second strong dependency arises from f_{min}, reflecting the relation between Doppler shift and velocity through the transformation of parameters. Apart from these impacts, the CRLBs for R_{f} and v are structurally equal as both result from frequency analysis.

This CRLB gives a bound for the estimated velocity of the target. For an ideal estimator, the variance of velocity and velocity error would coincide as

$$\mathrm{var}(\delta v) = \mathrm{var}(\widehat{v} - v_{\mathrm{set}}) = \mathrm{var}(\widehat{v}) + \mathrm{var}(v_{\mathrm{set}}) = \mathrm{var}(\widehat{v}), \tag{4.26}$$

with the nominal velocity v_{set}. Generally, however, $\mathrm{var}(\widehat{v}) \neq \mathrm{var}(\delta v)$, as the estimation is not perfectly unbiased and estimated and nominal velocities are not completely uncorrelated. This implies

$$\mathrm{var}(\delta v) = \mathrm{var}(\widehat{v}) + \mathrm{var}(v_{\mathrm{set}}) - 2 \cdot \mathrm{Cov}(\widehat{v}, v_{\mathrm{set}}), \tag{4.27}$$

and the correlation is hard to quantify as it depends on both the measurement and the reference system. The variance of the velocity error is hence considered without clear relation to the variance of the velocity as an additional characterization parameter.

These derivations contextualize the achievable estimation accuracy for range and velocity and will be transferred to artificial Doppler shifts in Ch. 5.1.

4.2 Simulative Analysis of Estimation Capability

The performance of the discussed $f\varphi$ range estimation is at first investigated in simulations. They are mainly utilized to systematically optimize the applied signal processing with regard to hyperparameters such as used window functions or the number of CZT iterations while avoiding to optimize for a specific set of measurements. Further, implications and error sources that are hardly separable in measurements are investigated based on simulations that emulate the measurements. Radar parameters are taken from the configuration given in Table 3.1 to best mimic measurements.

4.2.1 Accurate Static Range Estimation

As an ideal, although unrealistic, reference, the radar signal is simulated for a single target without noise or any additional effects, and the results are depicted in Fig. 4.5 for frequency and $f\varphi$ analysis. The alternating patterns are the result of bin effects.
For ranges in the center of a bin, the error theoretically vanishes, and reaches a maximum at the boundary between two bins. For the range estimation after only

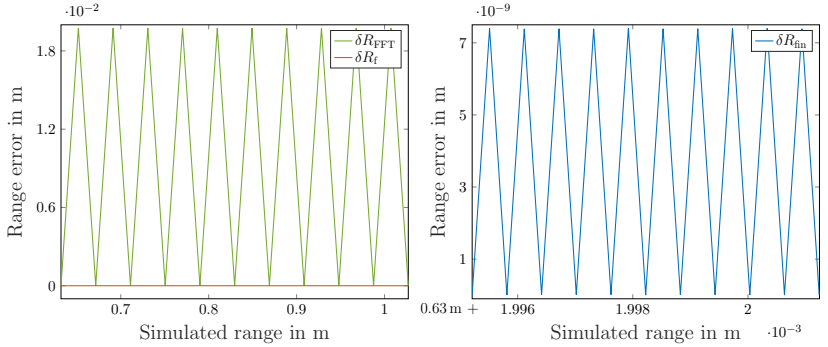

Figure 4.5: Simulated range error for frequency (a) and $f\varphi$ estimation (b) over simulated range in steps of half the respective resolution ($\Delta R = 0.04\,\mathrm{m}$, $\Delta R_{\mathrm{fin}} = 6.0 \cdot 10^{-7}\,\mathrm{m}$). Only a single target with no noise or any other effects is simulated to visualize bin effects and the theoretical potential of the proposed $f\varphi$ range estimation.

an FFT in Fig. 4.5a, the range is simulated in steps of half the FFT resolution,

$$\frac{\Delta R}{2} = \frac{c}{4B}, \tag{4.28}$$

starting at an integer multiple of the FFT resolution. The evaluated range proceeds successively over the center of a range cell and the transition between two range cells. The range error consequently alternates between zero and a maximum value of $\frac{\Delta R}{2}$. An additional CZT at these ranges improves the range estimation to zero range error as also shown in Fig. 4.5a. However, this is only the case for ranges in the center of a CZT bin; the bin effect for the CZT is masked by the large FFT steps but generally present with

$$\delta R_{\mathrm{f}} \in \left[0, \frac{\Delta R_{\mathrm{f}}}{2}\right] = \left[0, 3.0 \cdot 10^{-7}\,\mathrm{m}\right] \tag{4.29}$$

for two CZT iterations. These values are theoretical results not achievable in non-ideal simulations or measurements as systematic effects restrict the CZT. For the $f\varphi$ range estimation in Fig. 4.5b, the range is simulated in steps of

$$\frac{\Delta R_{\mathrm{fin}}}{2} = \frac{\Delta R}{2{N_{\mathrm{s}}}^{w}} = \frac{\Delta R_{\mathrm{f}}}{2}, \tag{4.30}$$

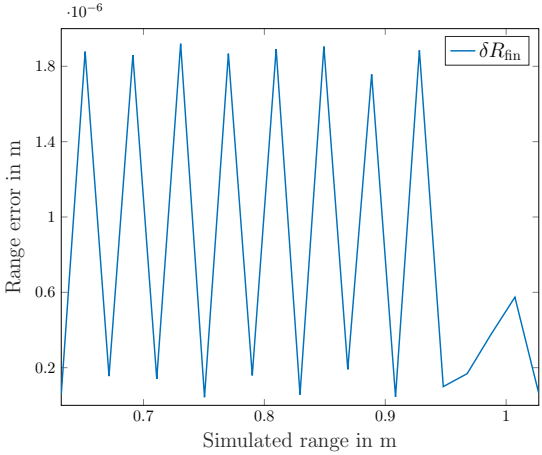

Figure 4.6: Simulated range error over simulated range for $f\varphi$ range estimation. AWGN is included in the simulation that is in all other aspects equal to Fig. 4.5.

which corresponds to half the bin size of the CZT with w iterations. Two CZT iterations are utilized and the starting point is chosen equal to Fig. 4.5a. A similar pattern is observed as for frequency-based estimation, however, due to the small step size, the estimation is within the first step in Fig. 4.5a. The periodicity of the occurring bin effect is dominated by the CZT that determines the step size of the combined estimation. The achievable range error, however, is defined by the phase-offset analysis, but taking into account the CZT iterations with

$$\delta R_{\mathrm{fin}} \in \left[0, \frac{c}{2 \cdot 4 f_{\mathrm{min}} N_{\mathrm{s}}{}^{w}}\right] = \left[0, 7.4 \cdot 10^{-9}\,\mathrm{m}\right]. \tag{4.31}$$

The maximum error is dependent on the number of CZT iterations according to (4.31), however, the influence is mostly observable in ideal simulations, as soon as additional effects are included, other factors limit the achievable accuracy for more than two CZT iterations. Thus, two iterations are used hereinafter. The additional bisection stems from the rounding function in (4.4), that restricts the final range estimate to half a bin, limiting the error to its quarter.

From the impressively low range error in nm scale, the potential of this signal processing approach is evident. It is not realistic to achieve such high accuracy in measurements, not even if optimized hardware and perfectly controlled

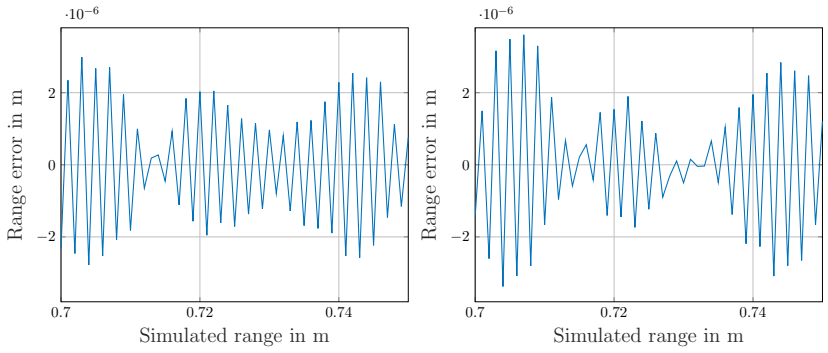

Figure 4.7: Simulated range error over simulated range for $f\varphi$ analysis, including noise and the first multiple reflection of the target (a) and an additional independent target reflection (b). The superposition of signal components results in a beat phenomenon for both cases.

measurement surroundings would be available. This is apparent from Fig. 4.6, showing the results of simulations including only AWGN in dependency of the target range. The noise is determined from the SNR, calculated from the radar parameters of the AWR1843BOOST as used in the measurements. In all other respects, the simulation is equivalent to the one performed for Fig. 4.5. The results reveal the significant influence of noise as the range error shifts from nm to µm. The bin effect is still pronounced, however, R_{fin} is limited by the preceding frequency analysis and the pattern in Fig. 4.6 adopts the periodicity of frequency analysis in Fig. 4.5a, although with much smaller amplitude. The advantage of $f\varphi$ analysis therefore remains, but its systematic behavior is dominated by frequency analysis. While the regular pattern is clearly included, it is slightly disturbed in amplitude over the complete range and also in periodicity at around 1 m. As a single simulation iteration is performed for each range, these effects are attributed to noise influences. In repetitive simulations, similar disturbances occur at different ranges, indicating that they result from a significant noise contribution rather than being characteristic of a certain simulated range. However, the pattern remains, despite such disturbances, regular also over wider ranges and in all repetitions.

Figure 4.7 depicts simulation results mimicking the measurements not only regarding radar parameters, but also absolute range and range steps, used

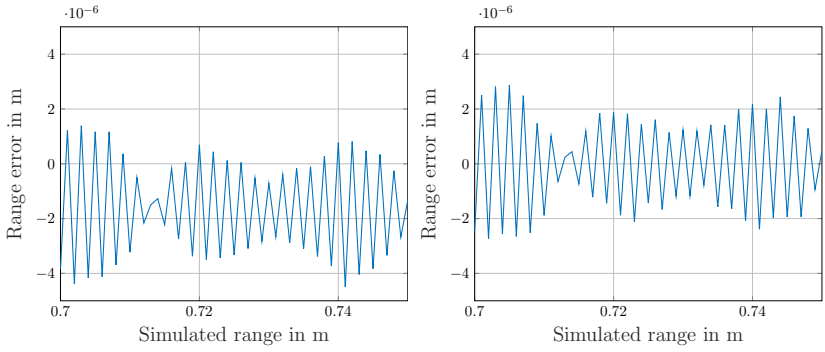

Figure 4.8: Simulated range error over simulated range for $f\varphi$ analysis, including noise, the first multiple reflection of the target, and Doppler estimation and correction for a simulated velocity of 0 m/s (a) and 1 m/s (b).

henceforth. The first multiple reflection of the target is included in Fig. 4.7a, causing a beat due to the superposition of two signal components, direct target reflection and multiple reflection. The bin effect as well as the simulated ranges have influence on the occurring beat pattern. Additionally simulating an independent second target of the same signal strength in Fig. 4.7b demonstrates the susceptibility of the beat pattern to present signal components, although the overall range error is not significantly increased. These three aspects, noise, multiple reflections, and unintended targets, are the main influence factors on $f\varphi$ range estimation in static scenarios.

4.2.2 Range and Velocity Estimation under Doppler Influence

In dynamic scenarios, the occurring Doppler shift, its estimation, and correction present a challenge for range estimation. This is obvious from simulations not including a Doppler shift ($v_{\mathrm{sim}} = 0\,\mathrm{m/s}$) in Fig. 4.8a, where the $f\varphi$ range estimation is structurally equivalent to simulation results without Doppler correction in Fig. 4.7a, but biased from zero mean. Applying a non-zero Doppler shift even improves range estimation as the offset vanishes, exemplified in Fig. 4.8b

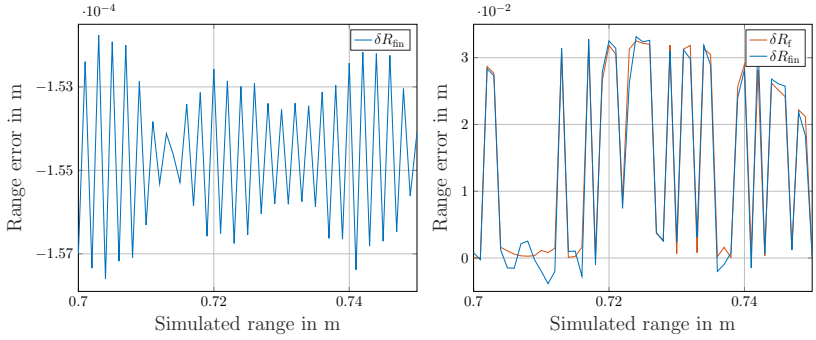

Figure 4.9: Simulated range error over simulated range for a simulated velocity of 1 m/s. In (a), the velocity estimate after FFT is used for Doppler correction while in (b), no Doppler correction is applied.

for $v_{\mathrm{sim}} = 1\,\mathrm{m/s}$. This is attributable to a slight offset in Doppler estimation after CZT, occurring for $v_{\mathrm{sim}} = 0\,\mathrm{m/s}$. If the velocity estimate after an FFT, which is $\widehat{v}_{\mathrm{FFT}} = 0\,\mathrm{m/s}$, is used for Doppler correction instead of applying an additional CZT, no offset occurs in range estimation as for $v_{\mathrm{sim}} = 0\,\mathrm{m/s}$, $\widehat{v}_{\mathrm{FFT}}$ is more accurate. However, it results in significantly deteriorated estimations for $v_{\mathrm{sim}} \neq 0\,\mathrm{m/s}$ (Fig. 4.9a). Estimations are structurally similar to correction with $\widehat{v}_{\mathrm{CZT}}$ (Fig. 4.8b), however, a strong bias deteriorates range estimation. As the effect for zero Doppler is masked by dominant phenomena in measurements, $\widehat{v}_{\mathrm{CZT}}$ is used for Doppler correction hereinafter. If no Doppler correction is applied (Fig. 4.9b), $f\varphi$ range estimation cannot improve the results of frequency analysis as the accuracy of the latter is not sufficient to identify the correct range bin. As a result, range errors of multiple cm occur for both frequency-based and combined estimation and the estimated ranges are similar to equal.

But proper velocity estimation is not only required for highly accurate and undisturbed range estimation. Beyond pure knowledge about this target parameter, it can be utilized for advanced applications such as target tracking or hypothesis testing. Similar bin effects as discussed regarding range estimation

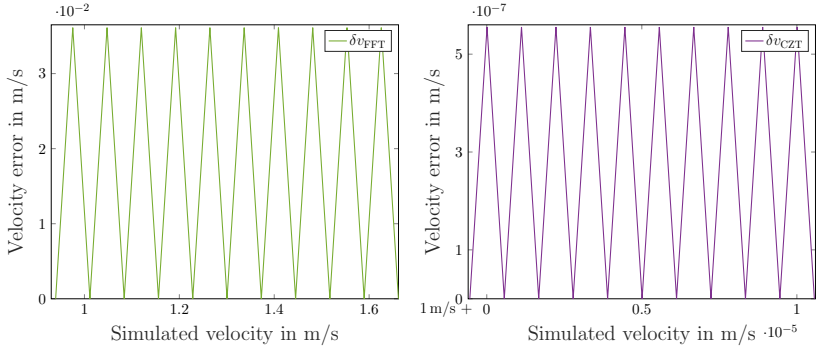

Figure 4.10: Simulated velocity error for FFT- (a) and CZT-based estimation (b) over simulated velocity in steps of half the respective resolution ($\Delta v = 0.07\,\mathrm{m/s}$, $\Delta v_{\mathrm{CZT}} = 1.1 \cdot 10^{-6}\,\mathrm{m/s}$), visualizing bin effects.

are observed. For the FFT-based velocity estimation in Fig. 4.10a, the velocity is simulated in steps of half the velocity resolution

$$\frac{\Delta v}{2} = \frac{c}{4 N_{\mathrm{c}} T_{\mathrm{cr}} f_{\mathrm{min}}}, \tag{4.32}$$

starting at an integer multiple of this resolution close to 1 m/s. The evaluated velocity proceeds successively over the center of a Doppler cell and the transition between two Doppler cells, while the velocity error alternates between zero and its maximum value $\frac{\Delta v}{2}$.
Similarly, velocity estimation from CZT contains an alternation in steps of

$$\frac{\Delta v_{\mathrm{CZT}}}{2} = \frac{\Delta v}{2 N_{\mathrm{c}}^{w}} \tag{4.33}$$

with

$$\delta v_{\mathrm{CZT}} \in \left[0, \frac{\Delta v_{\mathrm{CZT}}}{2}\right] = \left[0, 5.6 \cdot 10^{-7}\,\mathrm{m/s}\right], \tag{4.34}$$

shown in Fig. 4.10b for $w = 2$. Results and dependencies are very similar to range investigation and will be further transferred to artificial Doppler shifts in Ch. 5.

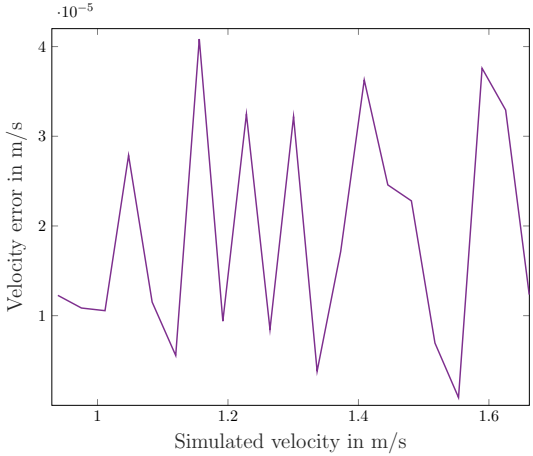

Figure 4.11: Simulated velocity error for CZT-based estimation over simulated velocity including AWGN and the first multiple reflection.

As for range estimation, these results are not reached in non-ideal simulations or measurements. Analyzing CZT-based velocity estimation in a more realistic simulation in Fig. 4.11, including the same effects as in Fig. 4.7a, reveals increased velocity errors. The major share of increase stems from the noise influence, multiple reflections only slightly impair velocity errors. The alternating pattern is disturbed by noise, multiple reflections, and, in this visualization, also the simulation of velocities in steps of the FFT resolution to cover larger velocities. Despite the observed deterioration, range estimation is not impeded as ascertained in Fig. 4.8b and the gained velocity estimate is still well-suited for direct usage.

4.2.3 CRLB Comparison

Figure 4.12 illustrates the comparison between the approximated CRLB for phase-based range estimation in (4.10) and the achieved variance in simulations

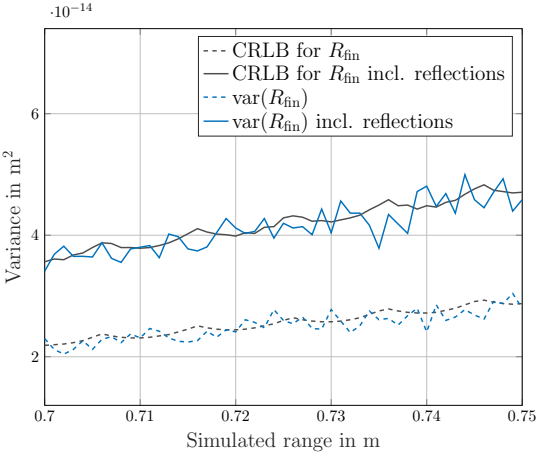

Figure 4.12: Approximated CRLB and variance of simulated range estimation including only noise (dashed) and noise as well as multiple reflections (solid).

including only noise and noise as well as multiple reflections, both using 1000 iterations. The variance is defined as

$$\text{var}(\widehat{R}) = \frac{1}{N_{\text{it}} - 1} \sum_{i=1}^{N_{\text{it}}} | R_i - \overline{R} |^2, \tag{4.35}$$

including Bessel's correction [UC14]. N_{it} is the number of iterations and $\overline{R}$ describes the mean of R according to

$$\overline{R} = \frac{1}{N_{\text{it}}} \sum_{i=1}^{N_{\text{it}}} R_i. \tag{4.36}$$

As the simulations do not contain additional targets, the SNR is estimated from the simulation results and used for calculating the CRLB. It hence differs for the two scenarios and over the simulated ranges, while all other parameters are taken as simulated. The CRLB is calculated according to (4.10) for both curves. As the SNR in the scenario including multiple reflections is slightly decreased compared to the noise-only case, an increase in CRLB as well as variance is observed. For both cases, the variance varies around the CRLB. As stated before, the CRLB derivation assumes an unbiased estimator which is

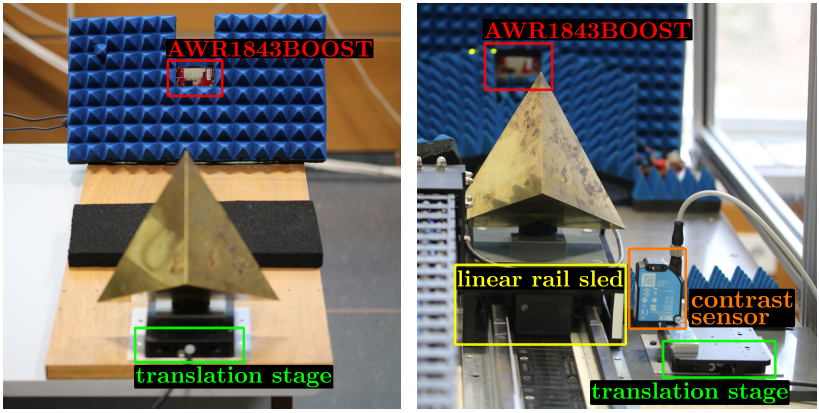

(a) (b)

Figure 4.13: Measurement setup with the radar sensor facing a corner reflector in a static (a) and a dynamic setup (b). In the static setup, the corner is mounted on a translation stage, but only moved in between, not during measurements. In the dynamic setup, the corner is mounted on a linear rail sled moving during measurements and the contrast sensor on the translation stage next to it triggers each measurement in passing.

not reached, in simulations mostly due to the bin effect. As a result, deviations from the CRLB in both positive and negative directions are to be expected even though it is a lower limit as discussed in Ch. 4.1.1. In general, the simulation iterations are very similar to each other as the scenario is perfectly deterministic and remains unchanged in between the simulation runs and even the simulated AWGN is only pseudo-random. Thus, the resulting range estimations are also very similar, and their variance is significantly smaller than to be expected from measurements, where in addition to occurring non-modeled signal components, environmental influences may change, and with a corner reflector, a distributed target is used.

4.3 Metrological Verification

To appraise the conducted simulations and found dependencies, measurements are performed aiming at expressive validation in the static and dynamic scenarios depicted in Fig. 4.13.

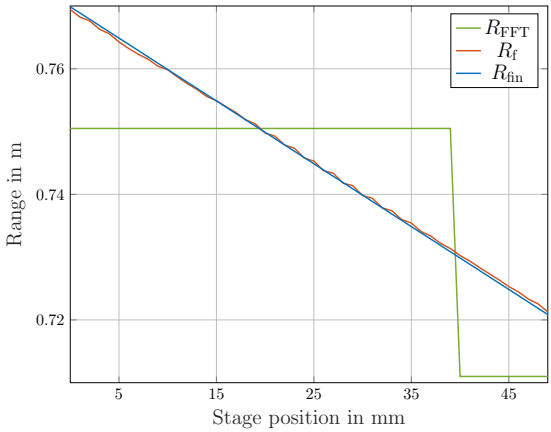

Figure 4.14: Measured range over 50 stage positions after FFT, CZT, and $f\varphi$ analysis.

4.3.1 Accurate Static Range Estimation

The $f\varphi$ range estimation is first verified in a static laboratory setup. The radar target is a trihedral corner reflector with a side length of 14 cm. As the dimensions are large in comparison to the wavelength, it can be approximated as a point target at its center [JRM10].
An AWR1843BOOST (Ch. 3.1.1) radar is used with the measurement parameters previously applied in simulations and given in Table 3.1. No calibration is performed, hence, relative accuracy is provided as discussed in Ch. 2.2.2. The range error is calculated as the deviation of the range estimates of two measurements at defined distance Λ according to

$$\delta R = \widehat{R} - \widehat{R}_{\mathrm{ref}} - \Lambda. \tag{4.37}$$

The corner reflector is mounted on the M-683 precision translation stage (Ch. 3.2.1) and incrementally moved toward the radar within the measurement range of 50 mm in steps of $\Lambda = 1\,\mathrm{mm}$. The distance between corner and radar starts at approximately 0.75 m and decreases accordingly. Absorber material is used to suppress reflections from the wooden plate between radar and corner and the front side of the translation stage as well as multiple reflections to have one main target with all other reflections being considerably weaker.

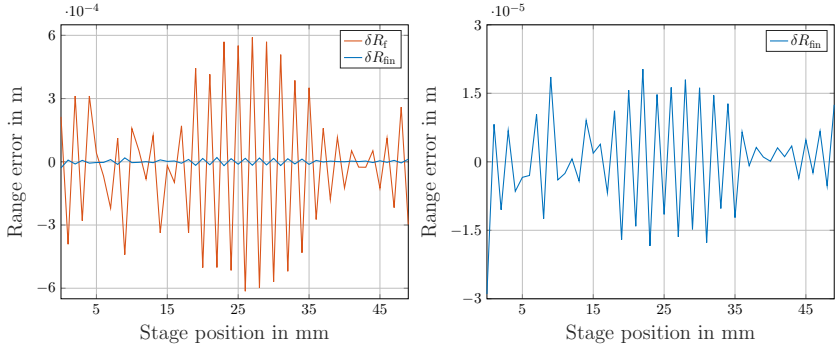

Figure 4.15: Range error over a measurement range of 50 mm in an all-static scenario for frequency (a) and $f\varphi$ analysis (b), revealing a distinctive beat in both estimations.

Environmental influences remain but no further processing optimizing estimation results, such as background compensation, is applied as it is not reliably applicable in real scenarios, which may contain dynamics both in the target and its surroundings. The complete measurement setup for the static scenario is shown in Fig. 4.13a.
Although constant during measurements, the measured range decreases linearly with the steps of the translation stage. This behavior is observable in Fig. 4.14 for frequency and $f\varphi$ analysis, while the FFT only provides a very coarse range estimation that approximates the linear curve in steps of ΔR. Deviation from the true distance is due to the lack of calibration, but only adds a constant offset not affecting the range error in relative evaluation according to (4.37).

After frequency analysis, small ripples occur in R_f, better visible in Fig. 4.15 that depicts the range error after frequency and combined analysis. The direct comparison emphasizes the accuracy advance of $f\varphi$ estimation but also demonstrates the relation between both analyses. As $f\varphi$ range estimation builds on frequency analysis, influence factors and therefore, deviations, are transferred although the requirement of $\delta R_\mathrm{f} \in \left[-\frac{c}{4f_\mathrm{min}}, \frac{c}{4f_\mathrm{min}}\right] \approx \left[-9.7 \cdot 10^{-4}\,\mathrm{m}, 9.7 \cdot 10^{-4}\,\mathrm{m}\right]$ is met in all stage positions. Nevertheless, the achieved range errors for $f\varphi$ estimation are considerably below those of frequency analysis. The beat pattern occurring for both estimations is very similar to the one observed already in simulations and hence most likely originating from multiple target reflections.

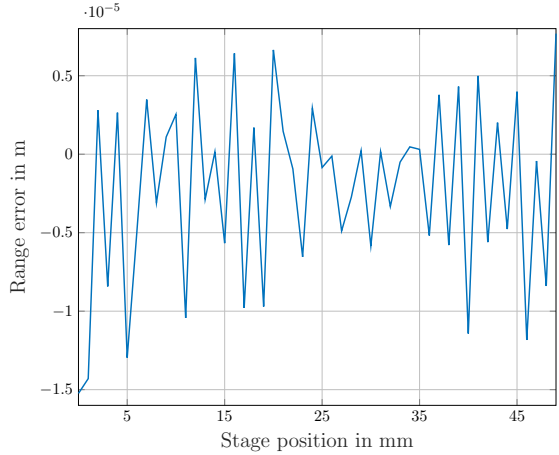

Figure 4.16: Range error after $f\varphi$ analysis in a setup optimized to reduce multiple reflections. Significantly smaller errors and less beat are observed in comparison to Fig. 4.15b.

If the setup is thus optimized to suppress multiple reflections, the beat is reduced, resulting in decreased range errors as shown in Fig. 4.16, however, the beat impact is still observable. For this measurement, a signed mean error $\overline{\delta R_{\text{fin}}}$ of $-2.2\,\mu\text{m}$ is achieved while the absolute mean error $\overline{|\delta R_{\text{fin}}|}$ is $4.8\,\mu\text{m}$. The signed mean error $\overline{\delta R_{\text{fin}}}$ over the stage positions indicates the balance of error values whereas the absolute mean error $\overline{|\delta R_{\text{fin}}|}$ better specifies deviations from ground truth. Figure 4.16 hence contains balanced range estimates, however, including a negative bias, and small absolute errors.
These are promising results rarely yet achieved in comparable free-space setups without particularly high bandwidths. They impressively demonstrate the capabilities of the proposed analysis and, together with the systematic error pattern, the high correlation between measurements and corresponding simulations, which are consequently well suited for predictions about the expectable performance.

The estimation results are stable across the number of measurement iterations as shown in Fig. 4.17, depicting the mean of 1000 iterations and its standard deviation, visualized as error bars. The stability of the range error and particularly of the contained beat proves robust performance, but also underlines the dominance of systematic errors while random processes are minor. Averaging over

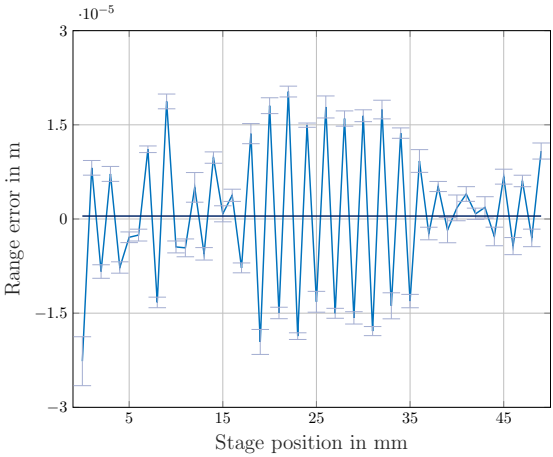

Figure 4.17: Mean range error after $f\varphi$ analysis with standard deviation (error bars) and mean over all measurement positions (dark blue) for 1000 measurement iterations. Errors are well-balanced and hardly varying over the iterations, indicating robust estimation performance.

all positions, zero mean is approximately reached ($\overline{\delta R_{\mathrm{fin}}} = 0.5\,\mu\mathrm{m}$), indicating well-balanced estimations without bias.

The variance over multiple measurement iterations is the second evaluation criterion of accuracy, describing the precision of the estimation. The question arises, how many iterations are required for a qualitative statement about this precision. The maximum number of iterations recorded for a setup is 1000, which showed good accordance with a single measurement and small deviations in Fig. 4.17. However, this high number of iterations is not viable for all setups and not required as shown in Fig. 4.18a. The variance of range estimation is depicted for 100, 300, and 1000 iterations. The lower numbers are taken as parts of the 1000 iterations, thereby avoiding other influences to affect the comparison. The variance continuously decreases for more iterations as shown in Fig. 4.18b for additional intermediate terms. This is mostly attributable to statistical effects and the drift of radar parameters diminishing over time as the temperature approaches a constant value (Ch. 3.1.1). However, the structure of the variance is very similar for 100 to 1000 iterations, so that qualitative statements are possible. Further, the decrease is slow and not spanning significant

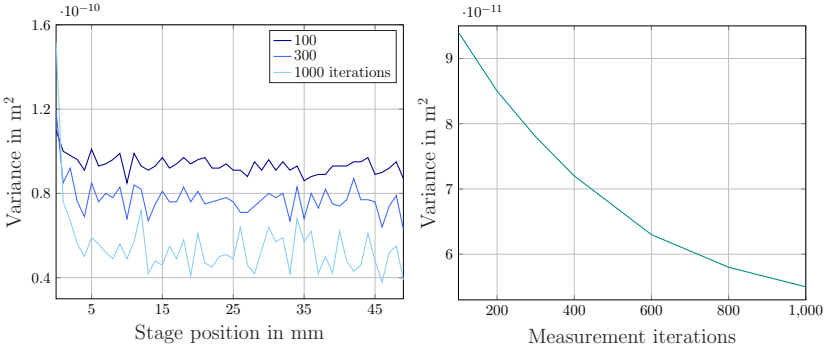

Figure 4.18: Variance of range estimation over a measurement range of 50 mm for 100, 300, and 1000 iterations (a) and over the number of iterations, averaged over the measurement range (b). Variances hardly differ over the number of iterations and 100 iterations are used henceforth.

orders of magnitude, hence allowing for a rough qualitative placement. Already 100 iterations thus contain valuable information about the accuracy in terms of (mean) error and variance and are used hereinafter for both static and dynamic scenarios.

4.3.2 Range and Velocity Estimation under Doppler Influence

In order to build a dynamic scenario, the measurement setup is adjusted as shown in Fig. 4.13b. The corner reflector is mounted on the sled of a linear rail (Ch. 3.2.3) which is accelerated to a nominal velocity v_{set} and moves the corner away from the radar. A contrast sensor (KTS-WB9114115AZZZZ from SICK) is installed next to the sled on the translation stage (Ch. 3.2.1), measuring a change in contrast from the precalibrated value. Thereby, when the sled passes by the contrast sensor, a measurement is triggered using the hardware trigger of the radar. Next, the contrast sensor is moved by $\Lambda = 1\,\mathrm{mm}$ and a new measurement is conducted to allow for relative evaluation. The setup minimizes variations in measurement starting times, however, they cannot be completely eliminated. The used contrast sensor has a jitter of its response time

of 3 µs [SIC24]. The trigger signal for the radar sensor is generated from the contrast sensor input using a custom adapter board. The occurring variations in this part of the setup are measured to be within 0.2 µs. The hardware trigger uncertainty is specified to be 5 ns [Tex20]. All timing variations add up and affect the range estimation as the target has already moved further and is at a larger distance for a delayed measurement. The variations add up to approximately 3.2 µs, which translates to a range error of up to 9.6 µm at 3 m/s and is hence to be considered in the interpretation of measurement results. However, this is a worst-case consideration and not observed to this degree. The overall time delay, on the other hand, is not problematic as long as the sled is in constant motion within the evaluated frame. In that case, a constant delay cancels out in the relative evaluation.

The range error is evaluated according to (4.37) while for the velocity error, absolute reference values are used according to

$$\delta v = \widehat{v} - v_{\mathrm{set}}. \tag{4.38}$$

As the nominal velocity is not provided by an external reference system, the motor control of the rail affects error progression. Oscillations in the actual velocity around the setpoint value, caused by the motor control, are contained in the velocity estimation, but not considered in the reference, so that the error also contains these oscillations. Not visible in most other measurement setups and in static scenarios, the combination of small-range steps and fine velocity resolution unveils them. To investigate their behavior, a second measurement setup is built and velocity estimations are compared. Only the linear rail is used, and the sled moves along the rail at velocities $v_{\mathrm{set}} = 1$ to $3\,\mathrm{m/s}$ while a continuous radar measurement captures the entire movement as depicted in Fig. 4.19a. The measurement parameters are adjusted to achieve a very short frame periodicity of only 3 ms, so that each frame corresponds to a movement of 3 to 9 mm at 1 to 3 m/s. The start of the measurement is triggered manually and contains no further information. The velocity error is determined, and excerpts of it of 50 mm length are used for comparison. In Fig. 4.19b, these excerpts are manually matched to the oscillations recorded in the first setup and show comparable frequencies and amplitudes. The motor control oscillates at the same temporal frequency for all velocities while meanwhile the target travels a longer distance at higher velocities, resulting in different spatial oscillation frequencies for the associated velocity errors over distance. As a result of the

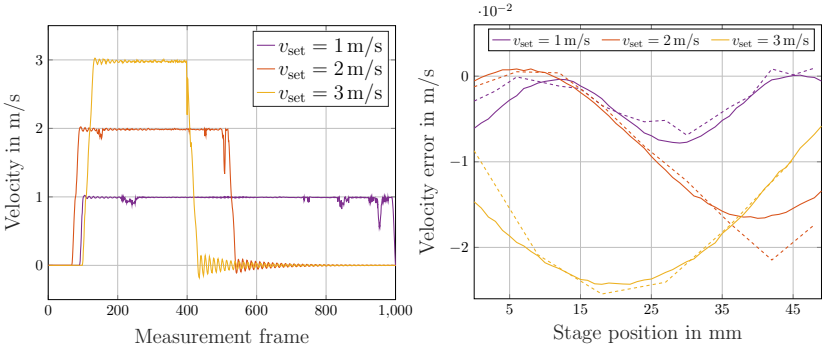

(a) (b)

Figure 4.19: Velocity measurement for a target at 1, 2, and 3 m/s in steps of 3 to 9 mm (a) and corresponding velocity error (b). The measurement starts at rest and covers acceleration to v_{set}, movement at this velocity with oscillations caused by the motor control, and braking to a standstill. The velocity error (dashed) is compared to the error of measurements in steps of 1 mm, recorded with the setup from Fig. 4.13b (solid).

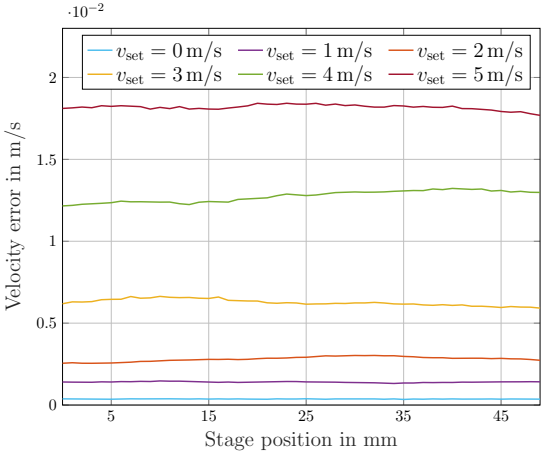

Figure 4.20: Velocity error over a measurement range of 50 mm for a static target as well as velocities of 1 to 5 m/s. The starting position of the sled is moved according to the position of the contrast sensor for each measurement to suppress the motor control oscillations observed in Fig. 4.19b.

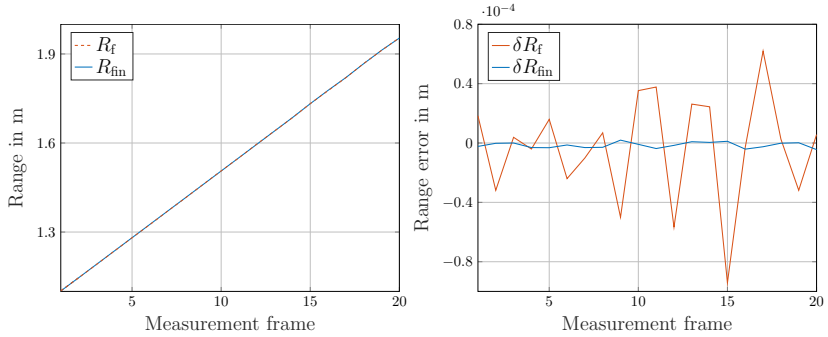

Figure 4.21: Estimated range (a) and range error (b) over 20 consecutive frames using frequency-based and $f\varphi$ range estimation. The target is moving away from the radar with 1 m/s.

oscillations in velocity, the range oscillates as well, but with a phase shift of 90° due to the integration connecting velocity and range.

To suppress the influence of the motor control, the starting position of the sled is moved according to the position of the contrast sensor before a new measurement is triggered. In this way, the distance between the sled start and the contrast sensor release point remains approximately equal for all measurements. The motor control of the sled is hence always at the same point and does not superimpose with the estimation results anymore. However, absolute deviations from the assumed nominal velocity remain and affect the velocity error. Fig. 4.20 shows the measured velocity error for six velocities $v_\mathrm{set} = 0$ to $5\,\mathrm{m/s}$ and 50 stage positions. The static measurement is conducted at the initial range of each stage position and evaluated including Doppler estimation and correction. A mean velocity error $\overline{|\delta v|}$ of 0.4 mm/s is reached, whereat evaluation without Doppler consideration does not result in significantly different results for the static case. The velocity error differs for the five non-zero velocities and is in significant excess of the static scenario. It rises with higher velocities from $\overline{|\delta v|} = 1.4\,\mathrm{mm/s}$ at 1 m/s to $\overline{|\delta v|} = 18\,\mathrm{mm/s}$ at 5 m/s. Additionally, a slight oscillation remains as the motor control is not perfectly suppressed. This is better visible for higher velocities where the amplitude of the oscillation is larger as depicted in Fig. 4.19b. The larger amplitudes of oscillations also contribute to larger velocity errors at higher velocities, however, this can only

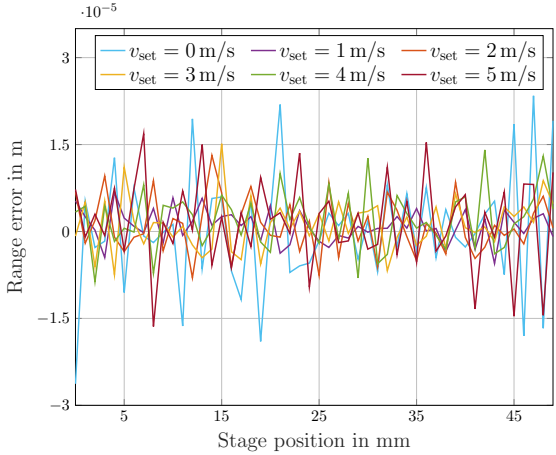

Figure 4.22: Range error over a measurement range of 50 mm for a static target as well as velocities of 1 to 5 m/s, all experiencing comparable estimation performance.

in part explain the deterioration. Although there are a number of other effects caused by the measurement setup, it mainly demonstrates the limitations of the performed Doppler estimation. However, the influence on range estimation is limited as long as the oscillation of the motor control is sufficiently suppressed and Doppler shifts are corrected during processing.

A range estimation over 20 consecutive frames for $v_{set} = 1\,m/s$ is depicted in Fig. 4.21a, showing the linear movement of the target away from the radar. No difference between the estimated ranges R_f and R_{fin} can be observed due to the coarse y-axis scaling. This is only possible from Fig. 4.21b, depicting the corresponding range errors. $f\varphi$ estimation achieves significantly lower errors, although frequency-based estimation is already quite exact as a result of the optimization performed to comply with the error limits of $\frac{c}{4f_{min}} = 9.7 \cdot 10^{-4}\,m$ for phase-offset-based analysis. The range error is, despite random variations, independent of the evaluated frame for both estimations, which is important for applications requiring estimation over time, such as tracking.

In Fig. 4.22, the range error is shown for the six velocities considered prior. Excellent range errors with signed means $\overline{\delta R_{fin}}$ of 0.9 to 2.0 µm and absolute means $\overline{|\delta R_{fin}|}$ of 2.3 to 6.1 µm for 1 to 5 m/s are achieved despite motion. The

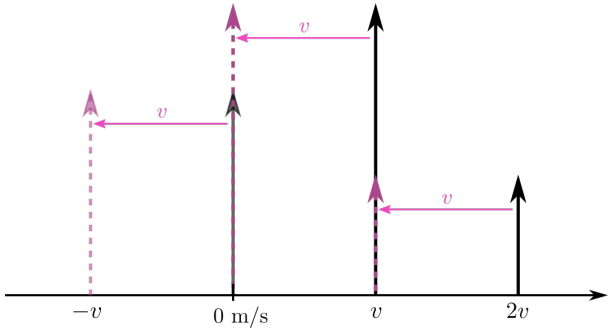

Figure 4.23: Schematic representation of Doppler correction for a single target at v and its first multiple reflection at $2v$. All signal components are shifted equally by v, resulting in the target peak at zero velocity and multiple reflections and static clutter at $\pm v$.

distinctive double peaks with inverted amplitude, e.g., around stage position 20 mm, are typical for the relative measurement evaluation where each measurement is used twice, but errors contribute with an inverted sign.

For the range estimation of moving targets, an interesting effect occurs as a slightly higher accuracy is achieved compared to the static scenario, however, errors are less balanced. This is evident from the absolute mean errors of 7.7 and 2.3 µm for 0 and 1 m/s, respectively, as well as signed errors of −4.6 nm and 0.9 µm for the same velocities. The absolute improvement stems from the chirp summation prior to range estimation. As a consequence of this summation, the achieved SINR for a moving target is higher than in a static scenario due to the presence of multiple static targets in the surroundings. If the target of interest is static as well, the targets can be separated but interfering peaks lower the SINR. The same applies to multiple reflections. If the target of interest is in motion, the discussed Doppler correction shifts the whole spectrum in the Doppler domain by the detected Doppler shift as delineated in Fig. 4.23. The peak of the moving target shifts to zero velocity, while all static targets are shifted to the inverted target velocity. Multiple reflections are shifted equally, but as they experienced the Doppler shift multiple times from multiple reflections on the moving target, they contain a Doppler shift related to their multiplication factor after correction. When the chirps are summed, all spectrum parts containing a Doppler shift sum up incoherently due to their phase shift to each other and are effectively suppressed. The peak at zero Doppler sums coherently, resulting

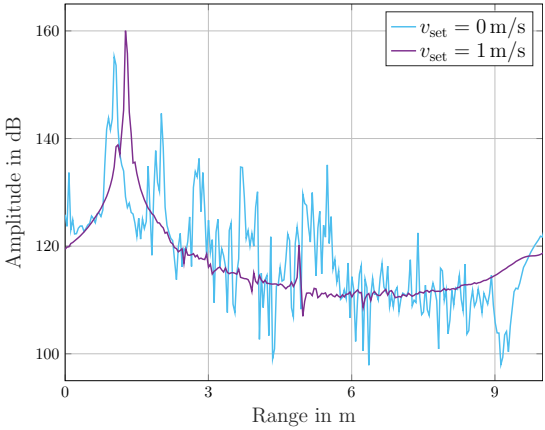

Figure 4.24: Range profile after Doppler correction and chirp summation for a target with 0 and 1 m/s, respectively. The moving target appears at a larger range due to the time delay between contrast sensor release and measurement start.

in a higher amplitude compared to a single chirp and a very clean spectrum with hardly any other spectral components. This is shown in Fig. 4.24, where the range profiles after chirp summation of a static and a moving target are compared and the enhanced SINR is observable. The same stage position is depicted, but the moving target appears at a slightly larger range due to the time delay between contrast sensor release and measurement start.
Using this correction significantly augments range estimation capabilities for moving targets. The improvement is particularly prominent at 1 and 2 m/s, for increasing velocities, the effect is countervailed by increasing velocity errors. Consequently, range errors deteriorate for higher velocities as observed in Fig. 4.20 and 4.22, but remain below those of a static scenario and still feature excellent values.

The Doppler correction works well and enables high-accuracy range estimation, however, deviations in the Doppler estimation affect range estimation as derived mathematically in (4.7). Although the phase offset itself is not prone to Doppler shifts, a larger velocity error results in a larger range error. This correlation is investigated in more detail with an artificially deteriorated velocity estimation. Fig. 4.25 depicts the mean of the range error of frequency-based and $f\varphi$ range estimation over the 50 stage positions for the measurements with 1 m/s. An

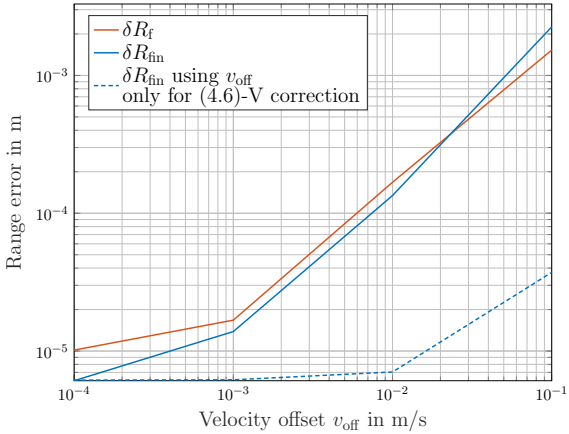

Figure 4.25: Mean of absolute range error across 50 stage positions with $v_\mathrm{set} = 1\,\mathrm{m/s}$ for frequency-based and $f\varphi$ range estimation over different offsets v_off on the Doppler estimation (solid). Additionally, the investigation with the same offsets only applied for the correction of the (4.6)-V term and the quadratic share of the phase offset is shown for $f\varphi$ range estimation (dashed).

increasing velocity offset v_off is added to the estimated velocity to emulate corrupted estimation. While small offsets hardly influence range estimation, larger v_off drastically increase the range error to a level where an incorrect range bin is chosen from frequency analysis and a consecutive phase-offset analysis cannot contribute to a higher accuracy. The benefit from $f\varphi$ range estimation is greatest without velocity offset. If an incorrect range bin is chosen, combined analysis can even result in larger errors than only frequency analysis.
Over all offsets, the error is primary caused by the frequency-based range estimation. To further investigate this, the defective range estimation $R_\mathrm{f,off}$, caused by v_off, is used only for the last correction of the (4.6)-V term and the quadratic share of the phase offset prior to phase-offset analysis. Apart from that, the estimate without velocity offset is used. The results are depicted as the dashed line, showing that the partly defective correction already deteriorates $f\varphi$ range estimation, but only to a mean value of 37 µm for $v_\mathrm{off} = 0.1\,\mathrm{m/s}$, whereas the same offset in the complete processing chain results in a mean range error of 2.2 mm. Reliable Doppler correction is hence crucial for range estimation, using either frequency or $f\varphi$ analysis with real or artificial Doppler shifts.

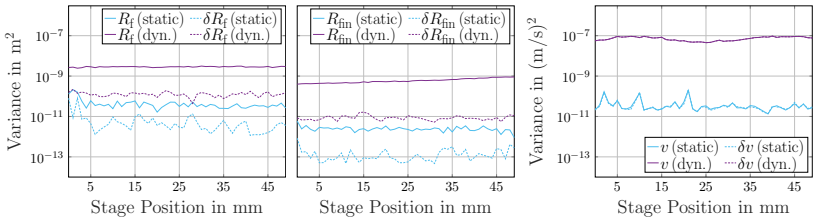

Figure 4.26: Variance of range estimation after frequency (a) and $f\varphi$ (b) analysis and variance of velocity estimation (c). For each estimation, the variance of the estimated parameter (solid) and the associated error (dashed) are depicted for a static and a dynamic (dyn.) measurement scenario.

4.3.3 CRLB Comparison

The presented estimation results shall be contextualized with a comparison of their variances. Those are determined from 100 measurement iterations of the static and the dynamic scenario each. It is distinguished between the variance of the estimation $\mathrm{var}(R)$, $\mathrm{var}(v)$ and the variance of the error $\mathrm{var}(\delta R)$, $\mathrm{var}(\delta v)$ according to (4.18) and (4.27), respectively. Fig. 4.26a presents the variances of range and range error after frequency analysis for the static and the dynamic setup. Equivalent results are given for $f\varphi$ analysis in Fig. 4.26b. Figure 4.26c provides these results for velocity estimation. As expected, variances are higher for R_f than for R_fin and the variances of the error values are by trend smaller than those of the estimated values as derived in theory. Further, changing environmental conditions and drifts in the radar parameters affect mainly the range variance as multiple consecutive measurements contribute while for the range error, only two consecutive measurements are put into relation. Although all iterations are considered for the variance, they are not directly compared, diminishing drift implications. However, there is a correlation between larger range errors and larger variances of the range error. The range estimation deviates, leading to large range errors, while deviations are not constant, resulting in a large variance of the range error. The variances in the dynamic setup are generally higher than those achieved in the static one. One reason is the setup itself, containing timing variances that transfer to range and range error likewise. Due to the motor control behavior, they can also affect velocity estimation. Additionally, the measurements are recorded at longer intervals as the motor

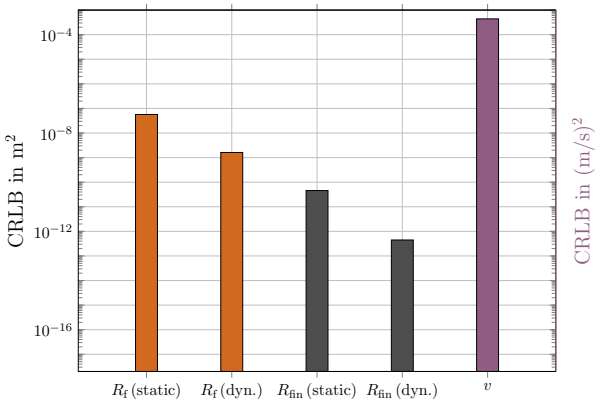

Figure 4.27: CRLBs for R_f, R_fin, and v considering a static and a dynamic (dyn.) scenario, respectively.

has to drive back and start anew. Radar and atmospheric parameter drifts are hence more pronounced and the vibrations of the rail in operation additionally add variance. Finally, regular restarts of radar, rail, and stage are required to record 100 iterations in this setup. While the difference between the variance of the estimated parameter and the corresponding error is significant for range estimation, both variances are approximately equal for velocity estimation. Particularly in the dynamic scenario, differences are negligible. The reason is the difference in error determination for range and velocity estimation as discussed prior. As the velocity is compared against a constant nominal velocity v_set and correlation is negligible, the variance of estimation and error coincide. For the dynamic scenario, remaining oscillations from the motor control are visible as these are measured, but not accounted for in v_set.

To provide a theoretical comparison for the achieved variances, the CRLBs are determined for the measured SINR and depicted in Fig. 4.27. They are computed according to (4.8) and (4.10) for the static scenario and (4.23), (4.24), and (4.25) for the dynamic scenario. The SINR is estimated from one measurement in the center motor position for each of the scenarios. The quantitative relations between the CRLBs in Fig. 4.27 are not reproduced in the measurement variances. While $f\varphi$ estimation yields smaller variances for both, static and dynamic scenarios, the variances in the dynamic scenario are generally larger

despite the larger SINR, that leads to a smaller CRLB. The SINR enhancement can therefore not compensate the increased variances from the measurement setup as discussed earlier. The variance of velocity estimation is in excess of the variance of range estimation in both scenarios, however, not as large as the CRLB would imply, indicating systematic deviations. While these can result from the motor control in the dynamic scenario, the static scenario has a clear and unimpaired nominal velocity $v_{\mathrm{set}} = 0\,\mathrm{m/s}$. The limitation for the estimation error and variance is hence the processing chain itself, which is optimized to Doppler correction and undisturbed range estimation rather than accurate and unbiased velocity estimation. The achieved velocity estimation results are, however, promising with regard to practical applications such as tracking.

The CRLBs are not and were not expected to be met. Lower variances indicate a biased estimator and non-modeled phenomena in the evaluated signal, which is not investigated further. A thorough analysis of requirements and measurements approaching the CRLB in a specially optimized setup are given in [Sch17] and are out of the scope of this work. The presented measurement setups, the used hardware, and reference systems are not elected to reach highest possible accuracy, but to show performance capabilities in realistic environments and with low-cost, commercially available hardware, which was successfully demonstrated.

4.4 Functional Requirements and Limitations

For the $f\varphi$ estimation providing the high accuracy demonstrated so far, there are few real requirements, however, different parameters can limit the reached accuracy. Single-sideband mixing in the radar receiver is essential to extract the phase offset. Phase reconstruction from a real-valued signal was investigated, but did not provide comparable accuracy. Additionally, single-sideband mixing prevents the occurrence of a second sideband at the inverted Doppler frequency, which would cause additional spectral components and impede unambiguous velocity estimation as well as impair subsequent processing. The additional gain of 3 dB is advantageous, although not imperative. There are no additional hardware requirements for the radar, but the radar configuration can be optimized for high accuracy. From the CRLB derivations in Ch. 4.1.1 and 4.1.2, influence factors for improved estimation accuracy can be derived. Their investigation

mainly suggests minimum required values for bandwidth and SINR, while the minimum frequency is less relevant due to small relative changes. Substantial changes are not investigated as this would require different hardware in other frequency bands, which are restricted to certain applications. The number of samples contributing to an estimation is considered as linked to the SINR over the corresponding processing gain.

Range Resolution Degradation

From (4.10), the estimation accuracy obtained is presumed to be independent of the sampled bandwidth and, thus, the range resolution. Lower bandwidths ease hardware realization and restrictions while being more spectrally efficient, hence optimization in this regard is aspired. Artificially reduced bandwidths allow for an investigation of bandwidth dependencies disregarding simultaneous effects. In CS, but also in FMCW, the bandwidth used for a measurement can, in retrospect, be artificially reduced by utilizing a contiguous fraction of stored samples. Keeping the original sampling rate, the bandwidth and chirp duration are reduced accordingly, leading to a corresponding degradation in the range resolution as

$$\Delta R' = \frac{1}{u} \cdot \Delta R, \tag{4.39}$$

where u denotes the reduction factor, $u < 1$, by which the used number of samples is decreased as $N_\mathrm{s}' = u \cdot N_\mathrm{s}$.
This artificial resolution degradation is applied to the measurements presented in Fig. 4.16 as these contain the least disturbances. The bandwidth is gradually reduced, giving results as shown in Fig 4.28a. Bisecting the bandwidth ($u = 0.5$, $B = 1.9\,\mathrm{GHz}$) has hardly any effect and $f\varphi$ analysis provides clear advantage of around $300\,\mu\mathrm{m}$ over frequency analysis. A further bandwidth reduction significantly increases the range errors for frequency and $f\varphi$ analysis with the errors increasing strictly monotonically. The accuracy is limited by the frequency analysis that cannot provide an adequate basis for phase-offset analysis. As the bin determination is biased, the error of $f\varphi$ analysis occasionally even exceeds that of frequency analysis and additional phase-offset evaluation is not beneficial anymore. The slight increase in range error for bisected bandwidths is also caused by a deteriorated frequency-based range estimate, which is used not only for the choice of the correct range bin, but also to correct phase terms, so deterioration in range error occurs even while the correct bin is selected.

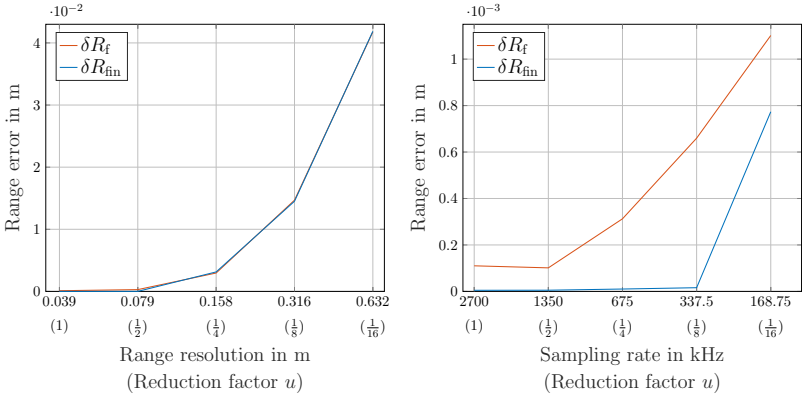

Figure 4.28: Range error over artificially increased range resolution with constant sampling rate (B, T, N_s, SINR decreased, f_s constant) (a) and artificially reduced sampling rate with constant range resolution (N_s, SINR, f_s decreased, B, T constant) (b) for frequency and $f\varphi$ analysis. The x-axis is logarithmically scaled and the reduction factor for each tick label is parenthesized below.

With the applied resolution degradation, the number of samples and, consequently, the SNR are reduced, affecting the accuracy of range estimation for frequency- and $f\varphi$ analysis according to (4.8) and (4.10). To separate this effect from the previously investigated bandwidth reduction, the same sample and SNR reduction is artificially emulated while keeping the bandwidth constant. A reduced number of samples covering the complete bandwidth is used, mimicking a reduced sampling rate f_s. This additionally affects the maximum unambiguous range, which is not sufficient for all reductions, however, the relative manner of measurements preserves processing possibilities. The results in Fig. 4.28b indicate that the reduced accuracy is caused by insufficient bandwidth and does not originate from a decreased number of samples. While the range error for frequency analysis increases continuously, that of $f\varphi$ analysis is hardly affected up to a reduction factor of $u = \frac{1}{8}$ and remains permanently below the error for frequency analysis. However, overly reducing the measurement samples also limits the accuracy of range estimation as the available information is insufficient.
This reinforces the strong importance of adequate frequency analysis as a basis

for $f\varphi$ range estimation and its dependency on the bandwidth, although the CRLB for $f\varphi$ analysis is bandwidth-independent. Despite the indirect correlation, the limitations of frequency analysis must therefore be taken into account during parameterization of a radar sensor for high-accuracy range estimation, but requirements are moderate.

Velocity Resolution Degradation

Not only the range resolution, but also the velocity resolution affects the reached accuracy as the Doppler estimation depends on it and is used for Doppler correction. In CS, the velocity resolution can, in retrospect, be artificially degraded by utilizing only part of the captured chirps, resulting in

$$\Delta v' = \frac{1}{u} \cdot \Delta v, \tag{4.40}$$

where u denotes the reduction factor, $u < 1$, by which the used number of chirps is decreased as $N_\mathrm{c}' = u \cdot N_\mathrm{c}$. Integer divisors of $N_\mathrm{c} = 255$ are used for u.
The velocity resolution degradation is applied to the measurements with $v_\mathrm{set} = 1\,\mathrm{m/s}$ from Fig. 4.20. It primary affects the FFT-based velocity estimate, to an extent that zero Doppler is estimated and the velocity error equals the nominal velocity as exemplified in Fig. 4.29a. The CZT-based estimate consequently also deteriorates, but to a lesser extent. Attributing this effect to velocity resolution degradation is not as straightforward as it is with range estimation. The accuracy of velocity estimation also depends on the number of chirps and the SNR according to (4.25). In order to reduce N_c comparably at constant velocity resolution, the chirp repetition time T_cr must be increased accordingly. However, this reduces the maximum unambiguous velocity and, unlike in range estimation, this effect must be compensated for in signal processing, as the reference is absolute and not relative. This was not achieved with the same accuracy as the other estimates as visible in Fig. 4.29b. Additionally, the FFT-based velocity estimate does not develop monotonously with increasing chirp repetition rate. In the numeric values, the velocity error for constant resolution is unchanged up to a reduction factor of $u = \frac{1}{5}$, where the estimation is unambiguous. For increasing resolution, it is increasing slowly but continuously. Therefore, poorer resolution is associated with a higher velocity error, whereat yet unambiguity has to be assumed.

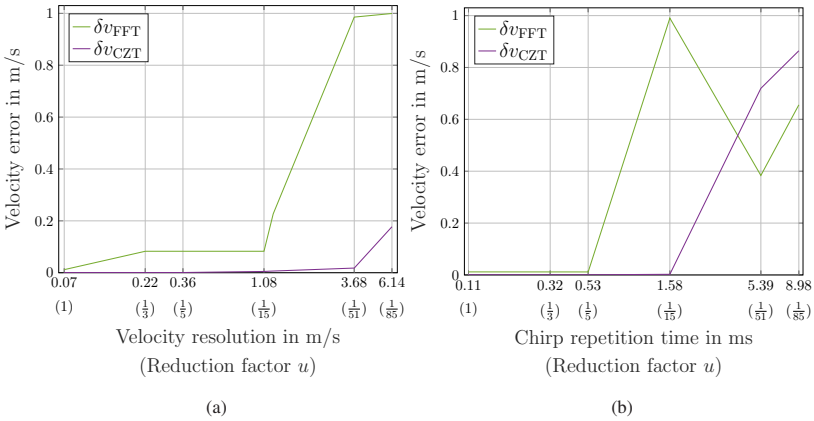

Figure 4.29: Velocity error over artificially increased velocity resolution with constant chirp repetition time (N_{c}, SINR decreased, T_{cr} constant) (a) and artificially increased chirp repetition time with constant velocity resolution (N_{c}, SINR decreased, T_{cr} increased) (b) for FFT-based (v_{FFT}) and CZT-based velocity estimation (v_{CZT}) at 1 m/s. The x-axis is logarithmically scaled and the reduction factor for each tick label is parenthesized below.

Velocity estimation influences range estimation as it is used for Doppler correction. The larger the velocity, the greater the impact, as uncorrected phase terms increase. R_{f} is much more sensitive to increasing velocity errors as the evaluated terms are directly affected whereas the phase offset only experiences an indirect influence from suboptimal correction. For a small velocity of 1 m/s (Fig. 4.30a), $f\varphi$ estimation hence hardly deteriorates over increased velocity resolution, although the curve progression of v_{CZT} is reflected in R_{fin}. For larger velocities, frequency analysis cannot provide a sufficient basis for phase-offset evaluation, and an erroneous bin choice significantly deteriorates R_{fin}. That being the case, $f\varphi$ analysis is no longer superior to frequency analysis as observable in Fig. 4.30b for the measurements with $v_{\mathrm{set}} = 3\,\mathrm{m/s}$ from Fig. 4.20. Nevertheless, range estimation never becomes entirely independent of Doppler estimation, even at very low target velocities. The apparent stability of R_{fin} shown in Fig. 4.30a is partly due to the reduced number of chirps employed to degrade the resolution; consequently, fewer chirps are summed. If no Doppler correction is applied during processing yet the chirps are still summed despite the clear violation of the static target assumption, the resulting range error

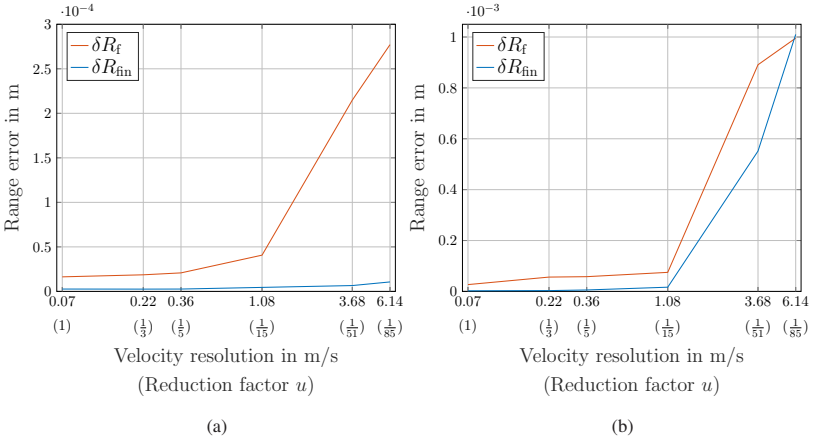

Figure 4.30: Range error over artificially increased velocity resolution (N_c, SINR decreased, T_{cr} constant) for a target moving with 1 m/s (a) and 3 m/s (b). The x-axis is logarithmically scaled and the reduction factor for each tick label is parenthesized below.

drastically increases. As the target moves while the chirps are acquired, each chirp contains information about the target at a slightly different range. Without accurate Doppler estimation and correction, summing these chirps results in a corrupted range estimate not suitable to determine the correct range bin of the target at its initial position. Omitting the summation in case no or insufficient Doppler correction was applied mitigates the impact on range estimation. The same consideration applies for long chirp durations such as those used in FMCW radars, which would require additional correction. For CS, however, the range is assumed to be constant within a single chirp as velocities and chirp durations are limited.

Consequently, the applied processing has to be chosen depending on the required accuracies, available radar parameters, and possible Doppler shifts in awareness of the targeted application. Three exemplary cases are visualized in Fig. 4.31, depicting the requirements for range estimation in case of a small target velocity and medium and high required accuracy. For small velocities and if the available SINR is sufficient to renounce the processing gain of the chirp summation and the additional target suppression, Doppler correction can be omitted. If, on the other hand, only medium accuracies are targeted, frequency-based range

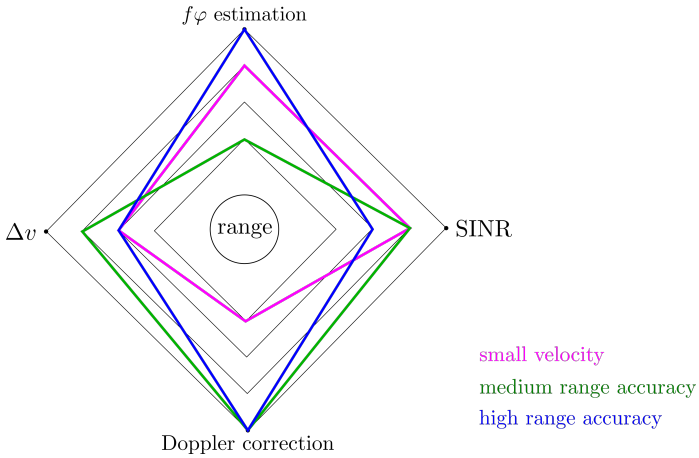

Figure 4.31: Requirement analysis for range estimation with regard to processing ($f\varphi$ or frequency-based), required SINR, required Doppler correction, and required Δv. Three cases, small velocities, medium required accuracy, and high required accuracy, are compared.

estimation may be sufficient but requires reliable Doppler correction with relatively fine velocity resolution. Otherwise, and particularly if high accuracies are to be achieved for targets moving at higher velocities, Doppler-aware $f\varphi$ range estimation is predestined. Under those conditions, no particularly fine velocity resolution or high SINR are required as the processing is robust in different scenarios.

The combined $f\varphi$ range estimation was transferred to CS, including dynamic scenarios, and the accuracy was demonstrated in terms of small range errors, indicating high trueness, and low variance, hence high precision. Average absolute range errors over the investigated stage positions of 4.8 and 2.3 µm for a static and a dynamic scenario with 1 m/s are achieved, comprising a signal-processing-induced enhancement for range estimation to moving targets. These are outstanding results for free-space measurements with commercial hardware and medium bandwidths. The dependency of the reached accuracy on factors such as processing, bandwidth, or SNR, was discussed by means of supportive investigations. The proposed processing outperforms range estimation using

only frequency-based analysis and additionally delivers a reliable velocity estimate with velocity errors of 1.4 mm/s at 1 m/s. Estimating best achievable values beyond theoretical bounds is ambiguous as it depends on a variety of factors, including the radar hardware, reference systems, and measurement setups, which can be optimized for either maximum accuracy or realistic application. The latter is focused on in this work, nonetheless, excellent estimation performance is achieved particularly in range.

5 Radar Target Identification with Doppler Tags

The highly accurate range estimation discussed in Ch. 4 is particularly valuable if the object, whose range is estimated, can be explicitly identified. Radar tags enable the separation of objects of interest while distinguishing them from the environment. This is of paramount interest for the simultaneous usage of multiple objects and, thus, tags. The work at hand initially introduces the Doppler tag, a novel radar tag designed for unique identification and highly accurate range estimation, originally published in [2]. It provides a comprehensive overview of the radar environment, containing multiple identified markers and general sensing information about the remaining untagged surroundings. An overview of the current state of the art regarding radar tags and hardware approaches similar to the Doppler tag is given in Ch. 1.2.
To evaluate the achievable performance of Doppler tags, hardware implementations with commercial components are realized. These are not tailored to the operation as tag and do hence introduce additional challenges preventable with hardware conceptualized specifically as Doppler tag. However, the demonstrator setups allow for the verification and optimization of system design prior to realization. Two different hardware concepts are utilized hereinafter to investigate different aspects of the Doppler tag concept. They both implement the basic idea of a Doppler tag and share a similar setup, although the adaption possibilities differ and make them suitable for investigations with distinct focus.

The basic idea of the Doppler tag is presented for the first time, together with a system design draft that can be used as the basis of a tailored hardware implementation. The latter is yet not within the scope of this work. The hardware used for subsequent investigations is presented with a discussion of benefits and limitations, each.

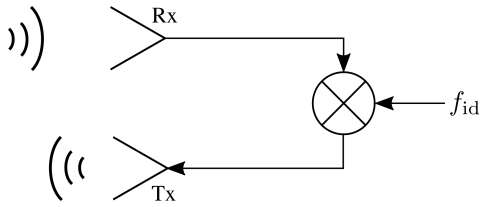

Figure 5.1: Block diagram of a Doppler tag using double-sideband mixing.

5.1 Doppler Tag Principles

Doppler tags mimic the Doppler effect and use an artificially raised frequency shift characteristic for each tag. This shift is assigned to an object or a functionality, which allows for tag separation and enhanced applications. Subsequent processing is based on the handling of the artificial Doppler phenomenon. Doppler tags enable unique identification without suppressing environmental reflections, hence preserving the detectability of the untagged surroundings. They can thus provide an overview of the radar environment with identified markers and general sensing information at short to medium ranges. A key advantage of Doppler tags is their ability to pinpoint the range between radar and tag through dedicated signal processing. This is ensured by shift correction without affecting the object-specific signal shares. The tags utilize the processing chain introduced in Ch. 4 and a tailored hardware principle. The artificial Doppler shift enhances the estimation accuracy in the same way as a motion-induced Doppler does. It separates targets and effectively suppresses static clutter, therefore improving the SINR. In contrast to most other radar tags, modification of the radar hardware is not necessary to allow for operation together with Doppler tags, however, signal processing is adjusted to allow for information extracting from the tags.

In CS radar, a Doppler shift can be implemented as a shift in frequency, which the tag applies with a double-sideband mixer. In the most basic setup (Fig. 5.1), the radar signal is received at the tag, mixed with a certain identification frequency f_{id}, and transmitted back toward the radar. As the identification frequency emulates a Doppler shift, resolution and unambiguity are equivalent to motion-induced Doppler estimation: $\Delta f_{\mathrm{id}} = \Delta f_{\mathrm{D}}$ and $f_{\mathrm{id_{ua}}} = f_{\mathrm{D_{ua}}}$.
Doppler tags are not restricted to operation with CS radars, however, those are

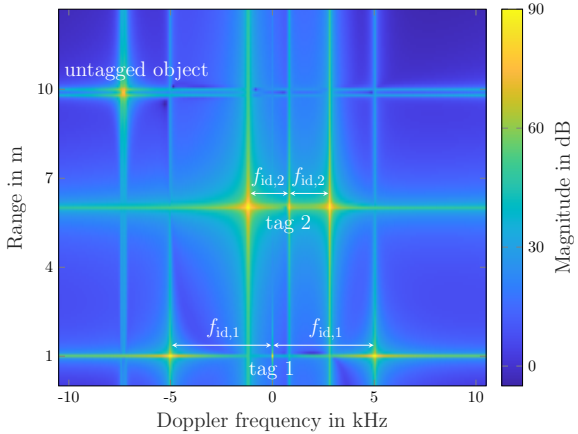

Figure 5.2: Simulated RDM for three objects. The two objects at 1 and 6 m are tagged with $f_{\mathrm{id},1} = 5\,\mathrm{kHz}$ and $f_{\mathrm{id},2} = 2\,\mathrm{kHz}$, respectively. While the first one is static, the second one moves with 2 m/s ($f_{\mathrm{D},2} \approx 800\,\mathrm{Hz}$) away from the radar. The third object does not carry a Doppler tag but moves with 18 m/s ($f_{\mathrm{D},3} \approx 7\,\mathrm{kHz}$) toward the radar, starting at 10 m.

the quasi-standard in industrial radar applications. As a well-investigated and commercially available sensor option, they are already applied in industrial automation and a combination with Doppler tags further expands their functional spectrum. Nevertheless, in other contexts it can be favorable to operate Doppler tags with other radar waveforms such as orthogonal frequency-division multiplexing (OFDM). Tag design would not significantly differ and comparable performance is expected, although signal processing would require modification. This work focuses on Doppler tag operation with CS radars.

Implementing the idea of Doppler tags in simulations, a range-Doppler map (RDM) as shown in Fig. 5.2 is obtained. Two Doppler tags with $f_{\mathrm{id},1} = 5\,\mathrm{kHz}$ and $f_{\mathrm{id},2} = 2\,\mathrm{kHz}$ as well as an untagged object moving with $v = 18\,\mathrm{m/s}$ toward the radar, are simulated. Tagged objects are detected thrice, once at their real velocity, as the radar signal is reflected off the object itself without passing through the tag, and twice with their characteristic artificial Doppler shift. This Doppler originates two symmetric peaks at $f_{\mathrm{D}} \pm f_{\mathrm{id}}$ due to double-sideband mixing as visualized in Fig. 5.2 for a static (tag 1) and a moving tag (tag 2). Using an active amplification within the tag, the amplitude of the tag response

is significantly above that of the object reflection, in case of static targets additionally masked by static clutter, so that only the symmetric peak pair is used in further processing. Untagged objects are detected as normal. Tag identification is not disturbed by untagged objects as they are mostly static and, if not, unlikely to have the exact same Doppler shift as applied by a tag. Tags can even be distinguished from objects with velocities equal to the artificial Doppler since these objects will indeed change their ranges over time. In contrast, the two peaks occurring at $f_\mathrm{D} \pm f_\mathrm{id}$ due to double-sideband mixing mostly have differently signed Doppler so that objects with these velocities would move in different directions while the tag and its peak pair are static or at most move in one direction with a way smaller velocity than that of the objects. Masking is only possible while range and velocity bins are very similar or even equal, which is rarely the case in real scenarios and only a short-time implication, as the required motion of the untagged object resolves the ambiguity.

For the untagged object in Fig. 5.2, migration over multiple range bins due to the high velocity as discussed in (2.7) is apparent. To emulate a Doppler shift within the tag, a phase shift of $2\pi f_\mathrm{id}(t+mT)$ is applied through mixing, but no change in range occurs as no real movement is simulated. Thus, no migration terms arise and the tag peaks are clearly delineated. In the beat phase of a single sideband (5.1), tmT-dependent terms are hence missing:

$$\begin{aligned}\Phi_{\mathrm{b,DT}}(t,m) =& 2\pi\left(\left(\frac{B}{T}\tau_0 + f_\mathrm{id}\right)t + f_\mathrm{id}mT\right.\\ &\left. + \tau_0\left(f_\mathrm{min} - \frac{f_\mathrm{id}}{2} - \frac{B}{2T}\tau_0\right)\right) + \varphi_\mathrm{id}\end{aligned} \tag{5.1}$$

The coupling term $f_\mathrm{id}t$ is still existent and can cause the sideband peaks to drift in opposite range directions for large identification frequencies as discernible for 25 kHz in Fig. 5.3b and 110 kHz in Fig. 5.3c. Thereupon and with increasing coupling, tag peaks are more difficult to relate to each other and to distinguish from untagged objects, impeding tag elimination and subsequent range estimation. The usable identification frequencies are hence limited depending on the system design, whereat, however, the effect only occurs beyond the maximum unambiguous velocity. Nevertheless, if correct peak assignment and tag elimination is possible in a sparse environment or from preknowledge, coupling is equalized during elimination and subsequent processing is not impaired. The artificial Doppler is henceforth chosen in the same order of magnitude as a

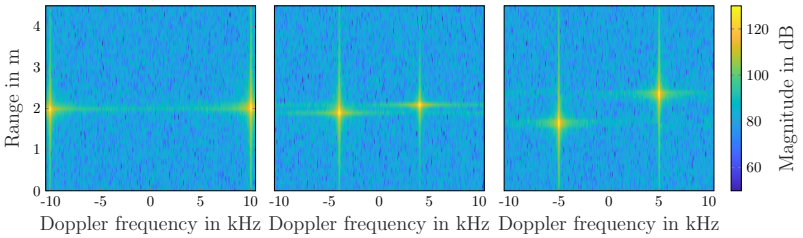

Figure 5.3: Simulated RDM containing a single Doppler tag, tagged with 10 kHz (a), 25 kHz (b), and 110 kHz (c). For 10 kHz, both sideband peaks are at the same range while for 25 kHz, coupling makes them drift in opposite range directions, even better perceptible for 110 kHz where the coupling is correspondingly stronger.

motion-caused Doppler shift. Doppler estimation is possible from the $f_{\mathrm{id}} mT$ term without impacting coupling effects. Even in case of large ranges and consequently, large delays τ_0, Doppler tag operation hence remains reliable. However, for large velocities, the peak pair migrates over multiple consecutive range bins with its range determined by the motion and migrating with the direct object reflection. This migration is not caused by the tag but an inherent radar phenomenon with the number of migration bins

$$N_{\mathrm{mig}}(v) = \frac{R_{\mathrm{mig}}}{\Delta R} = \frac{2BN_{\mathrm{c}}T_{\mathrm{cr}}}{c} \cdot v. \tag{5.2}$$

Using double-sideband mixing, two mixing products emerge, and the final beat signal can mathematically be described as the sum of those, thus

$$\begin{aligned} s_{\mathrm{b,DT}}(t,m) = \exp\Bigg(\mathrm{j}\Phi_{\mathrm{b}}(t,m) + \mathrm{j}\left(2\pi f_{\mathrm{id}}\left(t - \frac{\tau_0}{2} + mT\right) + \varphi_{\mathrm{id}}\right)\Bigg) \\ + \exp\Bigg(\mathrm{j}\Phi_{\mathrm{b}}(t,m) - \mathrm{j}\left(2\pi f_{\mathrm{id}}\left(t - \frac{\tau_0}{2} + mT\right) + \varphi_{\mathrm{id}}\right)\Bigg). \end{aligned} \tag{5.3}$$

In (5.3), not only a frequency shift is applied but an additional, unknown phase shift φ_{id} originating from the random phase position of the mixing signal. Equation (5.3) together with (2.7) describes the complete signal model for a CS signal received and retransmitted by a Doppler tag with double-sideband mixing.

Processing of a signal containing a Doppler tag is based on the RDM achieved after a two-dimensional (2D) FFT. As the shift in frequency is small relative to the center frequency of the radar, the tag response is received at the radar together with and in the same way as the reflections of untagged objects in the radar field of view (FoV). It can be easily integrated into the standard radar signal processing coming from (5.3). The radar processing including a Doppler tag from identification to range and velocity estimation is shown in Fig. 5.4 and discussed hereinafter. It can be carried out in parallel to normal sensing of the environment so that tagged and untagged objects are both served. Signal processing is performed in two steps: first, identifying the target by means of f_{id}, and second, determining the initial target range R_0 and velocity v. Identification is achieved solely through signal processing, similar to motion-induced Doppler determination. f_{id} is obtained from a 2D FFT on the radar signal and a subsequent maximum search or constant false alarm rate detection on the resulting RDM as shown in the upper part of Fig. 5.4. For a single tagged object, two maxima are detected at $f_{\mathrm{D}} \pm f_{\mathrm{id}}$. The objects in question are assumed to be preknown, such as from a table that assigns an $f_{\mathrm{id,x}}$ to each tagged object, allowing for unambiguous identification. To enhance the determination of f_{id}, zero padding is applied.

5.1.1 Novel Signal Processing Approach for Unimpaired Range Estimation

An innovative signal processing approach is developed to allow for unimpaired range estimation despite Doppler tag operation. For both range and velocity estimation, elimination of the Doppler tag influence is crucial. The proposed processing enables reliable Doppler tag elimination independent of the achieved identification accuracy. The precious phase-offset information remains unimpaired and available for highly accurate range estimation. The idea is a mathematical artifice separating and recombining the two sidebands emerging after double-sideband mixing. 2D windowing is applied around each sideband, concomitantly separating this tag from other targets and the two sidebands of this tag from each other. The two resulting signals are retransformed to the time domain using a 2D inverse fast Fourier transform (IFFT). Each of these signals only carries the information of one sideband, hence the contained tag modifi-

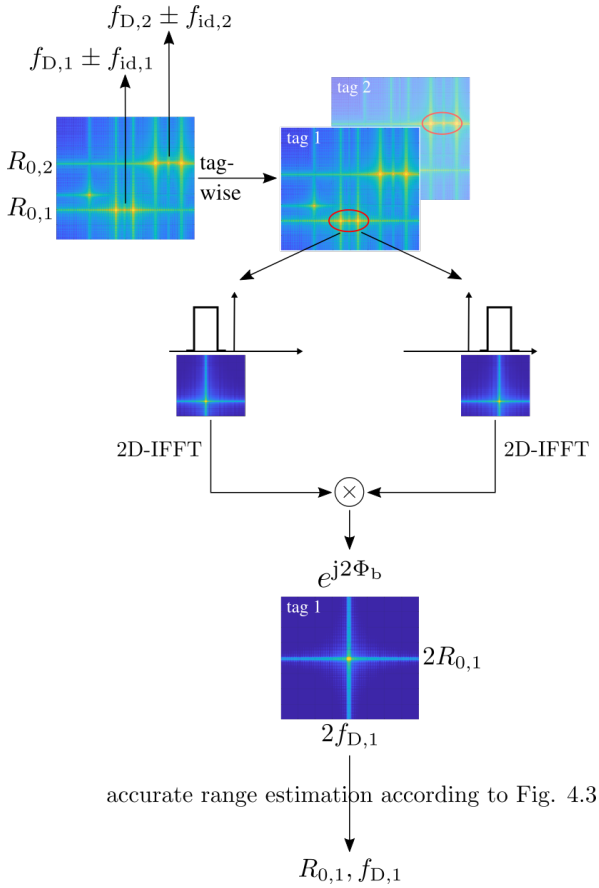

Figure 5.4: Processing chain for Doppler tag identification and elimination for subsequent range and velocity estimation. The occurring tag frequencies $f_{\mathrm{id},x}$ are determined from an RDM, and the remaining processing is performed tag-wise. Windowing simultaneously separates one tag from the other targets and the two sidebands of this tag from each other. The two windowed signals are multiplied in the time domain to eliminate the influence of the Doppler tag in frequency and phase. The resulting signal contains only information about one tagged object and therefore allows for conventional processing. However, the phase is doubled due to the preceding multiplication, which consequently results in a doubling of the range and velocity estimates and must be accounted for in further processing.

cation differs in sign. By means of a complex multiplication, the impact of the considered tag vanishes, resulting in

$$\begin{aligned} s_{\mathrm{b,w/o\,DT}}(t,m) &= \exp\left(\mathrm{j}\Phi_{\mathrm{b}}(t,m) + \mathrm{j}\left(2\pi f_{\mathrm{id}}\left(t - \frac{\tau_0}{2} + mT\right) + \varphi_{\mathrm{id}}\right)\right) \\ &\quad \cdot \exp\left(\mathrm{j}\Phi_{\mathrm{b}}(t,m) - \mathrm{j}\left(2\pi f_{\mathrm{id}}\left(t - \frac{\tau_0}{2} + mT\right) + \varphi_{\mathrm{id}}\right)\right) \\ &= \exp\left(\mathrm{j}2\Phi_{\mathrm{b}}\right). \end{aligned} \tag{5.4}$$

The resulting RDM is shown in the lower part of Fig. 5.4. The doubling in phase, transferring to range and velocity, is a side effect of the multiplication as shown in (5.4) and is corrected during estimation. In the phase itself, not only the artificial frequency shift f_{id} but also the unknown phase shift φ_{id} are canceled out so that the phase offset of the radar signal φ_{b} is not corrupted. This is even the case if the artificial frequency shift is not exactly known. Consider a deviation in the applied f_{id}, $f_{\mathrm{id}} + \delta$, e.g., due to a frequency drift. Identification is not impaired as long as the resulting frequency shift can still be assigned to the original f_{id}, hence no particularly high accuracy is required in the estimation of the identification frequency. Equation (5.3) will change accordingly, but nonetheless, the same frequency shift $f_{\mathrm{id}} + \delta$ occurs in both sidebands and can be eliminated equivalent to (5.4). Subsequent range and velocity estimation are thus not affected. This is also evident from the fact that the knowledge of possible $f_{\mathrm{id},x}$ is used only for identification, not for any subsequent processing. Similar considerations apply to phase noise and other non-ideal phenomena disturbing the identification frequency. Additionally, other tags and untagged measurement surroundings are suppressed during tag elimination in a similar way the Doppler correction in Ch. 4.1 achieves it.

After tag elimination, range and velocity estimation is performed for the corresponding object as discussed in Ch. 4 and Fig. 4.3. The only necessary adjustment is the consideration of a factor two. Motion-induced Doppler shifts are determined and corrected as well. Doppler shifts that may remain after tag elimination are corrected as if they were motion-caused. The resulting error is negligible as the remaining tag-caused Doppler shifts are minute and so are the unnecessarily corrected migration terms. The Doppler correction together with the cancellation of the unknown mixing phase shift φ_{id} allows for a reliable evaluation of the phase offset for range estimation according to (4.4).

5.1.2 CRLB including Doppler Tags

To contextualize this estimation, again the CRLB is used. Doppler tags emulate a Doppler shift without corresponding motion, hence the signal model differs from that in a dynamic scenario and so do the CRLBs. A derivation of the CRLB for parameter estimation in a static scenario including a single Doppler tag is given in A.1.4. The extension to multiple Doppler tags or dynamic scenarios is not included as the CRLBs are used for structural considerations rather than for actual performance comparison. However, derivations follow the same procedure as in A.1.2 and A.1.3. For range estimation, the CRLBs are derived to

$$\mathrm{var}(R_\mathrm{f}) \gtrapprox \frac{3c^2}{8\pi^2 B^2 \eta N_\mathrm{c} N_\mathrm{s}} \tag{5.5}$$

and

$$\mathrm{var}(R_\varphi) \gtrapprox \frac{7c^2}{2(4\pi)^2 f_\mathrm{min}^2 \eta N_\mathrm{c} N_\mathrm{s}}. \tag{5.6}$$

While the bounds for the range estimates differ from previously derived versions only by constant factors, the identification frequency is bounded by a structurally different term only depending on η, N_c, and N_s. It is estimated directly and transformation of parameters only comprises the sampling rate with $\tilde{f}_{\mathrm{b},3} = \frac{f_\mathrm{id}}{f_\mathrm{s}}$, which prevents f_min dependency in

$$\mathrm{var}(\widehat{f_\mathrm{id}}) \gtrapprox \frac{3f_\mathrm{s}^2}{2\pi^2 \eta N_\mathrm{c} N_\mathrm{s} (N_\mathrm{c}+1)(N_\mathrm{c}-1)}. \tag{5.7}$$

The CRLB for the motion-induced Doppler shift in a dynamic scenario, however, has the same structure and deriving an identification velocity from f_id as done in the addendum, the similarity of these terms is also obvious. This underscores the similarity between motion-induced and artificial Doppler shifts and is a clear indication that similar behavior and characteristics can also be assumed in other respects.

5.1.3 Considerations for Multiple Doppler Tags

For multiple tags in the radar FoV, multiple peak pairs occur in the RDM. Separation and identification is possible from their symmetry, and untagged

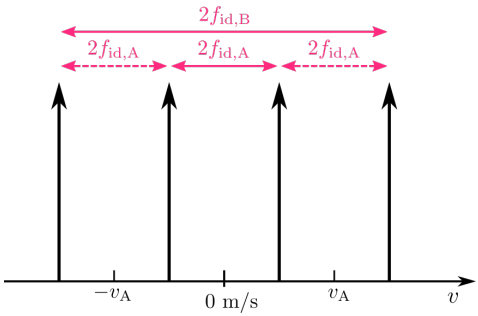

Figure 5.5: Schematic representation of arising ambiguity for multiple, potentially moving Doppler tags with identification frequencies being multiples of each other ($f_{\mathrm{id,B}} = 3 \cdot f_{\mathrm{id,A}}$).

objects, causing unmated peaks, can be differentiated. Correctly associating maxima belonging to the same peak pair presents the major challenge in signal processing. Peaks from moving objects or multiple reflections as well as strong sidelobes have to be excluded while pairs not perfectly symmetric, e.g., due to noise or nonlinearities, must not be missed. To achieve this, the unique characteristics of peak pairs are exploited. As both peaks in a pair originate from the same object, they are located at the same range and have similar amplitudes. Additionally, tag-caused peaks contain a Doppler shift with the frequency symmetry depending on object motion. Moving tags may overlap awhile, however, this ambiguity is before long resolved by the motion-induced change in range. System design has to ensure that identification frequency and motion-induced Doppler shift do not coincide as this would cause a tag peak at zero Doppler and not separable from static targets. If tags are used whose identification frequencies are multiples of each other, ambiguities can arise from motion as delineated in Fig. 5.5. Considering two identification frequencies $f_{\mathrm{id,A}}$ and $f_{\mathrm{id,B}}$ with $f_{\mathrm{id,B}} = 3 \cdot f_{\mathrm{id,A}}$, tag A can be detected either as static or with $\pm v_{\mathrm{A}}$, which is to be prevented during system design or resolved through signal processing.

A significantly larger number of peaks than the expected two per tag are initially detected. The peaks of interest are thus reliably included. Peaks at the same range are considered potential pairs, and only those with a frequency spacing close to twice a potential identification frequency are processed further. Among these, the most symmetric pairs are selected, and the final pair is chosen based on the highest amplitude.

All subsequent processing steps are completed on one distinct RDM for each evaluated tag as also indicated in Fig. 5.4. Consequently, ranging to a large set of tags can impose significant overhead as the processing effort scales with the number of tags. In typical applications such as tool identification or self-positioning, multiple tags are employed concurrently, yet are not all in the FoV of the radar at once, thereby mitigating scaling limitations.

As the tags are separated by their artificial Doppler frequency f_{id}, the number of simultaneously usable tags is limited by the frequency resolution Δf_{D} and maximum unambiguous frequency $f_{\mathrm{D_{ua}}}$ of the radar. In theory, each Doppler bin pair could be occupied with one tag, allowing a number of tags equal to half the number of chirps per measurement. Nonetheless, some margin should be allowed to prevent false identification as soon as the Doppler determination is off by one bin or the tagged object is in motion additionally, causing Doppler migration. In measurements, a frequency spacing of at least twice the frequency resolution was found to be required in static scenarios, although slight deterioration is observed already for larger spacings. Generally, the available number of tags is dependent on the number of chirps per measurement, the size of the margin that is granted between two tags, the potential velocities of the tagged objects, and the realization of the mixing process.

Single-sideband mixing provides more available tag frequencies as $\pm f_{\mathrm{id}}$ could be used to tag two objects. However, due to the random phase position of the mixing signal relative to the radar signal, mixing always applies an unknown phase shift to the signal in addition to the intended frequency shift, which is irrelevant for identification but influences the possibilities for high-accuracy range estimation. Using a double-sideband mixer, both sidebands are included in the signal, and the phase shift can be canceled, although unknown. In single-sideband mixing, the phase shift cannot be eliminated and only the less accurate frequency-based range estimation is applicable. Additionally, if the tagged object is in motion, symmetric guard intervals of velocity-dependent width around the artificial Doppler are necessary to prevent erroneous identification. A real Doppler shift adds or subtracts from the artificial one, depending on the relative direction of motion. This displacement within the Doppler domain has to happen within a distinct interval where all frequencies belong to one object; otherwise the real Doppler will falsify the object identification. This can be challenging if the expectable velocities are unknown and additionally limits the available number of tags. Guard intervals are not required for double-sideband

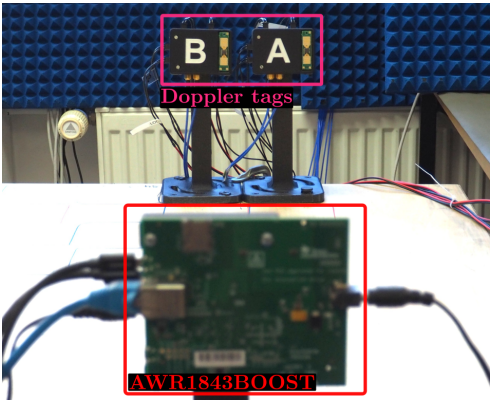

Figure 5.6: Measurement setup with radar centered between two tags A and B, resulting in equal distances from the radar to each tag.

mixing as the identification frequency is determined by the frequency difference between the two sidebands. A real Doppler shift changes the position of both sidebands in the frequency domain; their position relative to each other, and hence the determined f_{id}, remain. A corrupted identification of moving untagged objects as tagged ones or a confusion of Doppler tags is hence unlikely and can be prevented by scenario-aware choices of $f_{\mathrm{id},x}$.

Tag-induced Resolution Enhancement

While frequency spacing is a design parameter for radar-tag systems, spacing in range is not required for object separation. Using Doppler tags, the identification resolution is equal to the frequency spacing and enhances range resolution indirectly. This is of interest as the processing approach discussed in Ch. 4 only enhances the estimation accuracy, for which medium bandwidths are sufficient. Those, in turn, limit the available range resolution, but in multi-object environments, the resolution of a system is of particular significance and often even prioritized over accuracy.

The resolution enhancement is demonstrated with the setup in Fig. 5.6. The radar sensor is centered between the two used tags so that they are at the same range from the radar. Without activated tags, it is not possible to distinguish the tag

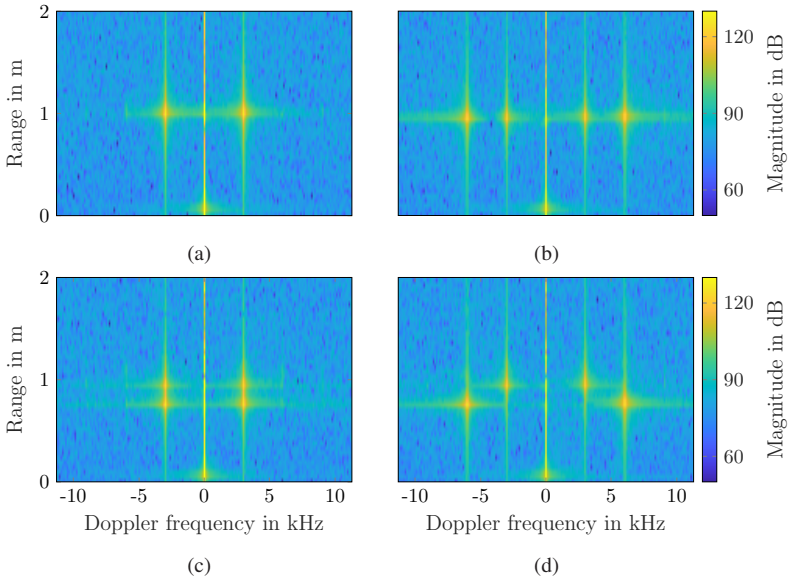

Figure 5.7: RDM for measurements in the setup in Fig. 5.6 with $f_{\mathrm{id,A}} = f_{\mathrm{id,B}} = 3\,\mathrm{kHz}$ ((a), (c)) and $f_{\mathrm{id,A}} = 3\,\mathrm{kHz}$, $f_{\mathrm{id,B}} = 6\,\mathrm{kHz}$ ((b), (d)). If different identification frequencies are applied, tag separation is possible despite a range difference below the range resolution.

hardware from the static environment. If both tags are turned on, but using the same identification frequency, the tags are clearly visible, but at the very same point in the RDM (Fig. 5.7a), so that differentiation is not possible and the tags cannot be identified and processed separately. Increasing the range difference above the range resolution by moving tag B closer to the radar, a separation of tags in range is possible (Fig. 5.7c). However, when choosing different f_{id} for the two tags, they are easily distinguished in the Doppler domain, disregarding a range difference (Fig. 5.7b and 5.7d), and avoiding the need for particularly high range resolution.

For moving targets, the velocity resolution can as well be enhanced using Doppler tags as they spread targets with the same or similar Doppler by the additive f_{id}, enabling separation and identification despite insufficient range and velocity resolution. Multi-object and crowded environments hence benefit most

from the usage of tags. However, the resolution of untagged objects remains unchanged and depends only on the radar bandwidth for range resolution and measurement time for velocity resolution. This has to be considered as part of the system specification if fine separation of objects, which cannot or should not be tagged, is required.

5.2 System Specification

Doppler tags follow a relatively simple hardware approach that, together with appropriate signal processing, enables the unique identification of targets and a highly accurate estimation of their range while being receptive for the untagged surroundings. This expands the radar scope of application to include target identification while not limiting conventional sensing. To allow for high-accuracy range estimation, which requires unimpaired phase information despite the modulation applied by the tag, both hardware and processing have to be carefully designed and coordinated. Only target identification would set lower demands on the hardware and require significantly less processing. However, the combination of features introduces new prospects in addition to conventional sensing and corresponding functionalities.
Concurrent operation of multiple tags without mutual interference is inherently provided and the processing for each tag simultaneously suppresses other tags and static targets. Tags are read at once without any protocol or time division. The usage of common radar hardware, which is already provided for classical sensing, is of additional advantage as no secondary system is required. The straightforward hardware design allows for compact and cost-efficient fabrication, making large numbers of tags feasible. Although the tag hardware is not very complex and similar setups have been used before for other purposes, no dedicated Doppler tag hardware is available yet. To demonstrate system capabilities and prepare specialized chip design, basic concepts and dependencies as well as performance forecasts are investigated. An early stage system specification provides guidance and identifies areas of research prior to chip design. The specification in this work focuses on a Doppler tag in industrial applications such as supporting autonomous navigation and operation of robots or guided vehicles. Similar applications are also investigated in demonstration setups discussed in Ch. 7.

Basic radar parameters are chosen according to Table 3.3 to reflect requirements in these applications. As major decision, the operational frequency was chosen in an ISM band and as a compromise between available bandwidth for range estimation and path attenuation. Additionally, it provides favorable conditions for tag minimization and promising performance bounds. The range resolution meets the requirements of frequency analysis for a combined estimation and the Doppler resolution ensures accurate identification. However, a poor estimation would hardly affect identification but deteriorate subsequent velocity estimation, impairing, e.g., tracking tasks. The maximum unambiguous Doppler shift restricts not only the real velocities that can be determined, but also the number of concomitantly available Doppler tags. In measurements, a minimum frequency spacing between tags of twice the Doppler resolution has proven necessary for accurate range estimation, whereat larger spacing results in more robust estimation. Conversely, the Doppler resolution also defines the accuracy of identification and velocity estimation, requiring a compromise between identification accuracy and the number of available tag frequencies as well as velocity estimation accuracy and maximal accordable velocities. These choices are highly application specific and do not coincide for the considered industrial applications, hence, even within the subsequent performance and application demonstrations, different radar parameters are used.
Tag parameters are specified according to the radar parameters with the main goal of optimized tag reflectivity and symmetry in double-sideband mixing. The amplification provided by the tag is crucial to ensure good SNR and wide coverage with radar-tag-systems. An active amplification of around 80 dB is favorable to secure constant and reliable operation up to 10 m. For enhanced flexibility and improved power consumption, the amplification is preferably provided by a fixed and a variable gain amplifier in combination. The first amplifier should be a low noise amplifier (LNA) so that tag noise remains secondary. For additional amplifiers, the phase performance is less crucial, but the maximum input power is to be considered as it already contains active amplification and the 1 dB compression point must be designed accordingly to ensure linearity. Strong amplification comes with the risk of oscillations in a feedback loop that could saturate the LNA, hence antenna coupling and mixer RF isolation must be designed in such a way that oscillation is prevented.

Double sideband mixing with a frequency range of around 1 to 25 kHz allows for accurate range estimation with multiple tags of different identification frequencies. Higher frequencies are less favorable as range-Doppler coupling

increases and complicates peak to tag assignment as observed in Fig. 5.3. The 1 dB compression point of the mixer should be chosen well above the input power to provide sufficient dynamic range in different scenarios. Depending on the targeted frequency spacing of tags, local oscillator (LO) frequencies have to be adjustable in small steps. Beyond, there are no specific or exceptional requirements for the oscillator generating the identification frequencies. Harmonics should be minimized as they can interfere with the response from other tags with this identification frequency. Phase noise is to be considered so as not to reduce the SNR and keep the noise contribution of the tag negligible in relevant ranges. Stability over time and temperature are benign and as long as drifts are smaller than half a frequency bin, no performance deterioration will result. In addition, only the less crucial identification accuracy is affected as imperfections in the frequency generation are contained in both sidebands and hence effectively canceled for range and velocity estimation.

The antenna design can provide additional gain for the tag reflectivity, but also has to minimize coupling to prevent oscillations. The choice of opening angles hence requires a compromise. A narrow opening angle enhances the antenna gain and reduces leakage from the transmit into the receive antenna. However, it also impairs visibility of the tag which is of great importance for distributed scenarios. A tailored antenna arrangement, the use of lenses, or polarization are among possible solutions.

These specifications are meant for a tailored Doppler tag design and cannot be found all in one existing device. Dedicated hardware design would be required but should only follow a conceptual investigation and basic performance demonstrations. To be able to investigate all important features of Doppler tags prior to chip design, two hardware implementations are deployed according to their suitability.

5.3 Doppler Tag Implementation

As no specialized Doppler tag hardware is available, two different hardware tags are henceforth used to investigate different aspects of the Doppler tag. They both follow the basic setup of Fig. 5.1, but one is composed of waveguide components, hereinafter referred to as the assembled Doppler tag, while the other one is a commercial miniature radar-target-simulation (mRTS) module,

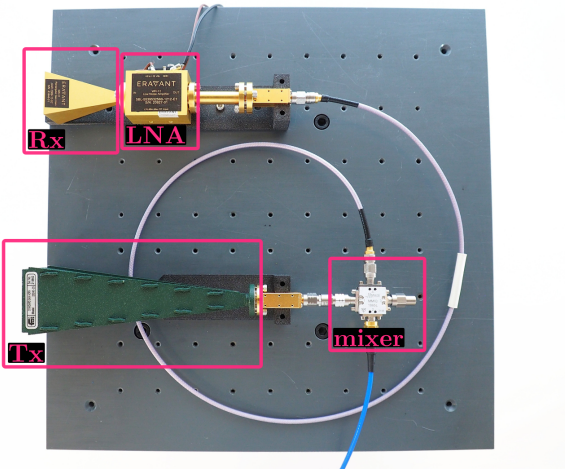

Figure 5.8: Doppler tag setup with Rx antenna (22.5 dBi gain), LNA (6 dB noise figure, 25 dB gain), double-sideband mixer (12 dB conversion loss), and Tx antenna (25 dBi gain).

referred to as mRTS tag. As the tag elimination is a key aspect of the Doppler tag and enables high-accuracy range estimation despite modifications the tag introduced to the signal, both tags use double-sideband mixing. Single-sideband mixing is not investigated due to the inherent drawbacks discussed prior.

Unlike with most other radar tags, modification of the radar hardware is not necessary to allow for operation together with Doppler tags. Nonetheless, the tags operate at different center frequencies, namely 61 and 79 GHz, so that different radar sensors have to be used. This is not a general requirement and hardly affects the achieved results as the frequencies are similar and other aspects such as changing measurement setups dominate. Further, the used radars, IWR6843ISK and AWR1843BOOST, share most specifications, apart from the center frequency.

5.3.1 Assembled Doppler Tag

The assembled Doppler tag is composed of off-the-shelf RF components and depicted in Fig. 5.8. It is designed for operation in the extended E-band at

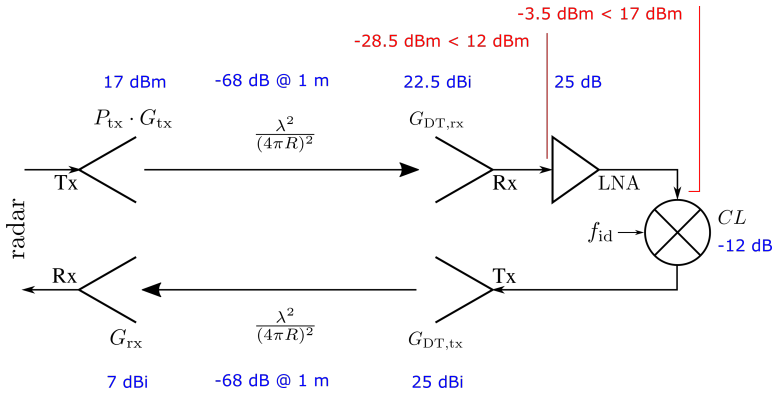

Figure 5.9: Link budget visualization for a radar-Doppler-tag system with gains and losses in blue and comparison against recommended operating conditions in red.

around 61 GHz. The tag consists of the receive and transmit antennas, an LNA with 25 dB amplification, and a single-sideband mixer, of which the I port is terminated to enable double-sideband mixing. The LO port of the mixer is connected to the receive path of the tag, and an artificial Doppler frequency f_{id} is applied at the Q port, allowing the usage and investigation of different $f_{\mathrm{id},x}$, generated by an arbitrary function generator. For measurements of larger ranges above 3 m, an additional power amplifier (PA) with 27 dB amplification can be used to enhance the tag response and extend the maximum detectable range. Further component exchange, such as different antennas or different connection parts from waveguide to coaxial, were found not to influence estimation results and are hence not discussed in detail.

The radar equation is also applicable to an active target such as the Doppler tag as visualized with the link budget in Fig. 5.9. In this case, it is convenient to define an equivalent RCS for the tag ϱ_{DT}. The receive power at the radar is

$$P_{\mathrm{rx}} = \frac{P_{\mathrm{tx}} G_{\mathrm{tx}} G_{\mathrm{DT,rx}} \lambda^2 G_{\mathrm{LNA}}\, CL\, G_{\mathrm{DT,tx}} G_{\mathrm{rx}} \lambda^2}{(4\pi R)^4}, \tag{5.8}$$

hence in consideration of (2.1), the RCS of a Doppler tag is defined as

$$\varrho_{\mathrm{DT}} = G_{\mathrm{DT,rx}} \frac{\lambda^2}{4\pi} G_{\mathrm{LNA}}\, CL\, G_{\mathrm{DT,tx}}. \tag{5.9}$$

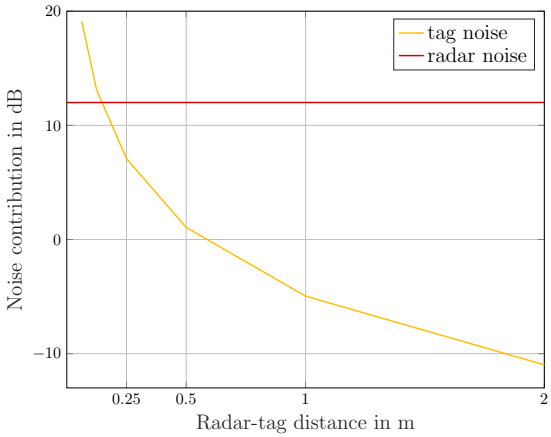

Figure 5.10: Calculated noise contributions of radar and assembled Doppler tag over increasing distance. From to a distance of 20 cm between radar and tag, tag noise is minor and hence neglected hereinafter.

In case of the assembled Doppler tag, $\varrho_{\mathrm{DT}} = 3.5\,\mathrm{dB\,m^2}$ and hence considerably above the untagged surroundings, although dedicated radar targets can have a RCS far beyond that.

The radar sensor used with this tag is an IWR6843ISK (Ch. 3.1.2) with the measurement parameters given in Table 3.3. Its functionality, setting options, and performance are comparable to those of the AWR1843BOOST used for the investigations in Ch. 4. As shown in red in Fig. 5.9, it is ensured that neither the incoming radar signal saturates the tag nor does the tag response saturate the radar. In the Rx chain of the tag, the LNA 1-dB compression point (12 dBm) is not reached with a radar Tx effective isotropic radiated power of 17 dBm and a tag Rx antenna gain of 22.5 dBi. For the mixer LO input, at which the LNA output is connected, the maximum input power should be below 17 dBm for recommended operating conditions, which is not reached with the LNA gain of 25 dB.

For an SNR analysis, the noise contributions of tag and radar are contrasted. Given a receiver noise figure of 12 dB for the IWR6843ISK, the noise contributions are compared in Fig. 5.10 for an increasing distance between radar and tag. Up to around 20 cm, the tag noise exceeds the noise contributed by the radar and must therefore be included in SNR calculations. However, such

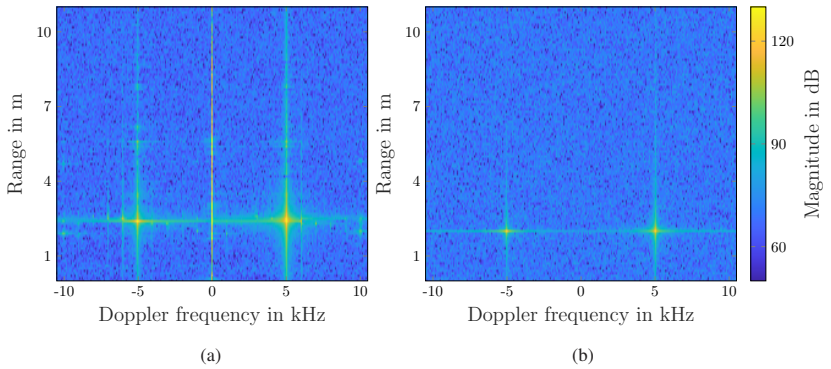

Figure 5.11: Comparison of RDMs of a single static target at 2 m distance, tagged with 5 kHz, from measurements with the assembled tag (a) and a simulation emulating this setup (b).

small ranges are not investigated within this work which is why the radar noise is considered dominant hereinafter. At 1 m distance between radar and tag, an SNR of 40 dB is reached before processing, which is well above SNR_{min} and ensures robust tag detection.

In Fig. 5.11, a RDM recorded with the assembled Doppler tag is compared to an emulating simulation. Both contain a single static target at a range of $2\,\mathrm{m}$, carrying a Doppler tag with $f_{\mathrm{id}} = 5\,\mathrm{kHz}$, at $f_{\mathrm{min}} = 60\,\mathrm{GHz}$ corresponding to $v_{\mathrm{id}} \approx 12.5\,\mathrm{m/s}$. The mixing products are visible at $\pm f_{\mathrm{id}}$ in both RDMs. Since the artificial Doppler shift f_{id} does neither imply any change in range nor a spread over multiple Doppler bins, the tag response is sharply defined. All other reflections are omitted in the simulation in Fig. 5.11b. The measurements in Fig. 5.11a contain the tag, the object reflection, and multiple reflections between radar and tag at multiples of the target range. In addition to the tag peaks at $\pm f_{\mathrm{id}}$, peaks at multiples of f_{id} occur, which originate from mixer harmonics and multiple reflections traveling through the tag repeatedly. Particularly the third harmonic, visible at $\pm 6\,\mathrm{kHz}$ due to $f_{\mathrm{D_{ua}}} = 10.5\,\mathrm{kHz}$, is pronounced and already contains slight coupling influence, making the peaks drift in opposite range directions. The static measurement surroundings are visible at 0 Hz and spread over multiple range bins.

This Doppler tag provides freedom in the used setup and enables a comparison of different topologies. The components can be adjusted, e.g., to allow for more

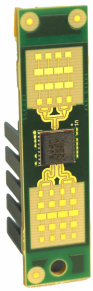

Figure 5.12: mRTS module with mixer chip, antennas, and heat sink on the reverse side.

amplification if larger ranges are investigated or add additional signal paths. Any hardware modifications are hence investigated with this tag. It offers a high SINR due to the active amplification and the limited crossover from Tx to Rx antenna. This makes it also suitable for exploring the limits of estimation accuracy. On the other hand, the tag cannot be miniaturized and is hence less suitable for the demonstration of applications. Further, the required space and connections complicate the installation in a dynamic setup. As a result, this tag is only used in static, single-tag scenarios, while dynamic scenarios and application demonstrations use mRTS tags.

5.3.2 mRTS as Doppler Tag

The mRTS tag is a commercial mRTS module from Keysight Technologies depicted in Fig. 5.12. Although not designed to be a Doppler tag, it features the basic tag setup of Fig. 5.1, yet using a single-sideband mixer. In combination with a custom supply board, one port is terminated to realize double-sideband mixing. The f_{id} feed is designed differentially and hence supplied by a universal software radio peripheral (USRP), which allows quasi-arbitrary $f_{\mathrm{id},x}$. The combination of mRTS and supply board is shown in Fig. 5.13 with and without cover. As radar target simulator, the mRTS is configured in the automotive frequency band at around 79 GHz and used together with the AWR1843BOOST. The measurements in Fig. 5.7 are recorded using mRTS tags. They contain

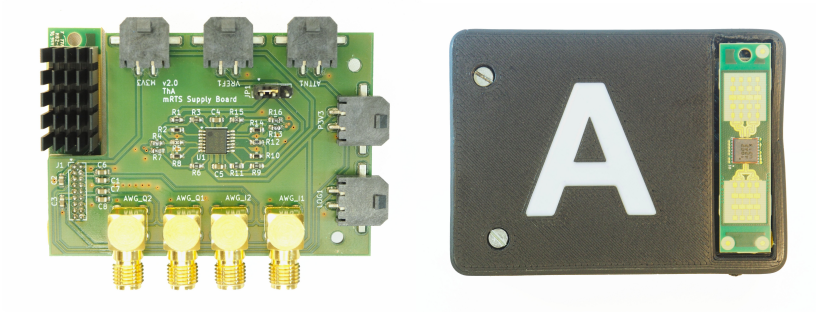

(a) (b)

Figure 5.13: mRTS module connected to the custom supply board (a) with printed cover for tag enumeration (b). The tag is connected to the reverse side of the supply board to facilitate power supply.

significantly less multiple reflections in comparison to the measurements with the assembled tag in Fig. 5.11a due to the missing amplification within the mRTS tag.
Multiple mRTS tags are available, however, their performance is not equal. This concerns mainly the transmitted signal strength, that varies over all tags. However, the varying internal signal delay is more critical as it affects range estimation in uncalibrated setups. The difference is exemplarily quantified for two tags in Fig. 5.14. The estimated range is depicted for two measurements with 10 iterations each, using tags A and B. The setup is kept constant so that the true range is unchanged and the radar is not restarted between the measurements. Results show worse repeatability for tag B and significantly varying range estimates between the tags. Repeatability cannot be addressed and remains a source of errors in measurements. Inter-tag variation is even more pronounced, however, only problematic for the application investigations which relate range measurements to multiple tags to each other. In these cases, calibration is required and performed for each tag separately to account for the distinct signal delay.

The compact form factor and multiple availability of this tag predestines it for the investigation of influence factors in multi-tag scenarios and the usage in demonstration setups for industrial applications. For most scenarios discussed in Ch. 6 and 7, mRTS tags are thus used. However, this tag does not contain

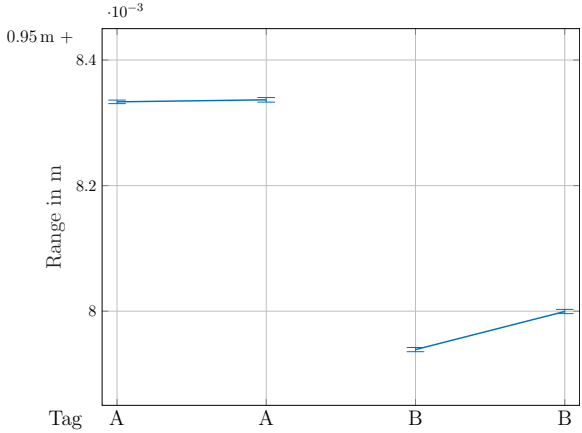

Figure 5.14: Estimated range and standard deviation of range for two times 10 iterations using tags A and B.

any amplification so that only ranges up to around 1 m provide sufficient SNR. In combination with a narrow antenna opening angle, possible tag distributions are limited and a trade-off between tag visibility and scenario coverage have to be reached. Nevertheless, the mRTS tag is a valuable extension that allows for setups not possible with the assembled tag due to tag size or quantity. It pushes the results toward realistic applications and demonstrates the applicability of Doppler tags, however, to fully exploit the tag capabilities, a tailored design would be required.

6 Estimation Performance with Doppler Tags

The idea of a Doppler tag to uniquely identify objects with conventional radar hardware and estimate their range with high accuracy was introduced. The proposed combination of hardware and signal processing enables a complete overview of the surroundings, with simultaneous identification of tagged objects and high-accuracy range estimation as well as velocity estimation for tagged and untagged objects. For practical applications, the estimation performance in regard to these three aspects, identification, range estimation, and velocity estimation, is decisive in system design and even determines viability.

This chapter investigates the performance of Doppler tags with different focus points, providing a basis for their application. All results are from measurements using the two tag implementations discussed in Ch. 5.3. Estimation capabilities are first discussed for a single tag in static and dynamic setups for reference purpose. However, Doppler tags are most interesting if applied in multiples. In such multi-tag scenarios, Doppler tags maintain their performance to ensure precise identification and ranging without interference. The corresponding metrological verification is given and forms the basis for realistic Doppler tag applications.

6.1 Estimation Capabilities for Single Doppler Tag

The investigations using a single tag are meant to demonstrate the performance capabilities of Doppler tags in optimized setups with no direct connection to applications. For this reason, the assembled Doppler tag as presented in Ch. 5.3 is mainly used for fundamental performance investigations in static scenarios.

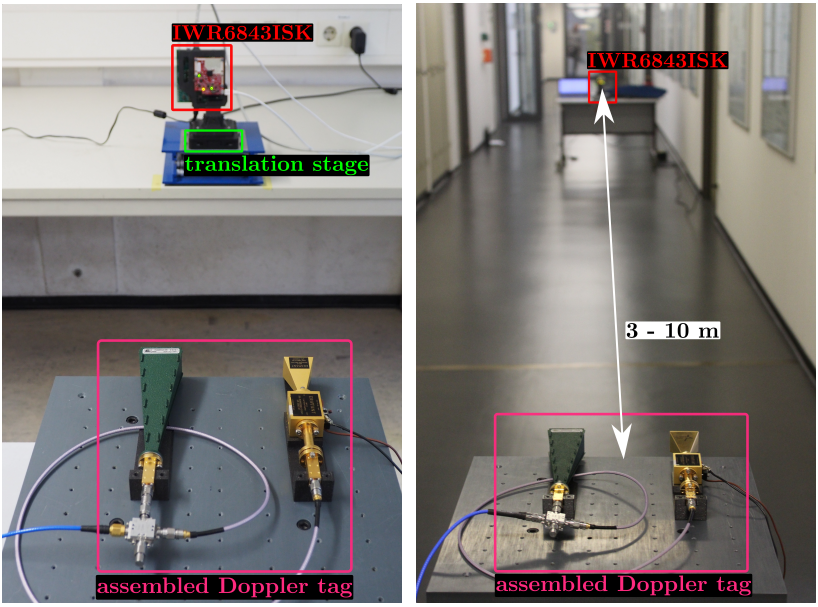

(a) (b)

Figure 6.1: Measurement setup with the radar sensor facing the assembled Doppler tag. The lab setup (a) provides a distance between radar and tag of approximately 2 m while the setup in the hallway (b) allows to measure distances up to 10 m.

The dynamic estimation performance is evaluated using an mRTS tag due to the small form factor that better integrates into the dynamic measurement setup.

6.1.1 Static Scenario

The static measurement scenario with a Doppler tag facing the radar sensor is shown in Fig. 6.1a. Both tags are used to investigate different phenomena in this setup. Identification and range estimation performance are evaluated up to large absolute values to explore the limits of the tag principle and hardware requirements using the assembled tag. Bin effects of the identification error are investigated using the mRTS tag as it allows for finer frequency steps.

Identification

In similarity to the velocity error, the identification error is determined using absolute reference values according to

$$\delta f_{\mathrm{id}} = \widehat{f}_{\mathrm{id}} - f_{\mathrm{id,set}}, \tag{6.1}$$

with the nominal identification frequency $f_{\mathrm{id,set}}$ given by a signal generator. For the assembled Doppler tag, an AFG-2225 arbitrary function generator from GW Instek is used, providing a frequency resolution of 1 µHz with a stability of $\pm 20\,\mathrm{ppm}$. For the mRTS tags, USRPs provide the identification frequency. Their precision is limited by the double-precision according to IEEE-754 [IEE85].

The reached identification error is dependent on the identification frequency f_{id}, the radar configuration, and the zero-padding factor z applied during processing. Zero padding increases the number of FFT samples so that more sine waves are reconstructed and more frequencies are distinguishable. The sampled resolution is thus improved by the zero-padding factor $\frac{\Delta f_{\mathrm{id}}}{z}$, however, the signal resolution remains unchanged, i.e., two frequencies spaced closer than Δf_{id} cannot be separated. Without interference, the identification error is within half a frequency bin, hence $\delta f_{\mathrm{id}} \in \left[0, \frac{\Delta f_{\mathrm{id}}}{2z}\right]$. For identification frequencies exactly in the center of a bin, the error theoretically vanishes, for those between two bins, it is exactly half the bin size. With the configuration given in Table 3.2 and $z = 5$, the maximum error is expected to be 11.89 Hz. Measurement results in Fig. 6.2 contain the identification error for identification frequencies around 2 kHz in steps of $\frac{\Delta f_{\mathrm{id}}}{2}$. Minimum errors of around 1×10^{-12} Hz are reached for f_{id} in the bin center while the maximum is slightly in excess of its theoretical value between the bins. Results remain unchanged for other frequencies within $f_{\mathrm{id_{ua}}}$ and are reliably reproducible. The variance of the identification error is also dependent on the absolute identification frequency. While the measurements at bin-center frequencies are highly stable and did hardly show deviations during the conducted measurements, between two bins the frequency can be assigned to an erroneous bin, resulting in errors beyond $\frac{\Delta f_{\mathrm{id}}}{2z}$. Even in such cases, the errors are small compared to the introduced identification frequencies. Particularly, they remain below the frequency resolution Δf_{id}, theoretically limiting the spacing between the frequencies of two tags. These results are independent of the used tag, however, values change with changing configuration. Further investigations are conducted using the assembled tag, particularly because bet-

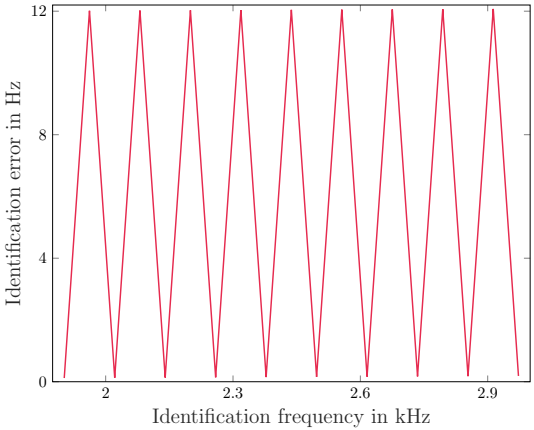

Figure 6.2: Identification error over identification frequency in steps of half the frequency resolution. The error alternates between two values as result of the bin effect.

ter range estimation performance is expected.
According to the basic Doppler tag idea, small identification frequencies of a few kHz are mainly applied, emulating a motion-induced Doppler shift. However, larger shifts can be favorable, particularly if a large number of tags is required or multiple tagged and untagged objects are in motion and tag frequencies can be chosen above the expected motion-caused Doppler shifts. This simplifies the differentiation between tagged and untagged objects and avoids overlapping of peaks of multiple tagged targets in motion, which would complicate processing. Larger identification frequencies yet increase coupling terms which in turn complicate tag separation, hence f_{id} choice and processing should be tailored to the application scenario.

Identification frequencies up to 40 kHz are investigated in Fig. 6.3, depicting the mean of the identification error δf_{id} over 100 iterations. The maximum unambiguous identification frequency is 10.5 kHz, all frequencies above are processed in their Nyquist zone, respectively. The achieved identification error is stable and well below the frequency resolution over all identification frequencies, preventing tag confusion. With an average value of 3×10^{-12} Hz, the standard deviation over multiple measurements is negligible. From an identification perspective, frequencies above the maximum unambiguous frequency

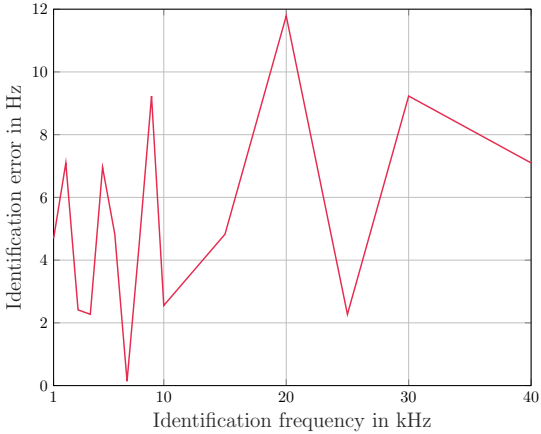

Figure 6.3: Mean of identification error over applied identification frequencies. Identification errors well below the frequency resolution ($\Delta f_\mathrm{D} = 82.4\,\mathrm{Hz}$) are achieved for all identification frequencies, preventing tag confusion.

can hence be used if the overall system design ensures unique assignment of tag frequencies to objects. However, coupling terms become significant and require consideration as discussed in Ch. 5.

Potential time dependencies of the Doppler tag are investigated with measurements lasting 1 min and repeated twice with 30 min break in between, during which the Doppler tag is continuously operating. The estimated identification frequency over time is visualized with a short-time Fourier transform (STFT) for $f_\mathrm{id,set} = 5\,\mathrm{kHz}$ in Fig. 6.4. The identification frequency is constant over time with an error significantly below typical frequency spacing. No noticeable deviations occur so that solid identification is permanently possible. However, this result is only transferable to other tag hardware to a limited extent as time-dependent phenomena such as drifts or heating are highly hardware specific.

The range dependency of the identification error is investigated up to a distance of 10 m with the setup in Fig. 6.1b. Ranges are measured manually with limited accuracy, as not the specific range but the invariance of $\widehat{f}_\mathrm{id}$ over different ranges is of interest. While the tag is reliably detected, it is identified accurately; in the basic Doppler tag setup up to a range of 3 m. Beyond, the tag response is too weak and undetectable due to a low SNR, hence a tag frequency of

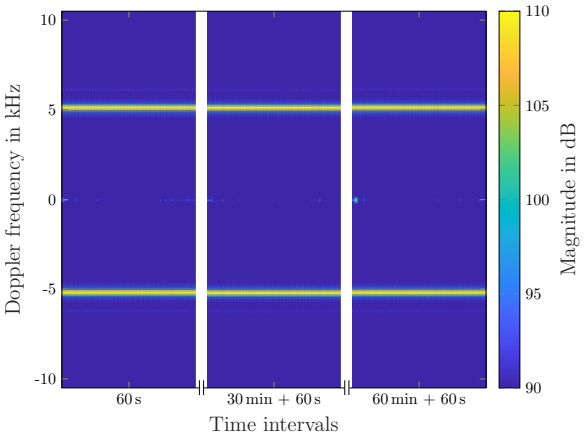

Figure 6.4: Tag frequency over time in three intervals of 60 s with 30 min in between. The Doppler tag is operating continuously without noticeable deviations.

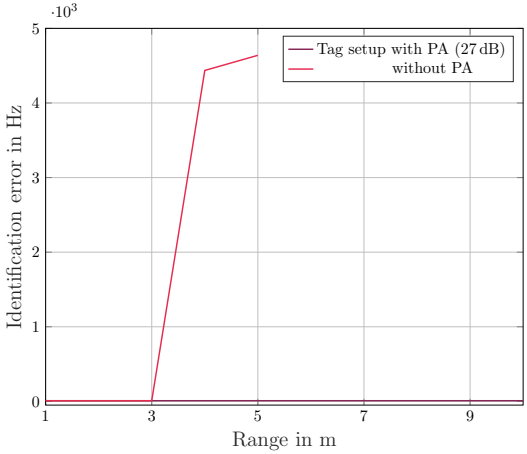

Figure 6.5: Identification error over measurement range for a Doppler tag of $f_{\mathrm{id,set}} = 5\,\mathrm{kHz}$ with and without PA. Tag identification is possible while the signal strength is sufficient for reliable detection.

0 Hz is estimated, resulting in $\delta f_{\mathrm{id}} = f_{\mathrm{id,set}} = 5\,\mathrm{kHz}$. Consequently, this is the

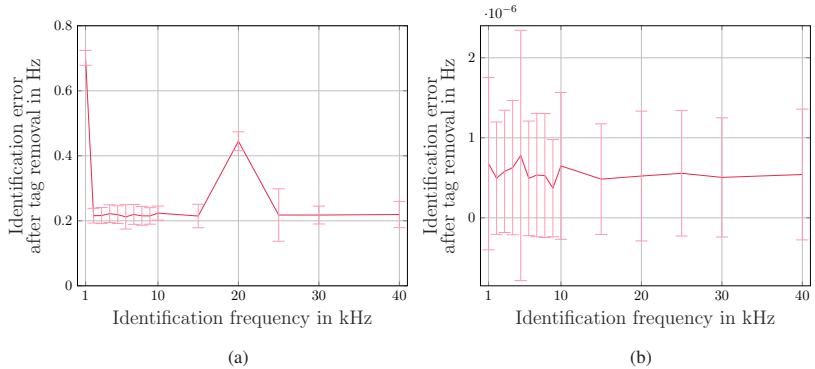

Figure 6.6: Mean of absolute identification error over applied identification frequency after Doppler tag removal (a) and after additional Doppler correction (b), including the standard deviation as error bars. While residual f_{id} shifts remain after non-ideal tag removal, an additional Doppler correction removes them.

maximum detectable range R_{max} according to (2.26) for the assembled tag without additional amplification. Adding a power amplifier to the transmit path of the tag extends the maximum detectable range, exemplified in Fig. 6.5 with an amplifier gain of 27 dB. The identification error remains stable across all detectable ranges with no deviations or variations. Further, there is no relation between SNR and identification accuracy, with the result that $\delta f_{\mathrm{id}} = 6.9\,\mathrm{Hz}$ for both Doppler tag setups and as shown in Fig. 6.3. Reliable identification is hence provided up to R_{max}, for which application-specific requirements have to be considered during tag design.

After successful identification, the artificial Doppler shift has to be removed to allow for unimpaired range estimation. As discussed in Ch. 5.1, the two sidebands are separated and multiplied to eliminate both frequency and phase shift originating from the tag operation. Residual f_{id} components in the signal would result in a bias in range estimation if not corrected, hence deteriorating the estimation accuracy. Ideally, no tag influence is left after elimination, and only static targets remain for range estimation. This is confirmed in Fig. 6.6a, where frequency and phase shift are removed from the measurements of Fig. 6.3. The identification error after tag removal describes deviations of a Doppler estimation from the expected value of 0 Hz. Those are small over all $f_{\mathrm{id,set}}$, which proves a successful tag elimination. Slightly larger deviations are observed for

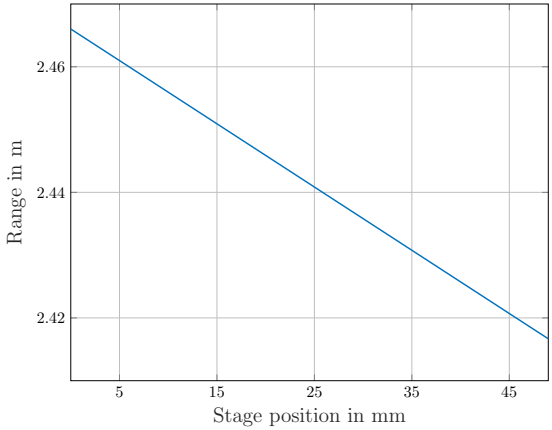

Figure 6.7: Estimated range between radar and Doppler tag over a measurement range of 50 mm for $f_{\mathrm{id,set}} = 5\,\mathrm{kHz}$. The radar approaches the tag in steps of 1 mm.

1 and 20 kHz, where the latter corresponds to 1 kHz in the second Nyquist zone. They stem from the zero-Doppler peak complicating sideband separation as parts of it may be contained within the sideband window, impairing tag elimination. The peak is closer for lower frequencies than for higher ones, hence the effect is even more prominent at identification frequencies below 1 kHz. An additional Doppler correction significantly improves the elimination for all identification frequencies and leaves almost purely static signal components as ascertained in Fig. 6.6b, even for 1 and 20 kHz. The residual artificial Doppler is negligible. Therefore, the static-target requirement for high-accuracy range estimation is fulfilled.

Range Estimation

Range estimation is evaluated using the M-683 translation stage (Ch. 3.2.1) over a measurement range of 50 mm in steps of 1 mm. The estimated range depicted in Fig. 6.7 starts at approximately 2.5 m, and the radar approaches the tag stepwise but remains static during each measurement.
The range error δR_{fin} is defined according to (4.37), assuming a constant signal propagation time within the tag. In Fig. 6.8a, it is compared for a Doppler tag

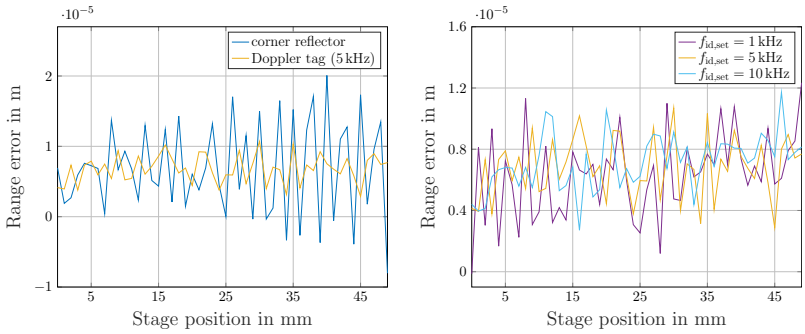

Figure 6.8: Comparison of the range error δR_{fin} for a Doppler tag with $f_{\mathrm{id,set}}$ = 5 kHz and a corner reflector (a) and for identification frequencies of 1, 5, and 10 kHz. The absolute distance between radar and target is approximately 2.5 m at the first stage position.

with $f_{\mathrm{id,set}}$ = 5 kHz and the corner reflector used previously in Ch. 4.3. The range error toward a Doppler tag is smaller ($\overline{|\delta R_{\mathrm{fin}}|}$ = 6.8 µm) than toward the corner reflector ($\overline{|\delta R_{\mathrm{fin}}|}$ = 7.7 µm) and shows enhanced stability over the stage positions. This is attributable to the dependency of accuracy on SNR, which is higher for the active Doppler tag. In addition, the measurement surroundings are effectively suppressed during Doppler tag elimination, further enhancing the range estimation similarly as for a target in motion in Fig. 4.22. Beyond these enhancements, the tag impact is successfully eliminated, allowing for undisturbed range estimation. However, a bias from zero mean is observable for measurements with and without tags in this setup.

Successful tag elimination and subsequent range estimation applies to all identification frequencies within the scope of unambiguousness as exemplarily shown in Fig. 6.8b for 1, 5, and 10 kHz. The variation in the range error for $f_{\mathrm{id,set}}$ = 1 kHz is slightly larger than for the other frequencies, attributable to the proximity to zero Doppler. However, the error values are not increased and all three frequencies provide comparably reliable performance with absolute mean errors $\overline{|\delta R_{\mathrm{fin}}|}$ of 6.3 to 7.2 µm. Absolute means herein coincide with signed means due to the bias. A significant improvement is achieved in comparison to frequency analysis as contrasted in Fig. 6.9 for 1 and 10 kHz. Not only the range error but also its variations are considerably reduced with the combined analy-

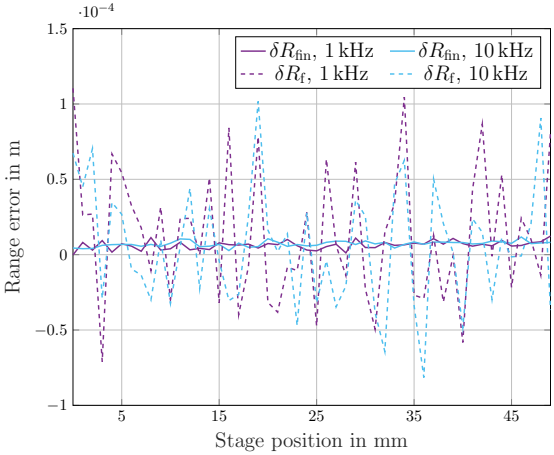

Figure 6.9: Range error for a Doppler tag with $f_{\mathrm{id,set}}$ = 1 and 10 kHz for frequency-based range estimation δR_{f} (dashed) and $f\varphi$ range estimation δR_{fin} (solid), visualizing the estimation improvement of the latter.

sis, despite a small remaining offset. The results show no significant influence of tag frequency, so range estimation with comparable accuracy is performed for all tagged objects in a given scenario.

Irrespective of the tag frequency, the range error is expected to be range-dependent due to the change in SNR. Adding a power amplifier to the transmit path of the tag can hence enhance estimation accuracy. Particularly for large ranges, the target peak can be amplified to rise above the noise floor that would otherwise hide it as found in Fig. 6.5 discussing identification. Figure 6.10a contains the average range error over 100 iterations in the center stage position for ranges up to 10 m. A Doppler tag setup with $f_{\mathrm{id,set}}$ = 5 kHz and including a power amplifier with 27 dB gain is used. Errors are comparable within the investigated range with a slight tendency toward higher errors at higher ranges. However, the minimum and maximum error values, represented by error bars, increase significantly with higher ranges. Consequently, the probability of outliers increases, and the estimation reliability diminishes for larger ranges. If the number of measurements is thus increased to 300 iterations at each of the 50 stage positions, resulting in a total of 15000 measurements, this effect is revealed. With the variation in measurement position and the large number of

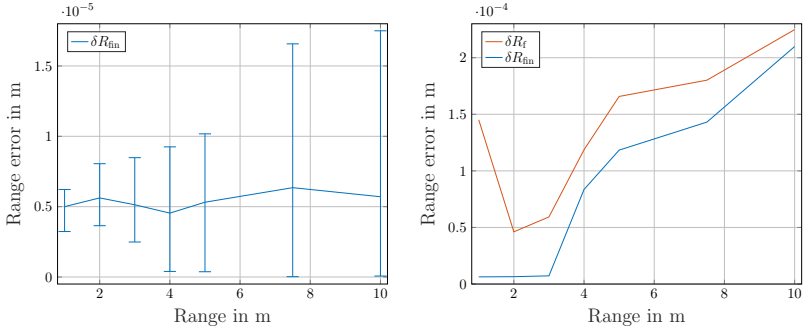

Figure 6.10: Mean of absolute range error over 100 iterations per range (a), including minimum and maximum values as error bars, and over 300 iterations and 50 stage positions per range (b), both for a Doppler tag with $f_{\mathrm{id,set}} = 5\,\mathrm{kHz}$. Erroneous bin choices occur more frequently for larger ranges.

measurements, outliers are likely to be included if they occur. This is observed from a range of 4 m in Fig. 6.10b. In the majority of cases, an erroneous bin is selected so that an error the size of one bin $\left(\frac{c}{2f_{\mathrm{min}}} = 2.5\,\mathrm{mm}\right)$ occurs. As only absolute values are given consideration, the mean error directly increases with the occurrence of more frequent bin errors. The comparison to frequency analysis indicates that phase-offset analysis can only significantly enhance range estimation up to a relatively small range. Beyond, both approaches result in similar range errors as $f\varphi$ analysis is based on frequency analysis for bin selection and phase correction. Therefore, $f\varphi$ analysis is most suitable for short ranges, whereas frequency analysis can provide comparable range estimation over large distances. This is compliant with typical requirements, as high accuracy is primarily requested in close proximity, while at several meters distance, mm-accuracy is mostly sufficient. A range-dependent processing decision can reduce computational effort and still benefit from exceptionally high accuracy where required.

While increased amplification within the tag is beneficial for large ranges, it can deteriorate the range estimation for small ranges as contrasted in Fig. 6.11 for no additional amplification, a PA with 27 dB, and a PA with 33 dB in a setup according to Fig. 6.1a. The deterioration stems from the amplification of both the intended target peak and multiple reflections, which distort range

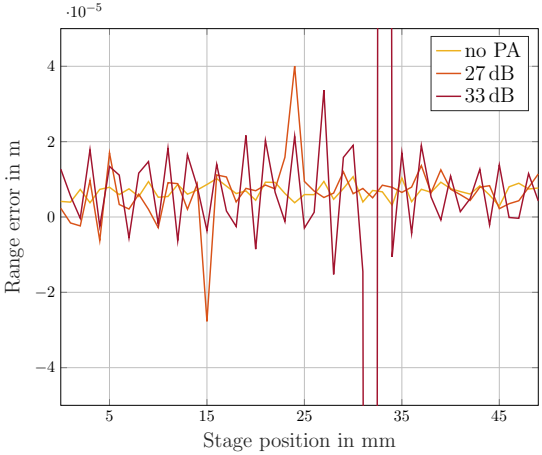

Figure 6.11: Range error for a Doppler tag with $f_{\mathrm{id}} = 5\,\mathrm{kHz}$ and different amplifications within the tag. The measurement setup remains unchanged, assigning deteriorations to the additional amplification at short ranges ($\approx 2\,\mathrm{m}$).

estimation. It hence depends on the actual application if an improvement is accomplished using an additional power amplifier and if it justifies the more complex tag setup. In any case, the Doppler tag can enlarge the operational range in comparison to passive targets and allow for efficient clutter suppression to support highly accurate range estimation for tagged objects.

6.1.2 Dynamic Scenario

The Doppler tag exploits an artificial Doppler shift for object identification, making its performance under motion particularly interesting. The first investigation on this is published in [14].
The dynamic measurement setup shown in Fig. 6.12 is adopted from Ch. 4.3 with a tag instead of a corner reflector. The mRTS tag is selected for its compact form factor and ease of implementation. For each of the measured velocities, the sled is evaluated in constant motion, enabling unimpaired range estimation. Identification and velocity estimation do not require constant motion and could be applied while velocity changes, however, only coarse range estimation would

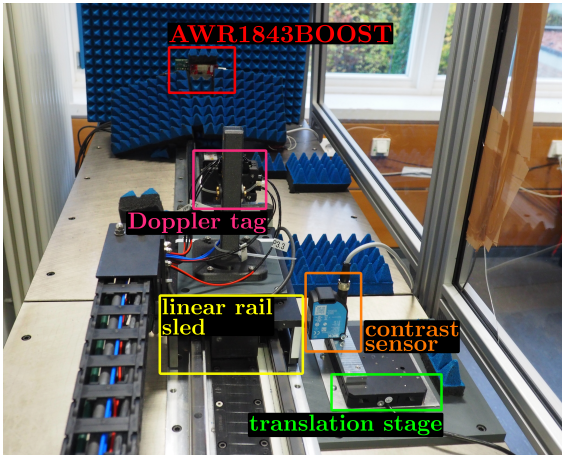

Figure 6.12: Dynamic measurement scenario with an mRTS tag mounted on the linear rail. The contrast sensor on the translation stage next to it triggers each measurement in passing.

be available. The peak pair from double-sideband mixing allows for an unambiguous tag assignment without velocity dependent guard intervals, which would be indispensable in dynamic scenarios with single-sideband mixing.
The tag motion shifts the characteristic peak pair in Doppler direction and the

Table 6.1: Parameters for the AWR1843BOOST used with an mRTS tag in a dynamic scenario.

Minimum frequency f_{min}	77.0 GHz
Sampled bandwidth B	3.70 GHz
Number of samples per chirp N_{s}	256
Number of chirps N_{c}	255
Range resolution ΔR	0.04 m
Maximum unambiguous range R_{ua}	5.18 m
Velocity resolution Δv	0.10 m/s
Maximum unambiguous velocity v_{ua}	13.3 m/s
Frequency resolution Δf_{D}	53.9 Hz
Maximum unambiguous frequency $f_{\mathrm{D_{ua}}}$	6.88 kHz

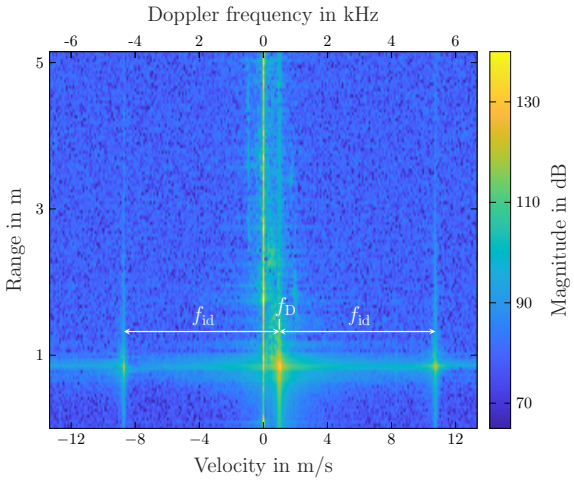

Figure 6.13: RDM for an mRTS tag with $f_{\mathrm{id}} = 5\,\mathrm{kHz}$ and $f_{\mathrm{D}} = 0.5\,\mathrm{kHz}$, corresponding to $1\,\mathrm{m/s}$. The tag response is visible around the direct object reflection and clutter from the static measurement surroundings occurs at $0\,\mathrm{m/s}$.

sum of motion-induced and artificial Doppler shift is restricted by the maximum unambiguous frequency, limiting the number and spacing of usable tag frequencies and admissible velocities. Conversely, the frequency resolution is crucial for tag elimination and Doppler correction and affects the achievable accuracy, requiring a trade-off. For the used configuration in Table 6.1, priority is on the estimation accuracy, hence frequency resolution is privileged over maximum unambiguous frequency, limiting the usable identification frequencies and sled velocities.

A measured RDM containing a tag with $f_{\mathrm{id}} = 5\,\mathrm{kHz}$ and a motion-induced Doppler shift of $f_{\mathrm{D}} = 0.5\,\mathrm{kHz}$, corresponding to 1 m/s, is depicted in Fig. 6.13. The peak pair is separated by $2f_{\mathrm{id}}$ and centered on the original object reflection at f_{D}. For the direct object reflection, range-Doppler migration occurs due to the movement of the tag. The artificial Doppler shift does not induce additional migration, but the tag peaks experience the same range migration as the object reflection. The object reflection as well as static reflections from the measurement surroundings are considerably stronger than the tag response. Active amplification within the tag can provide sufficient signal strength also

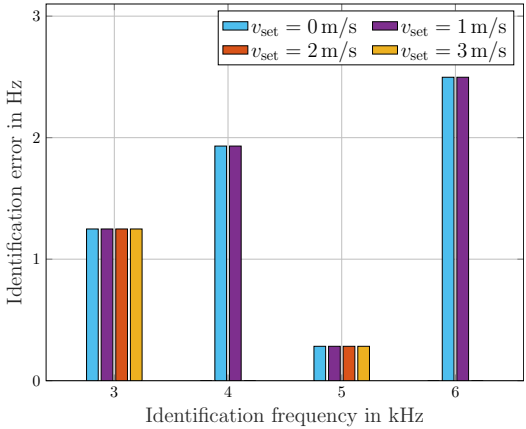

Figure 6.14: Identification frequency error for a Doppler tag with $f_{\mathrm{id}} = 3$ to $6\,\mathrm{kHz}$ and $v_{\mathrm{set}} = 0$ to $3\,\mathrm{m/s}$. The error reliably remains unchanged for increasing velocities.

for longer ranges and is thus recommended for tailored tag design.
The influence of motion on the tag performance is characterized in terms of the errors in estimated identification frequency, range, and velocity, evaluated according to (6.1), (4.37), and (4.38).

Identification

As in the static scenario, the identification error δf_{id} is dependent on the identification frequency, the frequency resolution, and the zero-padding factor. Figure 6.14 depicts the characteristic error for each identification frequency, which is stable over measurement positions and tag velocities. The identification errors differ in dependency of the applied identification frequency but are considerably smaller than those, ranging from 0.3 to 2.5 Hz in this investigation. Objects with different $f_{\mathrm{id},x}$ are hence comparably well identified. Errors are also well below the frequency resolution limiting the usage of adjacent identification frequencies, hence confusion of tags is debarred. The identification errors for zero and non-zero velocities coincide and no influence of the dynamic measurement scenario is observed regarding identification. This proves the

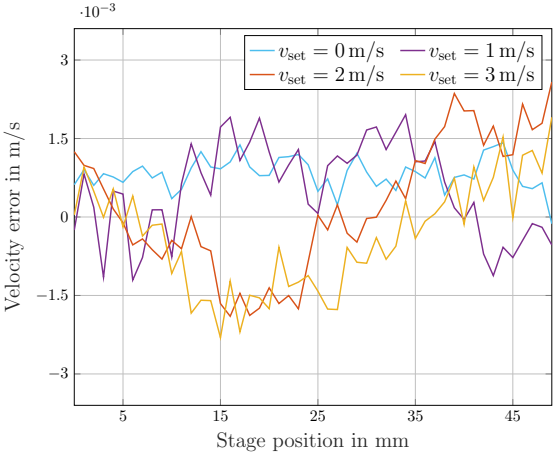

Figure 6.15: Velocity error for a Doppler tag with 5 kHz and velocities of 0 to 3 m/s. The error comprises oscillations from the rail control not accounted for in the nominal velocity, but beyond that, there are no significant deviations.

robustness of identification against motion-induced Doppler shifts and allows for utter tag elimination.

Velocity Estimation

The velocity error is depicted in Fig. 6.15 for velocities of 0 to 3 m/s and an identification frequency of 5 kHz. Mean velocity errors $\overline{|\delta v|}$ of 0.9 to 1.1 mm/s are achieved for 1 to 3 m/s while $\overline{|\delta v|} = 0.8\,\text{mm/s}$ for a static tag. Comparable velocity errors are found for other identification frequencies. In comparison to velocity estimation with the corner reflector in Ch. 4.3.2, the error for 0 m/s increased while the errors for non-zero velocities are significantly improved and particularly the systematic increase of the velocity error for increasing velocities is not observed, attributable to the active tag signal. In the smaller velocity errors, oscillations are apparent, which originate from the rail control and reflect the actual non-linear behavior of the rail as discussed prior in Ch. 4.3.2. This effect is not accounted for in the nominal velocity and hence causes higher error values in comparison to the static case and as to be expected

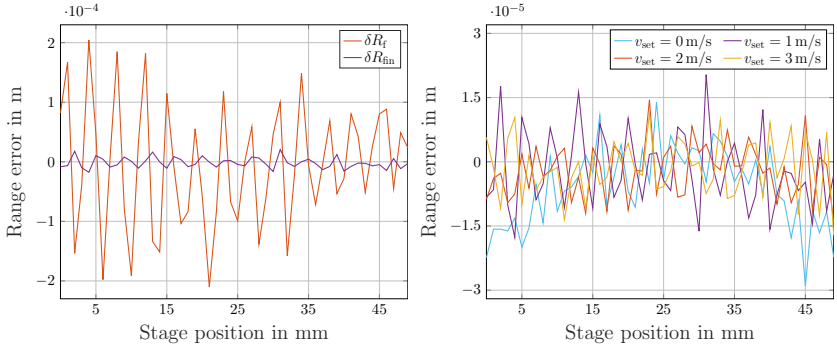

Figure 6.16: Range error for a Doppler tag with 5 kHz, moving with 1 m/s, (a) and for velocities of 0 to 3 m/s (b). The error after frequency analysis (δR_f) is compared to that after $f\varphi$ analysis (δR_fin). Results are similar to those from Fig. 4.22, obtained with a corner reflector, and demonstrate the robustness of range estimation despite tag operation.

in real scenarios. The achieved velocity estimation is accurate and well-suited for utilization, e.g., in tracking tasks. This also verifies a successful tag elimination as otherwise, remaining artificial Doppler shifts would cause deviations in the velocity estimation. In conjunction, tag elimination and motion-induced Doppler correction are the prerequisites for highly accurate range estimation.

Range Estimation

Unimpaired range estimation relies on utter tag elimination and Doppler correction and is hence dependent on prior processing performance. Additionally, it is more sensitive to external influences such as motion, decreasing signal strength, and setup alignment. This complicates result interpretation as it is difficult to establish a cause-and-effect relationship for deviations or trends. Nevertheless, the range error is an important evaluation criterion in tag and system characterization, although both cannot be unambiguously separated.
Results are given for an identification frequency of 5 kHz while other frequencies provide comparable values. As shown in Fig. 6.16a for an mRTS tag moving with 1 m/s, the error after frequency evaluation δR_f reaches values twice as high as in the static scenario with the assembled Doppler tag (Ch. 6.1.1). $f\varphi$ ana-

lysis can significantly enhance range estimation but absolute errors are still increased in comparison to the static investigation ($\overline{|\delta R_{\mathrm{fin}}|}_{\text{Fig. 6.8b}} = 6.8\,\mu\mathrm{m}$ and $\overline{|\delta R_{\mathrm{fin}}|}_{\text{Fig. 6.16a}} = 7.5\,\mu\mathrm{m}$). The deterioration is attributed mainly to the change in the used tag and the corresponding lack of amplification, but also the measurement scenario. Conversely, the bias observed in Fig. 6.8 is not included in the estimated range and errors are well-balanced ($\overline{\delta R_{\mathrm{fin}}}_{\text{Fig. 6.16a}} = -1.8\,\mu\mathrm{m}$). A comparison of the range errors after $f\varphi$ analysis for velocities of 0 to 3 m/s in the dynamic setup is presented in Fig. 6.16b. Average errors of $\overline{|\delta R_{\mathrm{fin}}|} = 5.2$ to $7.5\,\mu\mathrm{m}$ and $\overline{\delta R_{\mathrm{fin}}} = -1.5$ to $-2.0\,\mu\mathrm{m}$ are reached for 1 to 3 m/s, indicating small and balanced deviations from ground truth. For the static measurement in this setup (Fig. 6.16b), errors are slightly larger ($\overline{|\delta R_{\mathrm{fin}}|} = 8.7\,\mu\mathrm{m}$) and less balanced ($\overline{\delta R_{\mathrm{fin}}} = -6.0\,\mu\mathrm{m}$).
The error values as well as their variations over stage positions are in excess of the static setup in Ch. 6.1.1, particularly for $v_{\mathrm{set}} = 0\,\mathrm{m/s}$. Beside the influence of the tag hardware, this is attributable to the modified measurement environment, which contains significantly more metallic components. The range errors are very similar to those in Fig. 4.22, recorded in the same setup using a corner reflector. Consequently, the artificial Doppler shift introduced by the tag does not affect range estimation. Errors remain stable even at increased velocities although residual velocity components from non-ideal Doppler correction would have a stronger impact, implying profound tag-caused and motion-induced Doppler correction.
However, an artificial deterioration of the velocity resolution as applied in Ch. 4.4 reveals the importance of adequate radar configuration. Increasing the velocity resolution by a factor of 3 ($u = \frac{1}{3}$) still allows for reliable identification and the identification error remains unchanged. Velocity and range error, which are estimated with higher accuracy, are deteriorated by a factor of 2 to 3. Further increasing the velocity resolution inhibits tag identification, initially in some positions but entirely for $u < \frac{1}{5}$. Meaningful velocity and range estimation are consequently not possible. The velocity resolution is hence a crucial parameter to be considered during system specification.

The achieved error values have to be contextualized scenario-dependent. For objects in motion, the initial range at the measurement start is estimated. With errors up to $\pm 20\,\mu\mathrm{m}$, an estimation at 1 m/s remains valid for around 40 µs, afterwards the object has moved beyond the uncertainty interval. In combination with a measurement duration of 73 µs, disregarding processing times, the found range errors are far from limiting the system performance. If higher update rates

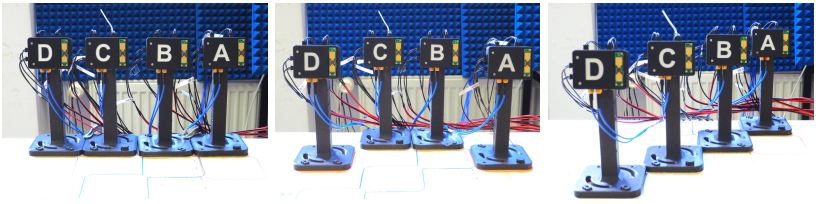

(a) (b) (c)

Figure 6.17: Tag constellations 1 to 3 (a to c), containing different distributions of four tags A to D. The radar is centered in front of tag B.

are required, the range can be tracked within consecutive measurements using the velocity estimate. Tag operation does hence not degrade estimation accuracy or introduce additional errors, but enables concomitant identification. In summary, Doppler tags provide reliable identification and parameter estimation despite motion.

6.2 Doppler Tags in Multiples

Doppler tags are particularly applicable when used in multiples, hence the influence of multiple tags on each other is investigated with different setups and identification frequency sets containing up to four tags as originally published in [12].

The setups are shown in Fig. 6.17 and face the radar sensor on the translation stage for relative reference. All setups contain four tags, which are activated in the sequence B-A-C-D to investigate the impact of an increasing number of active tags. As relative evaluation is only valid if the tag is centered in front of the radar, range estimation is performed only for tag B. The tags are arranged close to each other to be in short range from the radar and within the radar FoV to overcome the visibility limitations of the mRTS tags, although resulting in rather unrealistic scenarios. Separation is ensured from the tag functionality as discussed in Ch. 5.1.3 and not dependent on the radar resolution. While the shown setups provide visibility for all four tags, constellations with tags in a line toward the radar result in masking and the rear tags are not detected, hence these setups are omitted. However, wider tag opening angles in future hardware could facilitate such setups. Constellations with deteriorated tag visibility due

Table 6.2: Identification frequency sets 1 to 4.

	Tag A	Tag B	Tag C	Tag D
f_{id}-set 1	3 kHz	6 kHz	9 kHz	12 kHz
f_{id}-set 2	2 kHz	5 kHz	7.5 kHz	11 kHz
f_{id}-set 3	3 kHz	4 kHz	5 kHz	6 kHz
f_{id}-set 4	9 kHz	10 kHz	11 kHz	12 kHz

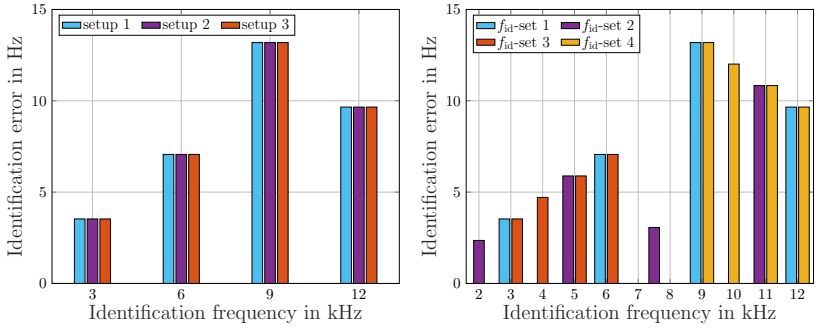

(a) (b)

Figure 6.18: Identification error over applied identification frequency for three setups using f_{id}-set 1 (a) and four f_{id}-sets in setup 1 (b). Results for four activated tags are shown, however coincide with those using less tags. The identification error is frequency dependent but stable over the setups and sets as well as the number of tags.

to angular displacement are not investigated as these are highly tag hardware dependent.
Four identification frequency sets, defining the applied $f_{\mathrm{id,x}}$ for each tag, are used as specified in Table 6.2. They allow for the investigation of different absolute identification frequencies, frequency spacings between tags, and the impact of multiples within a set.

6.2.1 Identification

The identification error is contrasted in Fig. 6.18 for the different setups and sets. It is not affected by the activation of additional tags which is why results are only

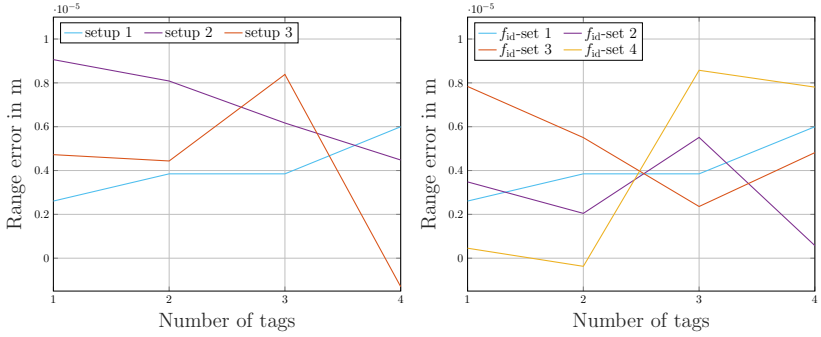

Figure 6.19: Range error over the number of active tags for three setups using f_{id}-set 1 (a) and four f_{id}-sets in setup 1 (b). Errors are depicted for tag B and demonstrate the independence of range estimation from multi-tag setups and used identification frequencies.

depicted for four active tags, however perfectly coinciding with those of less tags. Error values of the same tag are identical in different setups (Fig. 6.18a) and for different f_{id}-sets (Fig. 6.18b). Particularly, neither closer frequency spacing nor multiples within a set deteriorate identification. Depending on the applied identification frequency, the absolute error differs due to the bin effect as discussed in Ch. 6.1.1, however, no additional impacts were found. All setups and f_{id}-sets lead to a comparable identification performance, forming the basis for multi-tag applications and further processing.

6.2.2 Range Estimation

The range error in the center stage position is presented for the different setups and f_{id}-sets in Fig. 6.19. It is much more sensitive to other tags or setup modifications. In addition, it varies over repeated measurements, which makes it difficult to interpret the results clearly and assign causes to implications. However, these variations are small and cannot mask significant trends or deviations. The error remains small and comparable to prior investigations. Despite variations over the number of tags, setups, and f_{id}-sets, no trends or significant or sudden increases are observed. Neither does activating more tags reliably increase the range error nor is there a clear dependence on setup or f_{id}.

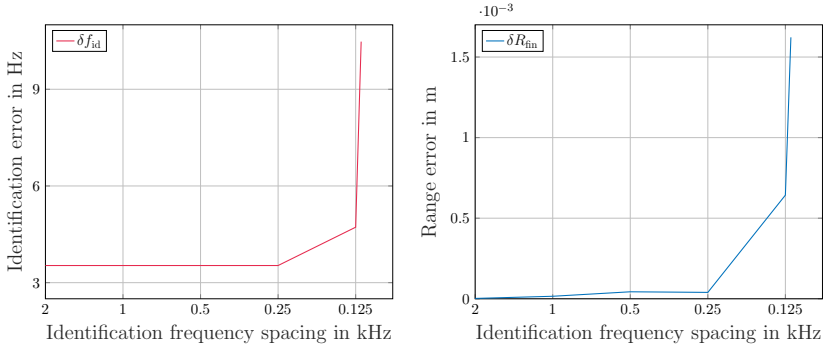

Figure 6.20: Identification error (a) and range error (b) for tag B over decreasing identification frequency spacing to neighboring tags in setup 1. Identification and range estimation are accurately possible until around twice the frequency resolution ($\Delta f_{\mathrm{id}} = 119\,\mathrm{Hz}$) and deteriorate rapidly thereafter.

Regarding the latter, closer frequency spacing Λ to the degree investigated in the f_{id}-sets does not degrade range estimation with mRTS tags. They contain limited signal amplification and interference between tags is negligible. However, if the frequency spacing is too close, the tags cannot be reliably separated in the RDM and, although identification is still possible, the tag elimination is insufficient and impairs range estimation. This is found in continuative measurements with decreasing Λ between identification frequencies, applied to four tags ($f_{\mathrm{id,A}} = 3\,\mathrm{kHz} - \Lambda$, $f_{\mathrm{id,B}} = 3\,\mathrm{kHz}$, $f_{\mathrm{id,C}} = 3\,\mathrm{kHz} + \Lambda$, $f_{\mathrm{id,D}} = 3\,\mathrm{kHz} + 2\Lambda$) in setup 1 as depicted in Fig. 6.20. An estimation deterioration is clearly observed from around twice the frequency resolution ($\Delta f_{\mathrm{id}} = 119\,\mathrm{Hz}$), however, slight deterioration occurs earlier. The last measurement point in Fig. 6.20 is taken at a frequency spacing equal to the frequency resolution. Identification is possible but identification errors increase. Tag elimination is not successful anymore and the range error significantly increases due to a corrupted phase information, impeding $f\varphi$ estimation. However, such close frequency spacing is not aimed for in practical applications where a margin of a few frequency bins allows for robust tag performance.

Presented results indicate robust performance and highlight the reliability and versatility of Doppler tags. Identification errors are within a few Hertz, constrained by frequency resolution and zero-padding factor. Based on this identification, successful tag elimination is demonstrated, enabling velocity errors of around 1 mm/s and range errors of 5.2 to 8.7 µm in static and dynamic scenarios. These are excellent results for estimation relying on commercial radars and non-optimized tag hardware. Multiple objects can be supplied and experience comparable performance. The findings establish Doppler tags as a flexible and scalable solution, ideal for applications requiring simultaneous identification, velocity estimation, and accurate range estimation for multiple targets.

7 Exemplary Applications with Doppler Tags

Previous investigations have demonstrated the functionality and performance of Doppler tags in different scenarios. Results prove a reliable radar-tag system and position the Doppler tag for versatile applications wherever joint identification and accurate range and velocity estimation is required. This chapter exemplarily showcases practical applications with Doppler tags and indicates what is yet to come. Typical tasks from an industrial context are chosen, highlighting the suitability of Doppler tags for this field. However, the Doppler tag idea is not based on or limited to a distinct area or application.

Both tag implementations introduced in Ch. 5.3 are used hereinafter, enabling a proof of principle for different applications while not being optimized to them. The application examples hence demonstrate the potential of the radar-tag system, but also challenges and limitations from which design decisions can be derived.

Doppler tags are shown to operate reliably in different scenarios, such as in close proximity to strongly reflecting targets. The data contained in their identification frequency can be tiered, providing information beyond object identification. Particularly spatial information, such as position or object orientation, is essential for autonomous systems operating in dynamic and unstructured environments and estimated using Doppler tags. The initial demonstration of orientation estimation and self-positioning is published in [1]. This expands the applicability of radar sensors offering promising capabilities for spatial awareness and precise movement. Autonomous robots and self-driving vehicles rely on such information for object interaction or obstacle avoidance. Thus, new functionalities transform radar-tag systems into holistic concepts, delivering a multiplicity of data simultaneously.

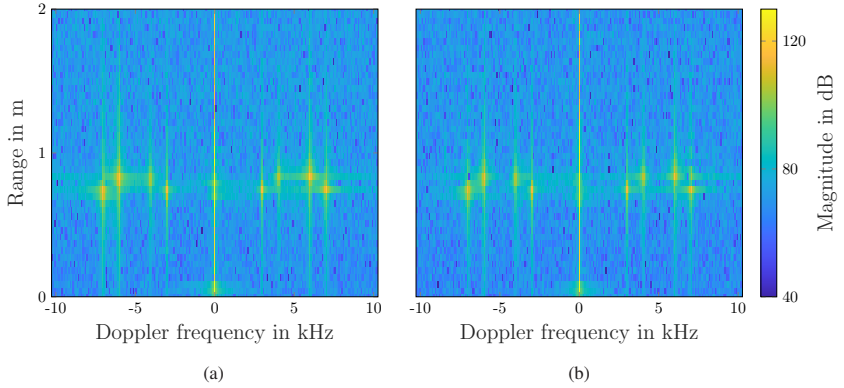

Figure 7.1: RDM for four tags all visible to the radar (a) and with a cardboard box around the two tags with 4 and 6 kHz (b). Hardly any influence on the RDM due to the box is observed, indicating robust hidden-object detection.

7.1 Scenario-aware Tag Features

Hidden Tag Detection

Doppler tags allow for unique identification without relying on optical information about the object. This applies even to objects contained in cardboard or thin plastic boxes as long as the Doppler tag is detectable. Radar signals at 60 or 77 GHz can easily penetrate cardboard, plastics, or even glass. In Fig. 7.1, measurements with and without a box are compared. While all four mRTS tags (3, 4, 6, and 7 kHz) are directly visible to the radar in 7.1a, a typical cardboard shipping box covers the tags tagged with 4 and 6 kHz in 7.1b. The impact on the RDM, however, is marginal. This is of interest in transport and logistics, but also for hidden-object detection in any other circumstances.

Multi-stage Identification

While Doppler tags inherently enable unique object identification, in some contexts more than just identification is favorable. The state of the object, its affiliation to different groups, or even communication to some extent are of

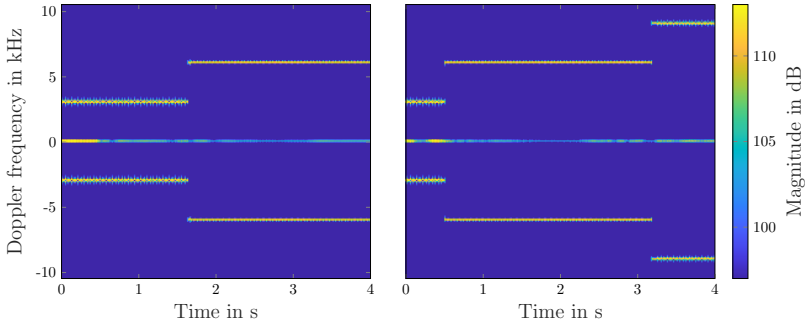

Figure 7.2: STFT visualizing multi-stage identification with switching in f_{id} from 3 to 6 kHz (a) and 3 to 6 to 9 kHz (b).

interest in autonomous environments. With the basic setup discussed in Ch. 5, such data cannot be extracted from radar sensing to Doppler tags. However, switching f_{id} during one measurement allows for a multi-stage identification imparting tiered information. Each $f_{\mathrm{id,x}}$ conveys a piece of information, jointly characterizing the tagged object in excess of pure identification.
In Fig. 7.2, switching with two and three stages is realized using the assembled Doppler tag. A manual switch is performed from 3 to 6 and 9 kHz. The individual $f_{\mathrm{id,x}}$ are clearly differentiated and an edge detection enables separate processing. Each determined identification frequency contains one part of the transmitted information, such as the kind of object, its unique identification, or its activity status. From the combination of different $f_{\mathrm{id,x}}$, a variety of information content can be accessed, and even control symbols, contextualizing posterior frequencies, can be implemented in the same way.
If multiple tags are visible simultaneously, separation is required from range or velocity information as some identification frequencies are used jointly and do not uniquely identify a tag. If tag-based identification is still required, multiple combinations of consecutive $f_{\mathrm{id,x}}$ can be assigned to a single tag, uniquely identifying it and containing additional information. So can five identification frequencies in three stages supply $\binom{5+3-1}{3} = 35$ combinations, e.g., up to 35 tags or five information stages for seven tags.

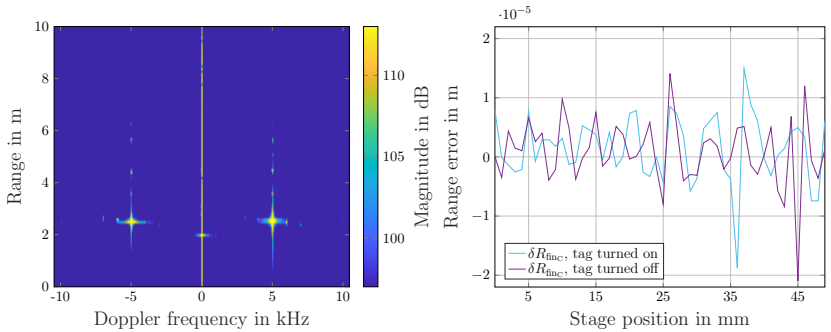

Figure 7.3: RDM (a) and range error (b) for measurements of a Doppler tag and a corner reflector next to each other. The tag is turned on and off for comparison of range errors toward the corner without changing the setup.

Simultaneous Tag and Object Monitoring

Doppler tags are ideal for crowded scenarios, where they uniquely identify (multiple) tagged objects and distinguish them from the surroundings. However, in some applications such as autonomous operation, surrounding obstacles should not just be suppressed but detected, monitored, and object to accurate signal processing for interaction or collision avoidance. Doppler tags tolerate detection and accurate $f\varphi$ estimation for untagged objects, one of the central distinguishing features from most radar tags. While the latter come with advantages in clearly defined tasks, Doppler tags work toward a holistic system.
For demonstration, a setup with the assembled Doppler tag (Fig. 6.1a) is complemented by a corner reflector next to the tag and range estimation is performed to both tag and corner, concurrently. The RDM for this setup is shown in Fig. 7.3a. As the corner is not centered in front of the radar, the angular shift is determined and considered during processing. Static targets are suppressed during Doppler tag processing, which is why range estimation for the tag is not impaired by the additional target. For the corner reflector, range errors with the tag turned on and off are contrasted in Fig. 7.3b with no deterioration discernible. Although the tag is a strong spurious target limiting the SINR, range accuracy is not restricted. Other effects such as multiple reflections and environmental influences

are dominant. The proposed signal processing chain is hence well-suited for simultaneous tagged and untagged object ranging.

7.2 Object Orientation Estimation

Orientation estimation determines the alignment of an object relative to a reference point or surface. It is hardly realized with radar and, where applied, mostly relys on radar-based angle of arrival (AoA) estimation [RSV15, DFV16] or information extraction from radar images, such as from high-resolution radars in [PG01, RKDW16, AFM+13]. Classification-aided estimation was also demonstrated with and without machine learning algorithms in [JLSV+23, SLY+21, KBK+15].
Alternatively, radar tags on each side of an object can be used to determine a coarse orientation estimation from the visibility of certain tags. Orientation angle estimation in two spatial directions, α_{az} and α_{el} in Fig. 7.4, is achieved using range information from two known reference points on one side of an object, e.g., Doppler tags. This estimation based on dual-point range estimation using simultaneously readable tags is newly demonstrated hereinafter. The approach is of paramount interest if the object is tagged for identification purposes and the same tags can be used for orientation estimation. Doppler tags are particularly suitable for this task as they allow for unique identification and accurate range estimation, enabling orientation estimation with decreased hardware and processing complexity compared to existing solutions. To determine α without spacial alignment of radar and object, the off-boresight angles at which the tags appear in front of the radar must be known, e.g., from AoA estimation. High angular resolution is required, particularly for small objects, to successfully separate the tag angles. However, if the radar is positioned volume-centered in front of the object, it is possible to estimate the orientation angles in azimuth (α_{az}) and elevation (α_{el}) without additional angular information. Angles are estimated separately, for orientation estimation with components in both angular directions azimuth and elevation, three tags in an L-shape are required for unambiguity. Roll angle estimation is not possible without fine angular resolution but can be obtained through pitch or yaw angle estimation using a different radar position.

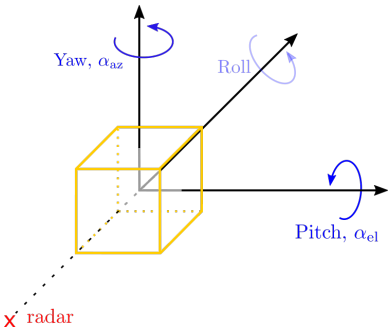

Figure 7.4: Orientation angle definition. Using Doppler tags, the two angles α_{az} and α_{el} can be estimated.

Orientation estimation is performed using the mRTS tags together with the AWR1843BOOST radar. Accurate absolute range estimation is essential to enable three-dimensional (3D) applications, hence requiring calibration. It accounts for systematic measurement errors, originating from signal propagation delays within the radar and Doppler tag hardware, as well as deviations caused by environmental influences. The calibration procedure utilizes the known positions of radar and tags to assign accurate ground truth ranges to each radar measurement. The discrepancy between measured and true ranges is evaluated throughout the entire measurement interval to identify a constant offset from hardware delays. This offset is determined and compensated individually for each tag in order to account for its specific delay. The temperature-dependent range drift (Ch. 3.1.1) is calibrated for each measurement. From the calibrated range information of multiple tags, the estimation of the orientation angle α is possible.

Azimuth orientation angle estimation is demonstrated in a volume-centered setup as delineated in Fig. 7.5a and shown pictorially in Fig. 7.5b. Two Doppler tags A and B are attached to diagonal corners of one side of a cuboid. The tag positions are chosen this way to have a baseline in both azimuth and elevation, so that the given calculation for the azimuth angle α_{az} can be directly transferred to elevation angles α_{el}. Given tags at a distance of d_1 in x-direction and d_3 in z-direction, α_{az} is derived from the range estimates R_A and R_B as detailed in A.2.
Good tag visibility is required for reliable range estimation. The orientation

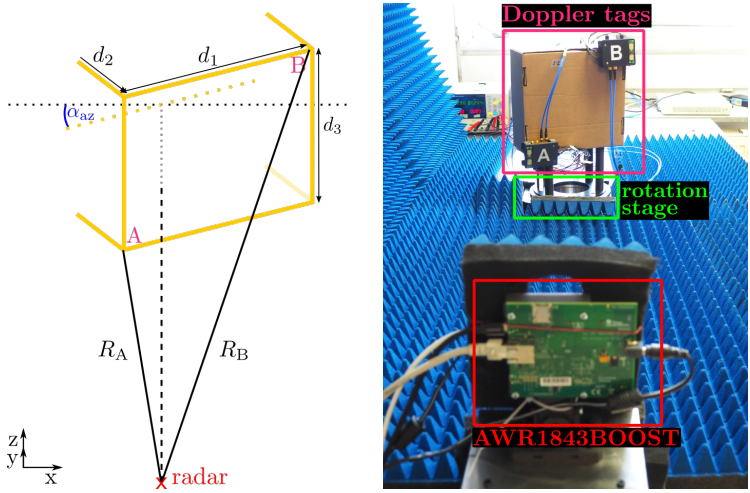

Figure 7.5: Orientation angle determination in azimuth using two Doppler tags A and B (a) and corresponding measurement scenario (b). The two tags are attached to diagonal corners of the object and reliably visible for $\alpha_{az} \in [-10°, 10°]$.

angles under which the tags are visible to the radar depend on the tag antenna opening angles and the overall setup. Increasing the range between radar and tags can compensate angle limitations; however, larger ranges would require active amplification in the tags for them to remain visible. If tags are visible but range estimation accuracy is low, e.g., due to poor SNR, orientation angle estimation deteriorates as errors directly transfer from range to angle according to

$$\delta\alpha_{az} \approx \frac{1}{d_1}(\delta R_B - \delta R_A). \tag{7.1}$$

Symmetric range errors occurring in both estimates R_A and R_B, e.g., from poor calibration, hardly affect the orientation estimation as they cancel out. Simulations show that these range errors lead to orientation errors two orders of magnitude smaller than equivalent asymmetric range errors, affecting only one estimate R_A or R_B, e.g. due to poor tag visibility. Errors in the tag placement, distorting d_1 and d_3, primary affect the orientation estimation if they occur in the direction in which the object is rotated off boresight, hence azimuth estimation is

sensitive to displacement in x-direction (d_1) and elevation estimation is sensitive to displacement in z-direction (d_3). The object dimension in y-direction (d_2) is required for orientation estimation according to A.2, however, has a minor influence on estimation errors.
At least two tags are required to determine an orientation angle, but calculations are conducted mostly using the information of one tag (tag A in A.2). Errors in the range estimation of this tag have a slightly stronger impact on the estimation results than those of the second tag. If known, the tag allowing for a more accurate range estimation should thus be primarily used in calculations.

For the evaluation of the proposed orientation estimation, the setup in Fig. 7.5b provides ground truth to quantify the estimation accuracy. A perforated metal plate with a uniform grid of holes at precisely determined x-y-coordinates serves as the reference platform. To minimize multipath interference and strong spurious reflections, it is covered with absorber material. The radar is placed at a fixed position on this plate, volume-centered in front of the rotating object. The holes of the plate establish the radar position in x- and y-direction while the height is manually determined. The object is mounted on the rotation stage (Ch. 3.2.4), also positioned on the perforated plate, and the tags are attached to the object exactly above the holes of the plate, defining their initial positions in all three dimensions. Two Doppler tags A and B with $f_{\mathrm{id,A}} = 3\,\mathrm{kHz}$ and $f_{\mathrm{id,B}} = 6\,\mathrm{kHz}$ are used with tag A being mainly utilized for orientation angle calculations. The major error source in this setup is the tag placement on the object above the plate holes in a certain height. However, most occurring errors are symmetrical and only have limited implications on the overall estimation accuracy.
The rotation stage provides the angular steps and serves as a reference system to validate the estimated orientation angle. It is rotated from $-10°$ to $10°$ in steps of $1°$. For each step, R_{A} and R_{B} are measured to determine $\widehat{\alpha}_{\mathrm{az}}$. Rotation up to $\pm 10°$ provides clear visibility for both tags. Beyond, reliable range estimation is not possible anymore due to the narrow antenna opening angle of the mRTS tags. Continuous angle estimation for an object during a full rotation is thus not possible with the available hardware. Wider opening angles would be required so that, equipping all sides of the cuboid with tags, at least two tags are continuously visible. In the special case of an orientation angle of 45°, two tags mounted on different sides of the object are detected. Due to the unique identification capability of the tags, this case can be differentiated from two tags on one side. The calculation has to be adjusted accordingly as

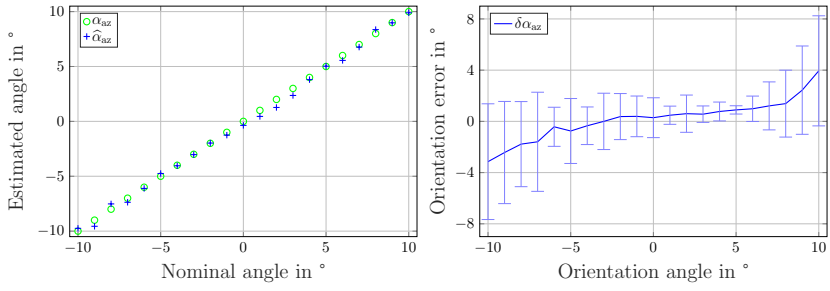

(a) (b)

Figure 7.6: Good agreement of nominal and estimated angles for $\alpha_{az} \in [-10°, 10°]$ is reached in some measurements (a), however, mean error and standard deviation (b) are generally larger and deteriorate with increasing angles, mainly due to poor tag visibility.

the distances between the tags differ from d_1 and d_3, but $R_A = R_C$ for two visible tags A and C on two sides of the cuboid can be utilized as additional information. For orientation angles close to but not exactly 45°, $R_A = R_C$ is not valid and orientation estimation is insensitive. A sufficient opening angle of tags providing visibility of a third tag is therefore recommended, allowing for regular calculations also near $\alpha = 45°$.

Estimated orientation angles in Fig. 7.6 are in good agreement with the true orientations and a root MSE (RMSE) of 0.4° is achieved over the depicted measurement series. However, variations up to a few degrees occur as shown in Fig. 7.6b for the mean error and standard deviation of 100 measurement iterations. For larger orientation angles, error and variance increase alike. This stems from a deteriorated visibility of tags for increased rotation, coming with lower SNR and, hence, larger variance. The variance is not symmetric, primarily due to deviant tag performance. Tag B is visible only up to 13°, whereas tag A remains visible up to −20°. The SNR for tag B hence degrades earlier and stronger as the angle increases. As a result, positive orientation angles, where tag B is rotated away from the radar, are estimated with larger errors, however, slightly lower variation. Large antenna opening angles, ensuring good tag visibility, are thus essential for reliable orientation estimation and a crucial design parameter for application-tailored tag hardware.
Additionally, multiplicative errors in the range estimates R_A and R_B or in d_1 influence the results. Possible reasons are the discussed limitations in the

hardware, measurement setup, and calibration, but also drifts in the radar parameters. An additive error in range estimation would result in a constant offset in α, which is hardly observed.

While the required radar calibration can be practically achieved and is not dependent on the surroundings, realizing a volume-centered setup is challenging and prone to movement. The implementation is mostly realistic in scenarios with limited degrees of freedom, such as objects on a conveyor belt, or supported with additional AoA estimation. Radar-based orientation estimation hence requires careful system design, but is an ambitious advancement in spatial awareness from radar data.

7.3 Self-Positioning

Positioning is a well-established radar application, covering both external and self-positioning [VWG+03] in various contexts and implementations [MKV11, SDCV18, DDG+18, SIR24, BASP+24]. It provides the data basis for autonomous systems with a particular emphasis on indoor applications, although not being limited to those. High accuracy can be achieved, particularly if phase information is exploited [VRH99].
Radar-based approaches offer an alternative to other wireless technologies, with the use of Doppler tags being presented as a new option. Self-positioning demonstrated hereinafter is based on trilateration according to [Ble00, SDM14]. The tags serve as reference stations, requiring unique distinction, accurate range estimation, and visibility from a distance to ensure reliable positioning. While the first two points are inherent features of Doppler tags, their range is limited with the current hardware, restricting possible setups. However, tailored tag design can overcome this limitation.
The radar position $\mathbf{p}_\mathrm{r} \in \mathbb{R}^3$ is unknown and determined by measuring ranges $R_i = \|\mathbf{p}_\mathrm{r} - \mathbf{p}_i\|$ to the tags as reference points $\mathbf{p}_i$. Each range measurement defines a sphere around $\mathbf{p}_i$ with radius R_i. In an ideal, noise-free scenario, trilateration determines the unknown spatial coordinates as the unique intersection point of at least four non-coplanar spheres, i.e., which are in no common plane. In practice, however, range estimations $\widehat{R}_i$ are subject to measurement uncertainties $\widehat{R}_i = R_i + \varepsilon_i$, where $\varepsilon_i \sim \mathcal{N}(0, \sigma_{\varepsilon_i}^2)$ after successful calibration. The geometric intersection problem is hence transformed into an optimization

task with the estimated position $\widehat{\mathbf{p}}_\mathrm{r}$ minimizing the squared differences between measured and ideal ranges to all N reference points as

$$\widehat{\mathbf{p}}_\mathrm{r} = \arg\min_{\mathbf{p}_\mathrm{r}} \sum_{i=1}^{N} \left(\widehat{R}_i - \|\mathbf{p}_\mathrm{r} - \mathbf{p}_i\|\right)^2. \tag{7.2}$$

The position error $\delta\mathbf{p}_\mathrm{r} = \widehat{\mathbf{p}}_\mathrm{r} - \mathbf{p}_\mathrm{r}$ is affected by the error of each range measurement as well as the geometrical configuration of the reference points. The relation between the position error $\delta\mathbf{p}_\mathrm{r}$ and the range error $\delta\mathbf{R}$ is described by a range vector $\mathbf{R}(\mathbf{p}_\mathrm{r})$ that contains all range measurements for one position, with $\delta\mathbf{R} = \mathbf{R}(\widehat{\mathbf{p}}_\mathrm{r}) - \mathbf{R}(\mathbf{p}_\mathrm{r})$. This range vector specifies the nonlinear relation between range and position but, for small deviations from the true position, can be linearized using a first-order Taylor expansion, resulting in $\delta\mathbf{R} = \mathbf{J}\delta\mathbf{p}_\mathrm{r}$ with the Jacobian matrix $\mathbf{J}$ and its rows $\mathbf{J}_i = \frac{(\mathbf{p}_\mathrm{r}-\mathbf{p}_i)^T}{\|\mathbf{p}_\mathrm{r}-\mathbf{p}_i\|}$. Solving for the position error using the Moore-Penrose pseudoinverse allows to describe the propagation from range errors to position errors with

$$\delta\mathbf{p}_\mathrm{r} = \left(\mathbf{J}^\mathrm{T}\mathbf{J}\right)^{-1}\mathbf{J}^\mathrm{T}\,\delta\mathbf{R}. \tag{7.3}$$

The term $\left(\mathbf{J}^\mathrm{T}\mathbf{J}\right)^{-1}$ is the dilution of precision (DOP), quantifying how spatial reference point constellations affect error propagation. Under the assumption of equally distributed and uncorrelated measurement noise, it can be interpreted as a covariance-like matrix, in 3D yielding

$$\mathbf{C}_\mathrm{DOP} = \left(\mathbf{J}^\mathrm{T}\mathbf{J}\right)^{-1} = \begin{bmatrix} \mathrm{DOP_x}^2 & \cdot & \cdot \\ \cdot & \mathrm{DOP_y}^2 & \cdot \\ \cdot & \cdot & \mathrm{DOP_z}^2 \end{bmatrix}. \tag{7.4}$$

The diagonal elements correspond to the geometric contributions to the error variance in each spatial dimension, often summarized into scalar indicators $\mathrm{HDOP} = \sqrt{\mathrm{DOP_x}^2 + \mathrm{DOP_y}^2}$ (horizontal) and $\mathrm{VDOP} = \sqrt{\mathrm{DOP_z}^2}$ (vertical). DOP values start from one, whereat smaller values indicate higher accuracies, i.e., one is optimal, five is still acceptable, and values in excess of 10 hardly allow meaningful evaluation.

In realistic scenarios, equal measurement uncertainty is not granted, e.g., due to a varying SNR or different angles of reception. Under these conditions, the

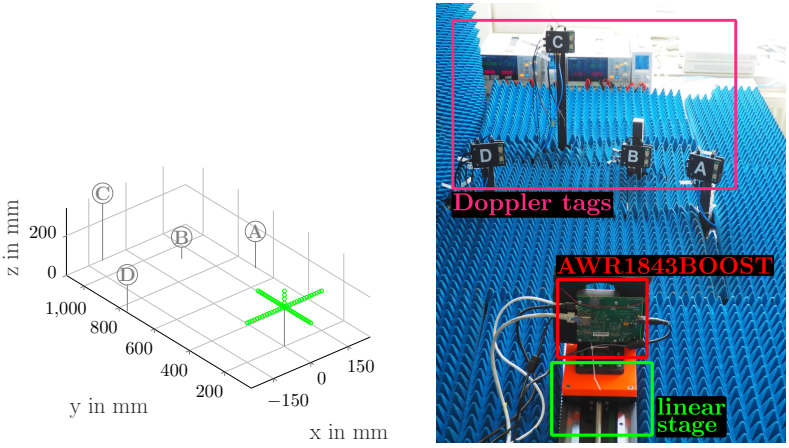

(a) (b)

Figure 7.7: Positioning scenario schematically (a) and picturally (b). Ground truth radar positions are depicted in x-, y-, and z-direction. The positions of the reference tags A to D result in a DOP of 5.5 (HDOP = 1.8, VDOP = 5.2) for the radar in the star center point.

DOP formulation can be extended by incorporating the covariance matrix $\mathbf{C}_\mathrm{R}$ of the range measurements, resulting in the positioning CRLB (PCRLB)

$$\mathbf{C}_\mathrm{CRLB} = \left(\mathbf{J}^\mathrm{T}\mathbf{C}_\mathrm{R}^{-1}\mathbf{J}\right)^{-1}. \tag{7.5}$$

The diagonal elements of $\mathbf{C}_\mathrm{CRLB}$ correspond to the minimum achievable variance of position estimation in each spatial dimension, considering both measurement uncertainties and the geometric constellation of reference points. Just as the CRLB, DOP and PCRLB rely on several simplifying assumptions, including unbiased range estimation and uncorrelated AWGN, hence being idealized lower bounds that provide geometric and qualitative insight rather than realistic performance limits. Even after calibration, small residual offsets persist due to limited reference accuracy and drifts of radar parameters and, as all tags are evaluated within the same radar frame, partial correlation of measurement noise cannot be avoided, particularly in multipath-rich environments.

Optimal tag placement hence minimizes DOP and expected measurement errors, but practical considerations are limiting. Minimizing the DOP favors

Table 7.1: Tag and radar coordinates for the measurement setup in Fig. 7.7.

	A	B	C	D
x	236	97	-97	-236
y	696	920	1096	760
z	185	110	340	185

(a) Tag coordinates in mm.

	$\mathbf{p}_{r,x}$	$\mathbf{p}_{r,y}$	$\mathbf{p}_{r,z}$
x	-150...150	0	0
y	200	49...349	200
z	200	200	200...280

(b) Radar coordinates in mm.

placing the stations far apart from each other while minimizing the measurement error, determined mostly by the SNR, requires close positioning centrally within the radar FoV to maximize antenna gain and reduce free-space loss. Both conditions cannot be met simultaneously, requiring a compromise for the setup that ensures good visibility of all tags in all radar positions together with adequate DOP. The resulting measurement setup is shown in Fig. 7.7 and coordinates are given in Table 7.1. The tags are mounted at short distance to the radar and at a shallow angle to ensure sufficient SNR for reliable tag detection despite missing amplification and limited opening angles. This setup is far from realistic scenarios, but suitable to demonstrate positioning with the mRTS tags. Radar displacement in x- and y-direction is realized using the M-414 linear stage (Ch. 3.2.2), moving the radar to 31 positions along the x- and the y-axis in steps of 10 mm, respectively. In z-direction, the radar is positioned using stackable spacers of 20 mm height. The positions resemble a star-shaped path, referred to as positioning star hereinafter.

At each point of the star, the radar position is estimated using trilateration and compared to the ground truth position for accuracy quantization. The same perforated metal plate used as a reference for orientation estimation allows for position referencing. Four tags, enumerated A to D, and the linear stage are mounted at defined positions on the plate. The tags are attached to vertical rods at certain heights above the holes of the plate, while mounting brackets align the linear stage to those. This defines the reference points and the center of the positioning star. In all other radar positions, x and y coordinates are determined from the movement of the linear stage, and the z coordinates are known from the height of the spacers that lift it. During assembly, tilts or misalignments occur and introduce uncertainties to the reference, which cannot be exactly quantized but are estimated to be in sub-millimetre to millimetre range, which is not truly sufficient to reference a system with mm accuracy, but accepted for demonstra-

tion purpose. Calibration for each tag is performed as detailed in Ch. 7.2 and also contains imperfections, jointly limiting the achievable estimation accuracy. The used identification frequencies $f_{\mathrm{id,x}}$ are chosen to provide adequate frequency spacing between tags and from zero Doppler, resulting in

$$f_{\mathrm{id,A}} = 3\,\mathrm{kHz},\ f_{\mathrm{id,B}} = 6\,\mathrm{kHz},\ f_{\mathrm{id,C}} = 9\,\mathrm{kHz},\ f_{\mathrm{id,D}} = 12\,\mathrm{kHz}. \tag{7.6}$$

Using trilateration and a nonlinear least-squares solver, 3D positioning is possible solely from the ranging information of four tags. However, due to limitations in tag visibility, the achievable DOP values are weak, particularly VDOP. This is caused by both the radar and tag FoVs, which are particularly small in elevation, hence reducing the position accuracy in z-direction. To address this limitation and demonstrate the potential of the radar-tag system for positioning, the estimated z-coordinates are manually constrained during optimization to remain close to the average z-coordinate of the tags when determining positions for the x- and y-direction movements. For the z movement, no such constraint is applied as the z-coordinate is iteratively changed. Consequently, processing for the x-y-plane and the z-direction is slightly different, preventing a direct comparison, but with minor influences on the overall conclusion.

For quantization of the results in 3D, the position RMSE is defined as

$$\mathrm{RMSE_{3D}} = \frac{1}{3}\left(\overline{\mathrm{RMSE_x}} + \overline{\mathrm{RMSE_y}} + \overline{\mathrm{RMSE_z}}\right) \tag{7.7}$$

and

$$\mathrm{RMSE}_{\mathrm{x},n} = \frac{1}{\sqrt{3}}\|\mathbf{p}_{\mathrm{r}_{\mathrm{x},n}} - \widehat{\mathbf{p}}_{\mathrm{r}_{\mathrm{x},n}}\|, \tag{7.8}$$

where $\mathrm{RMSE}_{\mathrm{x},n}$ denotes the RMSE of the position estimate $\widehat{\mathbf{p}}_{\mathrm{r}_{\mathrm{x},n}}$ for the n-th point on the x-ray of the positioning star and analogous definitions apply for $\mathrm{RMSE}_{\mathrm{y},n}$ and $\mathrm{RMSE}_{\mathrm{z},n}$. n counts through the 31 measurement steps in x- and y-direction and the five measurement steps in z-direction, respectively.
Figure 7.8a contains positioning results in all three spatial directions, which are in good agreement with ground truth. An overall RMSE for the full positioning star of $\mathrm{RMSE_{3D}} = 3.5\,\mathrm{mm}$ is achieved. The RMSE values for the three measurement directions according to (7.8) are contrasted in Fig. 7.8b. The center of the positioning star is measured thrice, however, after modification of the setup for measurements in x-, y-, and z-direction. The deviations in this point therefore mainly provide information about the setup reproducibility and rate

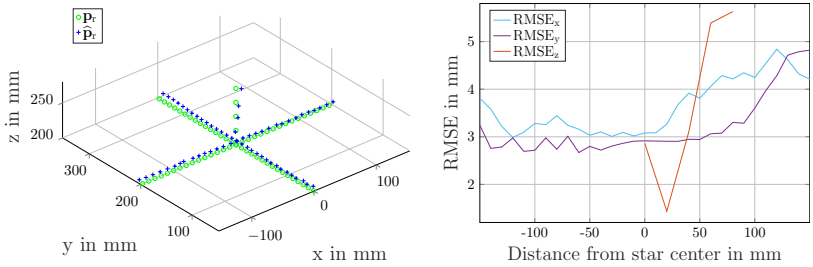

Figure 7.8: Estimated positions (a) and RMSE (b) for 3D measurements of 31 steps (step size 10 mm) in x- and y-direction and five steps (step size 20 mm) in z-direction. Results are in good agreement with ground truth positions, however, the sensitivity to tag visibility and SNR is apparent, resulting in larger errors in the outer star positions.

the reference system. Systematic deviations from ground truth positions at other points are likely due to imperfect calibration and unaccounted drifts in radar parameters. For the outer x positions, errors increase due to poorer DOP and tag visibility. This influence is more pronounced at positive x values due to the asymmetric tag constellation in x-direction. At close y positions, the tags are observed under steeper angles, which in combination with the given opening angles results in reduced SNR and higher RMSE. For large z-positions, the RMSE increases most due to the poor visibility of tag B and reduced visibility of tags A and D. The variance of repeated measurements is also higher with increasing z, caused by the worse VDOP in comparison to the HDOP. Additionally, the radar positions in z-direction were not reached using the linear stage but manually with 3D-printed spacers. Ground truth positions are consequently less accurate and less reproducible. The lowest RMSE is reached near the center of the measurement star, at a slightly elevated z-position. In this radar position, the tag heights are best balanced relative to the radar, ensuring good visibility of all tags. However, an offset of a few millimeters remains.

Positioning with Doppler tags is possible but sensitive to proper tag visibility and DOP. The DOP in Fig. 7.7 is given for the radar in the star center and only slightly changes for the outer positions. The visibility of tags varies to a greater extent and is the dominant factor for successful positioning. DOP is less pronounced but still essential to achieve robust results. With intentionally poor DOP, positioning is significantly deteriorated as exemplified in Fig. 7.9b for the

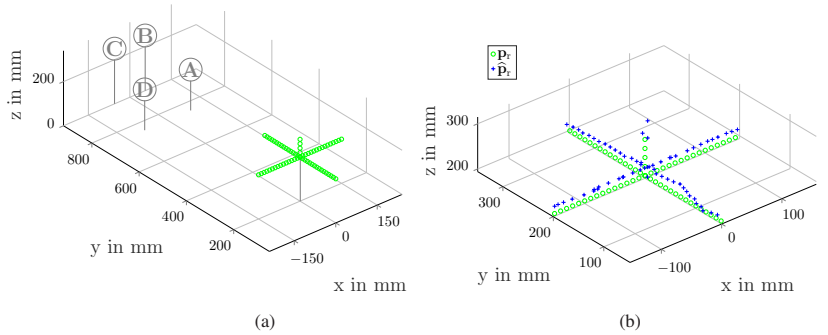

Figure 7.9: Measurement scenario with poor DOP (a) and corresponding positioning results (b). The tag positions result in a DOP of 11.3 (HDOP = 4.3, VDOP = 10.5) for the radar in the star center point and positioning results are thereupon clearly deteriorated in comparison to Fig. 7.8a.

measurement setup of Fig. 7.9a. Although tag visibility improves, the RMSE increases by a factor of 3 to 4 from 3.5 to 12.4 mm, substantiating the relevance of DOP for positioning.

To unambiguously determine a position in 3D, four reference points are required; using only three would result in two possible solutions. However, knowledge of the radar FoV and physically possible positions mostly leaves only one of them reasonable, so that a position estimate can be found with three tags. A similar kind of preknowledge is utilized in positioning with the global navigation satellite system (GNSS), where the signal of the fourth satellite is used for clock error correction that enhances position estimation. Similarly, the fourth tag can be used to correct an offset in the range estimation to the four tags that might remain after calibration. However, only a radar offset is addressed, different propagation delays of the tags cannot be corrected and the radar, corresponding to the GNSS base station, tends to be more accurate than the tags, corresponding to satellites. This is a major drawback compared to GNSS, where deviations in the less accurate system part, the base station, are addressed. The correction approach is hence less beneficial as it is for GNSS, and positioning results were found to barely improve. If calibration is omitted, offset correction can enhance positioning results, however, the results are not as good as those from a well-calibrated system. Thus, if calibration is applicable, it is preferred with the proposed offset correction being a fallback solution in case of missing or

insufficient calibration possibilities. If, however, tag positioning using multiple radars is targeted, this approach deserves reassessment.

Self-positioning using Doppler tags features promising results competitive to other indoor positioning approaches. Given tailored tag hardware, further improvement in the estimation accuracy is expected. The benefit of Doppler tags for positioning is mainly in the concomitant completion of multiple tasks so that one hardware concept serves most information requirements at once.

Doppler-tag operation was demonstrated in common industrial scenarios, including tiered information transmission, operation within boxes, and next to strong interfering reflections. The introduced orientation estimation is the first tag-based approach demonstrated for radar and takes full advantage of the highly accurate range estimation toward Doppler tags. Just as self-positioning, it features promising results, despite challenges introduced by the available tag hardware, primary in visibility. While this proves the functionality in a proof-of-concept setup, tailored tag hardware is required to put the Doppler tags into practice and will significantly enhance position and orientation estimation. Thereby, the applicability of radar-tag systems can be extended toward a holistic system, delivering a multiplicity of information contributing to spatial awareness.

8 Conclusion

From pinpoint ranges to decisive insights, this work scrutinizes the potential of highly accurate range estimation and its integration into the innovative concept of Doppler tags.
Industrial automation is on the rise and autonomous systems require increasing amounts of data about their vicinity and the objects they are intended to work with. Radar sensors can deliver ambient information in dynamic scenarios and their scope of function can be further extended to identification using tags. Particularly systems relying on artificial intelligence can benefit from a tagged environment on which they can continuously learn, while basic behavior can be taught even from simulations. Doppler tags are a promising option, explicitly when range estimation with pinpoint accuracy despite unique tag identification is required. Possible applications range from low-level supervision to autonomous guiding tasks and exploit the benefits of Doppler tags and accurate ranging to different extents.
Revisiting the central findings provides a comprehensive overview of the work at hand. The idea of ranging from phase-offset information was introduced for FMCW and is extended to be applicable with CS. It is combined with Doppler tags that emulate the Doppler phenomenon with uniquely assignable frequencies, allowing for identification of tagged objects. A radar-tag system thereby pictures its environment with identifiable tag markers and general sensing information about the untagged remainder. For tagged and untagged objects, highly accurate range estimation is available, whereat the achievable accuracy toward tags can even exceed that toward an equidistant untagged object. Beyond, classical radar sensing provides information on object properties such as relative velocity or angle, hence delivering further environmental insights without tag interference. Unmodified radar hardware allows for this concomitant sensing and simultaneously reduces equipment acquisition and complexity. Doppler tags function reliably in a variety of scenarios, whether there are multiple tags, strong passive targets, or dynamic conditions. They are sensed simultaneously, avoiding blind times and the requirement for exceptionally high measuring

rates. Finally, different radar schemes are capable of operating with Doppler tags, incorporating distinct benefits in various applications. These insights collectively reveal the versatile adaptability of Doppler tags with accurate ranging and carve out challenges and limitations regarding specification, design, and signal processing. Therefore, this work functions as a fundamental applicability study, forming the basis for application-oriented and application-tailored developments.

In this context, the central contributions of the work at hand are presented from the idea over its implementation to verification in hardware, highlighting the achievements in comparison to the current state of research.

Highly accurate range estimation is a prerequisite of various radar-related sensing tasks. The novel $f\varphi$ estimation algorithm enables µm accuracy solely in signal processing without challenging hardware demands. The work at hand initially derives the signal model required to isolate the phase offset in CS and utilize it for range estimation, achieving range errors of 4.8 µm in static scenarios with moderate bandwidths below 4 GHz. The newly developed Doppler correction algorithm significantly improves range estimation for targets in motion to range errors as small as 2.3 µm. Counterintuitively, this algorithm enables even higher range estimation accuracy for moving targets than for static ones due to an effective suppression of static influences. Accompanying velocity estimation achieves errors of 1.4 mm/s at 1 m/s. The results align well with findings from simulations, granting in-depth comprehension, and verify those as a valuable research tool for future system specification and impact analysis.

The **concept of Doppler tags**, extending radar functionality to unique object identification, is introduced for the first time from the idea over first hardware implementations to extensive signal processing. Original algorithms and signal processing chains for object separation and identification allow for improved tag sensing by clutter suppression and concomitant sensing of untagged surroundings, both with unmodified radar hardware. The presented radar-Doppler-tag system thereby overcomes previous limitations and enables unprecedented combinations of functions in the field of radar-based automation. The work offers guidance for an application-specific system design essential in further research and industrial implementation. The resulting sensing information indicates promising features of the new concept and bears potential for sophisticated processing approaches.

Of particular interest is **tag ranging** and the link between object identification and highly accurate range estimation toward this object. The integration of $f\varphi$ range estimation into the processing chain of Doppler tags is achieved by algorithmic elimination of all tag impacts preserving phase-offset information. The residual object-determined signal share is not only undisturbed of prior tag functionality, but contains enhanced resolution and SINR. Particularly high and challenging bandwidths are not required for target separation, enabled by Doppler tags, and accurate range estimation, obtained from $f\varphi$ analysis. Consequently, this work originally demonstrates high accuracy in range estimation toward Doppler tags without demanding hardware requirements. Range errors below 9 µm for static and 8 µm for moving tags are achieved with bandwidths below 4 GHz, accompanied by identification errors of a few Hertz depending on the applied frequency, and velocity errors around 1 mm/s. The results enhance existing and open up new areas of application, foremost in the context of automation, but also beyond.

Evaluation of **Doppler tag applicability** highlights practical relevance and supports implementation. New systems are particularly expedient if they enable a variety of applications at once. Combining the previous achievements allows for a utilization of Doppler tags in a number of practical applications in and beyond the scope of classical radar sensing. Exemplarily, for indoor positioning, they are a competitive concept reaching an average RMSE of 3.5 mm in a $300 \times 300 \times 80\,\mathrm{mm}^3$ frame. Orientation estimation from dual-point range estimation is newly developed in the work at hand and expands the scope of radar functionalities with additionally extracted information without supplementary hardware or evaluation instances. Angular errors of 0.4° over ±10° rotation are realized. While results are impacted by hardware and referencing limitations, they are still remarkable and greatly verify the practical value of Doppler tags in advanced radar operation.

In summary, Doppler tags with highly accurate ranging are a precious extension of radar functionality with versatile application possibilities. They unlock hidden potential in the simultaneous execution of classical sensing and sophisticated autonomous tasks. With this work, the technical foundations of the novel concept are established, paving the way for future developments.

A Addendum

A.1 Scenario-aware CRLB Derivations

Detailed derivations of the CRLB using different sets of assumptions are given.

A.1.1 Classical CRLB

The classical CRLB is derived according to [Kay93], assuming a single complex sine wave superimposed by AWGN and an unbiased estimator.

Consider the discretized data model in accordance to (4.6)

$$s[n] = A\exp\big(\, j(2\pi\tilde{f}_{\mathrm{b}}n + \varphi_{\mathrm{b}})\big) + \omega[n], n \in [0, N_{\mathrm{s}} - 1], \tag{A.1}$$

where A denotes the amplitude of the signal, $\tilde{f}_{\mathrm{b}}$ the sampled beat frequency, φ_{b} the beat phase, N_{s} the number of samples, and $\omega[n]$ a complex WGN process with variance σ^2. The parameter vector $\boldsymbol{\theta}$ contains the parameters to be estimated

$$\boldsymbol{\theta} = [A\ \tilde{f}_{\mathrm{b}}\ \varphi_{\mathrm{b}}]^T, \tag{A.2}$$

with their variances

$$\mathrm{var}(\widehat{\boldsymbol{\theta}_{\mathrm{i}}}) \geq \left[\mathbf{I}_{\mathrm{F}}^{-1}(\boldsymbol{\theta})\right]_{\mathrm{ii}}. \tag{A.3}$$

The Fisher information matrix for the proposed signal model is

$$\begin{aligned}\left[\mathbf{I}_{\mathrm{F}}(\boldsymbol{\theta})\right]_{\mathrm{ij}} = tr\left[\boldsymbol{C}^{-1}(\boldsymbol{\theta})\frac{\delta\boldsymbol{C}(\boldsymbol{\theta})}{\delta\boldsymbol{\theta}_{\mathrm{i}}}\boldsymbol{C}^{-1}(\boldsymbol{\theta})\frac{\delta\boldsymbol{C}(\boldsymbol{\theta})}{\delta\boldsymbol{\theta}_{\mathrm{j}}}\right] \\ + 2\Re\left[\frac{\delta\boldsymbol{\mu}^H(\boldsymbol{\theta})}{\delta\boldsymbol{\theta}_{\mathrm{i}}}\boldsymbol{C}^{-1}(\boldsymbol{\theta})\frac{\delta\boldsymbol{\mu}(\boldsymbol{\theta})}{\delta\boldsymbol{\theta}_{\mathrm{j}}}\right],\end{aligned} \tag{A.4}$$

where $\boldsymbol{C}$ denotes the covariance matrix, $\boldsymbol{\mu}$ the mean vector, and $\Re$ the real part of a complex number. The first term vanishes as $\boldsymbol{C}(\boldsymbol{\theta}) = \sigma^2\mathbf{I}$, with $\mathbf{I}$ being the identity matrix, is not dependent on $\boldsymbol{\theta}$, hence

$$\begin{aligned}[\mathbf{I}_\mathrm{F}(\boldsymbol{\theta})]_{\mathrm{ij}} &= 2\Re\left[\frac{\delta\boldsymbol{\mu}^H(\boldsymbol{\theta})}{\delta\boldsymbol{\theta}_\mathrm{i}}\boldsymbol{C}^{-1}(\boldsymbol{\theta})\frac{\delta\boldsymbol{\mu}(\boldsymbol{\theta})}{\delta\boldsymbol{\theta}_\mathrm{j}}\right] \\ &= \frac{2}{\sigma^2}\Re\left[\sum_{n=0}^{N_\mathrm{s}-1}\frac{\delta s^*[n]}{\delta\boldsymbol{\theta}_\mathrm{i}}\frac{\delta s[n]}{\delta\boldsymbol{\theta}_\mathrm{j}}\right]\end{aligned} \tag{A.5}$$

and

$$\begin{aligned}\mathbf{I}_\mathrm{F}(\boldsymbol{\theta}) &= \frac{2}{\sigma^2}\begin{bmatrix} N_\mathrm{s} & 0 & 0 \\ 0 & (2\pi A)^2\sum_{n=0}^{N_\mathrm{s}-1} n^2 & 2\pi A^2\sum_{n=0}^{N_\mathrm{s}-1} n \\ 0 & 2\pi A^2\sum_{n=0}^{N_\mathrm{s}-1} n & A^2 N_\mathrm{s} \end{bmatrix} \\ &= \frac{2}{\sigma^2}\begin{bmatrix} N_\mathrm{s} & 0 & 0 \\ 0 & (2\pi A)^2\frac{(N_\mathrm{s}-1)N_\mathrm{s}(2N_\mathrm{s}-1)}{6} & 2\pi A^2\frac{N_\mathrm{s}(N_\mathrm{s}-1)}{2} \\ 0 & 2\pi A^2\frac{N_\mathrm{s}(N_\mathrm{s}-1)}{2} & A^2 N_\mathrm{s} \end{bmatrix}.\end{aligned} \tag{A.6}$$

From the inversion of this matrix, the lower bounds are derived according to (A.3) and considering the SNR definition for a complex signal

$$\mathrm{SNR}\,\eta = \frac{\left(2\frac{A}{\sqrt{2}}\right)^2}{2\sigma^2} = \frac{A^2}{\sigma^2}. \tag{A.7}$$

$$\begin{aligned}\mathrm{var}(\widehat{A}) &\geq \frac{\sigma^2}{2N_\mathrm{s}} \\ \mathrm{var}(\widehat{f_\mathrm{b}}) &\geq \frac{6}{(2\pi)^2\eta N_\mathrm{s}(N_\mathrm{s}^2-1)} \\ \mathrm{var}(\widehat{\varphi_\mathrm{b}}) &\geq \frac{2N_\mathrm{s}-1}{\eta N_\mathrm{s}(N_\mathrm{s}+1)}\end{aligned} \tag{A.8}$$

These are the lower bounds for the parameters directly estimated from (A.1), although of interest are the lower bounds for the range estimation done from f_b and φ_b. These can be determined through a transformation of parameters for an unbiased estimator and a sufficiently large N_s:

$$\mathrm{var}(\widehat{g}(\boldsymbol{\theta})) \geq \left(\frac{\delta g(\boldsymbol{\theta})}{\delta \boldsymbol{\theta}}\right)^2 I_\mathrm{F}^{-1}(\boldsymbol{\theta}) = \left(\frac{\delta g(\boldsymbol{\theta})}{\delta \boldsymbol{\theta}}\right)^2 \mathrm{var}(\widehat{\boldsymbol{\theta}}) \tag{A.9}$$

A range estimate can be derived from the sampled frequency $\tilde{f}_\mathrm{b} = \frac{f_\mathrm{b}}{f_\mathrm{s}}$

$$R_\mathrm{f} = \frac{cT}{2B} \cdot f_\mathrm{b} = \frac{cN_\mathrm{s}}{2B} \cdot \frac{f_\mathrm{b}}{f_\mathrm{s}} \tag{A.10}$$

with

$$\begin{aligned} \mathrm{var}(R_\mathrm{f}) &\geq \frac{c^2 N_\mathrm{s}^2}{4B^2} \cdot \frac{6}{(2\pi)^2 \eta N_\mathrm{s}(N_\mathrm{s}^2-1)} \\ &= \frac{3c^2 N_\mathrm{s}}{8\pi^2 B^2 \eta (N_\mathrm{s}^2-1)} \approx \frac{3c^2}{8\pi^2 B^2 \eta N_\mathrm{s}}. \end{aligned} \tag{A.11}$$

Alternatively, range estimation is possible from the phase $\widehat{\varphi}_\mathrm{b}$

$$R_\varphi = \frac{T}{2B} c f_\mathrm{min} - \sqrt{\left(\frac{T}{2B} c f_\mathrm{min}\right)^2 - \frac{T}{4B} c^2 \frac{\varphi_\mathrm{b}}{\pi}}, \tag{A.12}$$

resulting in

$$\begin{aligned} \mathrm{var}(R_\varphi) &\geq \frac{c^2 T}{16\pi^2 B \left(\frac{T}{B} f_\mathrm{min}^2 - \frac{\varphi_\mathrm{b}}{\pi}\right)} \cdot \frac{2N_\mathrm{s}-1}{\eta N_\mathrm{s}(N_\mathrm{s}+1)} \\ &= \frac{c^2 T (2N_\mathrm{s}-1)}{16\pi^2 B \eta N_\mathrm{s}(N_\mathrm{s}+1)} \frac{1}{\frac{T}{B} f_\mathrm{min}^2 - f_\mathrm{min} \frac{4R}{c} + \frac{B}{T}\left(\frac{2R}{c}\right)^2} \\ &\approx \frac{c^2 T}{8\pi^2 B \eta N_\mathrm{s}} \frac{1}{\frac{T}{B} f_\mathrm{min}^2 - f_\mathrm{min} \frac{4R}{c} + \frac{B}{T}\left(\frac{2R}{c}\right)^2}. \end{aligned} \tag{A.13}$$

By approximation, the quadratic share of the phase offset can be neglected ($f_{\min} \gg \frac{B}{2T}\frac{2R}{c}$), hence

$$\begin{aligned} \operatorname{var}(R_\varphi) &\geq \frac{c^2}{(4\pi)^2 f_{\min}^2} \cdot \frac{2N_\mathrm{s} - 1}{\eta N_\mathrm{s}(N_\mathrm{s} + 1)} \\ &\approx \frac{c^2}{8\pi^2 f_{\min}^2 \eta N_\mathrm{s}}, \end{aligned} \tag{A.14}$$

equaling the CRLB for range estimation from the phase offset in FMCW.

A.1.2 CRLB for Multiple Targets

To include a second target in the CRLB derivation, the data model is adjusted

$$\begin{aligned} s[n] =& A_1 \exp\big(j(2\pi \tilde{f}_{\mathrm{b},1} n + \varphi_{\mathrm{b},1})\big) + A_2 \exp\big(j(2\pi \tilde{f}_{\mathrm{b},2} n + \varphi_{\mathrm{b},2})\big) + \omega[n], \\ & n \in [0, N_\mathrm{s} - 1]. \end{aligned} \tag{A.15}$$

Additional terms can be used to model more targets, depending on the relevant number of targets for the considered scenario. The first multiple reflection can be interpreted as an additional target with $f_{\mathrm{b},2} = 2 \cdot f_{\mathrm{b},1}$, but $\varphi_{\mathrm{b},1} \neq 2 \cdot \varphi_{\mathrm{b},2}$ as the latter dependency is not linear. The further derivation is in accordance to A.1.1.

For the two-target scenario, the parameter vector is

$$\boldsymbol{\theta} = [A_1 \ \tilde{f}_{\mathrm{b},1} \ \varphi_{\mathrm{b},1} \ A_2 \ \tilde{f}_{\mathrm{b},2} \ \varphi_{\mathrm{b},2}]^T. \tag{A.16}$$

The resulting Fisher information matrix is given by

$$
[\mathbf{I}_{\mathrm{F}}(\boldsymbol{\theta})]_{\mathrm{ij}} = \frac{2}{\sigma^2}
\begin{bmatrix}
N_{\mathrm{s}} & 0 & 0 & \Re\left(\Upsilon\Psi_0\right) & \Re\left(j2\pi A_2 \Upsilon\Psi_1\right) & \Re\left(jA_2\Upsilon\Psi_0\right) \\
0 & 4\pi^2 A_1^2 \sum_{n=0}^{N_{\mathrm{s}}-1} n^2 & 2\pi A_1^2 \sum_{n=0}^{N_{\mathrm{s}}-1} n & \Re\left(-j2\pi A_1 \Upsilon\Psi_1\right) & \Re\left(4\pi^2 A_{12} \Upsilon\Psi_2\right) & \Re\left(2\pi A_{12}\Upsilon\Psi_1\right) \\
0 & 2\pi A_1^2 \sum_{n=0}^{N_{\mathrm{s}}-1} n & A_1^2 N_{\mathrm{s}} & \Re\left(-jA_1\Upsilon\Psi_0\right) & \Re\left(2\pi A_{12}\Upsilon\Psi_1\right) & \Re\left(A_{12}\Upsilon\Psi_0\right) \\
\Re\left(\Upsilon\Psi_0\right) & \Re\left(-j2\pi A_1 \Upsilon\Psi_1\right) & \Re\left(-jA_1\Upsilon\Psi_0\right) & N_{\mathrm{s}} & 0 & 0 \\
\Re\left(j2\pi A_2 \Upsilon\Psi_1\right) & \Re\left(4\pi^2 A_{12} \Upsilon\Psi_2\right) & \Re\left(2\pi A_{12}\Upsilon\Psi_1\right) & 0 & 4\pi^2 A_2^2 \sum_{n=0}^{N_{\mathrm{s}}-1} n^2 & 2\pi A_2^2 \sum_{n=0}^{N_{\mathrm{s}}-1} n \\
\Re\left(jA_2\Upsilon\Psi_0\right) & \Re\left(2\pi A_{12}\Upsilon\Psi_1\right) & \Re\left(A_{12}\Upsilon\Psi_0\right) & 0 & 2\pi A_2^2 \sum_{n=0}^{N_{\mathrm{s}}-1} n & A_2^2 N_{\mathrm{s}}
\end{bmatrix}. \tag{A.17}
$$

with $A_{12} = A_1 A_2$, $\Upsilon = \exp\big(j(\varphi_{\mathrm{b},2} - \varphi_{\mathrm{b},1})\big)$, $\Psi_0 = \sum_{n=0}^{N_\mathrm{s}-1} \exp\big(j2\pi(\tilde{f}_{\mathrm{b},2} - \tilde{f}_{\mathrm{b},1})\big)$, $\Psi_1 = \sum_{n=0}^{N_\mathrm{s}-1} n \exp\big(j2\pi(\tilde{f}_{\mathrm{b},2} - \tilde{f}_{\mathrm{b},1})\big)$, and $\Psi_2 = \sum_{n=0}^{N_\mathrm{s}-1} n^2 \exp\big(j2\pi(\tilde{f}_{\mathrm{b},2} - \tilde{f}_{\mathrm{b},1})\big)$.

The structure of the matrix remains unchanged in comparison to (A.6) and contains two submatrixes describing the influence of either the first or the second target. Only the cross-terms contain parameters from both targets and the frequency difference $\tilde{f}_{\mathrm{b},2} - \tilde{f}_{\mathrm{b},1}$ and phase difference $\varphi_{\mathrm{b},2} - \varphi_{\mathrm{b},1}$ determine the values of these terms.

The further symbolic derivation of the CRLB is skipped as it results in huge and hardly applicable equations due to the required matrix inversion of (A.18). Instead, a numerical consideration is given in Ch. 4.

A.1.3 CRLB for Dynamic Estimation

To describe target parameter estimation in a dynamic scenario, an extended signal model reflecting the signal dependencies of (2.7) is developed

$$\begin{aligned} s[n,m] =& A\exp\big(j(2\pi(\tilde{f}_{\mathrm{b},1}n + \tilde{f}_{\mathrm{b},2}n^2 + \tilde{f}_{\mathrm{b},3}m + \tilde{f}_{\mathrm{b},4}m^2 + \tilde{f}_{\mathrm{b},5}nm) + \varphi_\mathrm{b})\big) \\ &+ \omega[n,m], \\ &n \in [0, N_\mathrm{s}-1], m \in [0, N_\mathrm{c}-1], \end{aligned} \tag{A.18}$$

where A denotes the amplitude of the signal, φ_b the beat phase, all parameters $\tilde{f}_{\mathrm{b,x}} = \frac{f_{\mathrm{b,x}}}{f_\mathrm{s}}$ describe the fast- and slow-time signal behavior, and $\omega[n,m]$ is a complex WGN process with variance σ^2. Further, $N_\mathrm{s}, N_\mathrm{c} \gg 1$. The parameter vector $\boldsymbol{\theta}$ contains the parameters to be estimated

$$\boldsymbol{\theta} = [A\ \tilde{f}_{\mathrm{b},1}\ \tilde{f}_{\mathrm{b},2}\ \tilde{f}_{\mathrm{b},3}\ \tilde{f}_{\mathrm{b},4}\ \tilde{f}_{\mathrm{b},5}\ \varphi_\mathrm{b}]^T. \tag{A.19}$$

From this signal model, the CRLB derivation is equivalent to A.1.1 using the partial derivatives to determine the Fisher information matrix, which is subsequently inverted and yields lower bounds for the parameters in $\boldsymbol{\theta}$. Although all parameters are considered for the CRLB derivation, only three are used for radar-based target parameter estimation, which are $\tilde{f}_{\mathrm{b},1}$ and φ_b for range

estimation and $\tilde{f}_{\mathrm{b},3}$ for velocity estimation. A transformation of parameters yields

$$\begin{aligned}
\mathrm{var}(R_\mathrm{f}) &\gtrapprox \frac{c^2 N_\mathrm{s}^2}{4B^2} \cdot \mathrm{var}(\widehat{f}_{\mathrm{b},1}) \\
&= \frac{c^2 N_\mathrm{s}^2}{4B^2} \cdot \frac{3(N_\mathrm{c} + 30N_\mathrm{s} - 19N_\mathrm{c}N_\mathrm{s}^2 - 13N_\mathrm{s}^2 + 30N_\mathrm{c}N_\mathrm{s} - 23)}{2\pi^2 \eta N_\mathrm{c} N_\mathrm{s} (N_\mathrm{c}+1)(N_\mathrm{s}-1)(-N_\mathrm{s}^3 - N_\mathrm{s}^2 + 4N_\mathrm{s} + 4)} \\
&\approx \frac{57c^2 N_\mathrm{c} N_\mathrm{s}^4}{8\pi^2 B^2 \eta N_\mathrm{c}^2 N_\mathrm{s}^5} \\
&= \frac{57c^2}{8\pi^2 B^2 \eta N_\mathrm{c} N_\mathrm{s}},
\end{aligned} \tag{A.20}$$

$$\begin{aligned}
\mathrm{var}(R_\varphi) &\gtrapprox \frac{c^2}{(4\pi)^2 f_{\min}^2} \cdot \mathrm{var}(\widehat{\varphi}_\mathrm{b}) \\
&= \frac{c^2}{(4\pi)^2 f_{\min}^2} \\
&\cdot \frac{13N_\mathrm{c}^2 N_\mathrm{s}^2 + 12N_\mathrm{c}^2 N_\mathrm{s} + 2N_\mathrm{c}^2 + 12N_\mathrm{c}N_\mathrm{s}^2 - 27N_\mathrm{c}N_\mathrm{s} - 12N_\mathrm{c} + 2N_\mathrm{s}^2 - 12N_\mathrm{s} + 28}{\eta N_\mathrm{c} N_\mathrm{s} (N_\mathrm{c}^2 + 3N_\mathrm{c} + 2)(N_\mathrm{s}^2 + 3N_\mathrm{s} + 2)} \\
&\approx \frac{13c^2 N_\mathrm{c}^2 N_\mathrm{s}^2}{(4\pi)^2 f_{\min}^2 \eta N_\mathrm{c}^3 N_\mathrm{s}^3} \\
&= \frac{13c^2}{(4\pi)^2 f_{\min}^2 \eta N_\mathrm{c} N_\mathrm{s}},
\end{aligned} \tag{A.21}$$

and

$$\begin{aligned}\operatorname{var}(\widehat{v}) &\gtrapprox \frac{c^2 f_\mathrm{s}^2}{4 f_\mathrm{min}^2} \cdot \operatorname{var}(\widehat{f}_{\mathrm{b},3}) \\ &= \frac{c^2 f_\mathrm{s}^2}{4 f_\mathrm{min}^2} \cdot \frac{3(30N_\mathrm{c} + N_\mathrm{s} - 19N_\mathrm{c}^2 N_\mathrm{s} - 13N_\mathrm{c}^2 + 30N_\mathrm{c}N_\mathrm{s} - 23)}{2\pi^2 \eta N_\mathrm{c} N_\mathrm{s} (N_\mathrm{c} - 1)(N_\mathrm{s} + 1)(-N_\mathrm{c}^3 - N_\mathrm{c}^2 + 4N_\mathrm{c} + 4)} \\ &\approx \frac{57 c^2 f_\mathrm{s}^2 N_\mathrm{c}^2 N_\mathrm{s}}{8\pi^2 f_\mathrm{min}^2 \eta N_\mathrm{c}^5 N_\mathrm{s}^2} \\ &= \frac{57 c^2 f_\mathrm{s}^2}{8\pi^2 f_\mathrm{min}^2 \eta N_\mathrm{c}^3 N_\mathrm{s}},\end{aligned} \tag{A.22}$$

assuming $N_\mathrm{c}, N_\mathrm{s} \gg 1$, $c \gg v$, and $f_\mathrm{min} \gg \frac{B}{T}\frac{2R}{c}$. Additionally, only the largest term in the sums in numerator and denominator of $\operatorname{var}(\widehat{f}_{\mathrm{b},1})$, $\operatorname{var}(\widehat{\varphi}_\mathrm{b})$, and $\operatorname{var}(\widehat{f}_{\mathrm{b},3})$ is considered further.

Both R_f and v rely on a frequency analysis over the samples and the chirps respectively, mathematically obvious from the equivalence of $\operatorname{var}(\widehat{f}_{\mathrm{b},1})$ and $\operatorname{var}(\widehat{f}_{\mathrm{b},3})$. The bounds, however, differ in their dependencies, which is due to the deviant parameter transformation. For R_f and R_φ, similar dependencies can be observed as for a static scenario. B and f_min are the dominant influence factors, while N_c contributes in the same way as N_s.

A.1.4 CRLB including Doppler Tags

The above derivation of CRLBs for dynamic estimation can be transferred to the case of an artificial Doppler shift introduced to the signal model as in case of a Doppler tag. If a static scenario with no motion-induced Doppler shift is assumed, the signal model for one sideband simplifies to

$$\begin{aligned}s[n,m] =& A \exp\big(j(2\pi(\tilde{f}_{\mathrm{b},1} n + \tilde{f}_{\mathrm{b},3} m) + \varphi_\mathrm{b})\big) + \omega[n,m], \\ & n \in [0, N_\mathrm{s} - 1], m \in [0, N_\mathrm{c} - 1],\end{aligned} \tag{A.23}$$

with the parameter vector

$$\boldsymbol{\theta} = [A \ \tilde{f}_{\mathrm{b},1} \ \tilde{f}_{\mathrm{b},3} \ \varphi_\mathrm{b}]^T \tag{A.24}$$

and

$$\begin{aligned} f_{\mathrm{b},1} &= \frac{B}{T}\frac{2R}{c} + f_{\mathrm{id}} \\ f_{\mathrm{b},3} &= f_{\mathrm{id}} \\ \varphi_{\mathrm{b}} &= 2\pi\frac{2R}{c}\left(f_{\min} - \frac{f_{\mathrm{id}}}{2} - \frac{B}{2T}\frac{2R}{c}\right) \approx 2\pi\frac{2R}{c}f_{\min}. \end{aligned} \tag{A.25}$$

The relations for transformation of parameters follow to

$$\begin{aligned} R_{\mathrm{f}} &= \frac{cT}{2B}\left(f_{\mathrm{b},1} - f_{\mathrm{id}}\right) = \frac{cN_{\mathrm{s}}}{2B}\left(\tilde{f}_{\mathrm{b},1} - \frac{f_{\mathrm{id}}}{f_{\mathrm{s}}}\right) \\ R_{\varphi} &= \frac{c}{4\pi f_{\min}}\varphi_{\mathrm{b}} \\ v_{\mathrm{id}} &= \frac{c}{2f_{\min}}f_{\mathrm{id}} = \frac{c}{2f_{\min}}f_{\mathrm{b},3} = \frac{cf_{\mathrm{s}}}{2f_{\min}}\tilde{f}_{\mathrm{b},3}, \end{aligned} \tag{A.26}$$

where $\tilde{f}_{\mathrm{b},1} = \frac{f_{\mathrm{b},1}}{f_{\mathrm{s}}}$ and $\tilde{f}_{\mathrm{b},3} = \frac{f_{\mathrm{b},3}}{f_{\mathrm{s}}}$.

Again, the same structural derivation results in the CRLBs for the three parameters of interest

$$\begin{aligned} \mathrm{var}(R_{\mathrm{f}}) &\gtrapprox \frac{c^2N_{\mathrm{s}}^2}{4B^2}\cdot\mathrm{var}(\widehat{f}_{\mathrm{b},1}) \\ &= \frac{c^2N_{\mathrm{s}}^2}{4B^2}\cdot\frac{3}{2\pi^2\eta N_{\mathrm{c}}N_{\mathrm{s}}(N_{\mathrm{s}}+1)(N_{\mathrm{s}}-1)} \\ &\approx \frac{3c^2N_{\mathrm{s}}^2}{8\pi^2B^2\eta N_{\mathrm{c}}N_{\mathrm{s}}^3} \\ &= \frac{3c^2}{8\pi^2B^2\eta N_{\mathrm{c}}N_{\mathrm{s}}}, \end{aligned} \tag{A.27}$$

$$\begin{aligned}
\operatorname{var}(R_\varphi) &\gtrapprox \frac{c^2}{(4\pi)^2 f_{\mathrm{min}}^2} \cdot \operatorname{var}(\widehat{\varphi}_{\mathrm{b}}) \\
&= \frac{c^2}{(4\pi)^2 f_{\mathrm{min}}^2} \cdot \frac{N_{\mathrm{c}} + N_{\mathrm{s}} + 7N_{\mathrm{c}}N_{\mathrm{s}} - 5}{2\eta N_{\mathrm{c}}N_{\mathrm{s}}(N_{\mathrm{c}}+1)(N_{\mathrm{s}}+1)} \\
&\approx \frac{7c^2 N_{\mathrm{c}}N_{\mathrm{s}}}{2(4\pi)^2 f_{\mathrm{min}}^2 \eta N_{\mathrm{c}}^2 N_{\mathrm{s}}^2} \\
&= \frac{7c^2}{2(4\pi)^2 f_{\mathrm{min}}^2 \eta N_{\mathrm{c}}N_{\mathrm{s}}},
\end{aligned} \tag{A.28}$$

and

$$\begin{aligned}
\operatorname{var}(\widehat{v}_{\mathrm{id}}) &\gtrapprox \frac{c^2 f_{\mathrm{s}}^2}{4 f_{\mathrm{min}}^2} \cdot \operatorname{var}(\widehat{f}_{\mathrm{b},3}) \\
&= \frac{c^2 f_{\mathrm{s}}^2}{4 f_{\mathrm{min}}^2} \cdot \frac{3}{2\pi^2 \eta N_{\mathrm{c}}N_{\mathrm{s}}(N_{\mathrm{c}}+1)(N_{\mathrm{c}}-1)} \\
&\approx \frac{3c^2 f_{\mathrm{s}}^2}{8\pi^2 f_{\mathrm{min}}^2 \eta N_{\mathrm{c}}^3 N_{\mathrm{s}}},
\end{aligned} \tag{A.29}$$

assuming $N_{\mathrm{c}}, N_{\mathrm{s}} \gg 1$, $f_{\mathrm{min}} \gg \frac{B}{2T}\frac{2R}{c}$, and $f_{\mathrm{min}} \gg f_{\mathrm{id}}$.

The variance $\operatorname{var}(\widehat{v}_{\mathrm{id}})$ is given to allow for a direct comparison with the CRLBs derived for a dynamic scenario without Doppler tags in A.1.3. As expected, results only differ by constant factors from those in A.1.3, the same dependencies are found. Influences of the coupling and migration terms not occurring for artificial Doppler are weak also for motion-induced Doppler shifts and hence neglected in the derivation given in A.1.3.

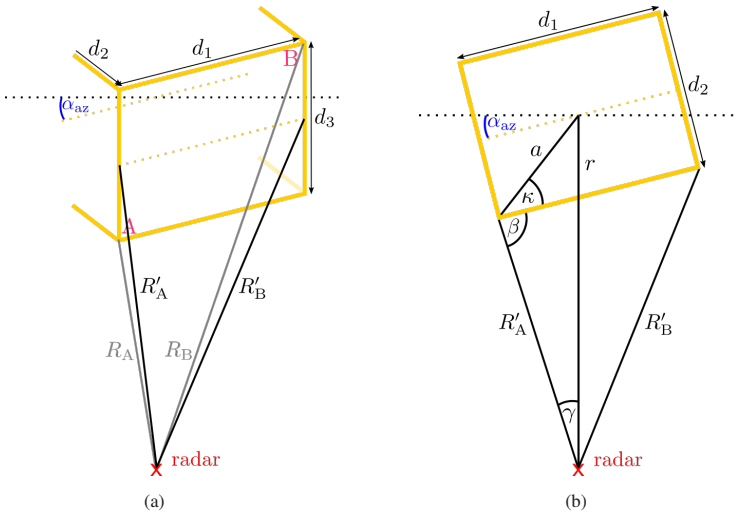

Figure A.1: Schematic delineation of orientation angle determination in 3D view (a) and as 2D section through (a) at $z = \frac{d_3}{2}$ (b). The azimuth orientation α_{az} is sought and determined using two Doppler tags A and B.

A.2 Radar-based Orientation Estimation Derivations

Azimuth orientation angle estimation is derived for a volume-centered setup with two Doppler tags A and B attached to diagonal corners of the object. In Fig. A.1a, dimensions d_1, d_2, and d_3 are preknown and R'_A and R'_B are determined from R_A and R_B according to

$$R'_A = \sqrt{R_A^2 - \left(\frac{d_3}{2}\right)^2}, \quad R'_B = \sqrt{R_B^2 - \left(\frac{d_3}{2}\right)^2}. \tag{A.30}$$

Considering Fig. A.1b, the azimuth orientation angle α_{az} is derived from β and γ to be

$$\alpha_{az} = \frac{\pi}{2} - (\pi - \beta - \gamma) = \beta + \gamma - \frac{\pi}{2}. \tag{A.31}$$

The auxiliary angles are determined from geometric interrelations as

$$\beta = \arccos\left(\frac{R_{\mathrm{B}}'^2 - R_{\mathrm{A}}'^2 - d_1^2}{-2R_{\mathrm{A}}' d_1}\right) \tag{A.32}$$

and

$$\gamma = \arcsin\left(\frac{\sin(\beta+\kappa)}{r}\cdot a\right), \tag{A.33}$$

where

$$a = \frac{\sqrt{d_1^2 + d_2^2}}{2}, \tag{A.34}$$

$$\kappa = \arccos\left(\frac{\frac{d_1}{2}}{a}\right), \tag{A.35}$$

and

$$r = \sqrt{a^2 + R_{\mathrm{A}}'^2 - 2aR_{\mathrm{A}}' cos(\beta+\kappa)}, \tag{A.36}$$

hence,

$$\gamma = \arcsin\left(\frac{\sin(\beta+\kappa)}{\sqrt{a^2 + R_{\mathrm{A}}'^2 - 2aR_{\mathrm{A}}'\cos(\beta+\kappa)}}\cdot a\right). \tag{A.37}$$

Orientation is herein determined mostly from one range estimate, R_{A} in this case, which has a larger influence on the estimation accuracy. However, two clearly visible tags are required for orientation estimation at all times. More detailed considerations on error influences are given in Ch. 7.2.

Bibliography

[AAZAK22] A. Alhaj Abbas, Y. Zantah, A. Abuelhaija, and T. Kaiser. Millimeter-Wave Retro-Directive Frequency Coded Lens by Curved One-Dimensional Photonic Crystal Resonator. *IEEE Access*, 10:132988–133000, 2022.

[AFM+13] M. Andres, P. Feil, W. Menzel, H.-L. Bloecher, and J. Dickmann. 3D detection of automobile scattering centers using UWB radar sensors at 24/77 GHz. *IEEE Aerospace and Electronic Systems Magazine*, 28(3):20–25, 2013.

[Ala25] M. B. Alabd. *Communication and Synchronization Schemes for Chirp Sequence-based Automotive Radar Systems*. KIT Scientific Publishing, Karlsruhe, Nov 2025.

[AOJRT24] M. F. R. Al-Okby, S. Junginger, T. Roddelkopf, and K. Thurow. UWB-Based Real-Time Indoor Positioning Systems: A Comprehensive Review. *Applied Sciences*, 14(23), 2024.

[APK+11] S. Ayhan, M. Pauli, T. Kayser, S. Scherr, and T. Zwick. FMCW radar system with additional phase evaluation for high accuracy range detection. In *2011 8th European Radar Conference*, pages 117–120, 2011.

[ASB+15] S. Ayhan, S. Scherr, A. Bhutani, M. Pauli, and T. Zwick. Radar Sensor for Waveguide based Distance Measurements in Machine Tool Components. In *2015 IEEE MTT-S International Conference on Microwaves for Intelligent Mobility (ICMIM)*, pages 1–4, 2015.

[BASP+24] A. Batra, A. A. Abbas, J. Sánchez-Pastor, M. El-Absi, A. Jiménez-Sáez, M. Khaliel, J. Barowski, M. Wiemeler, D. Göhringer, I. Rolfes, R. Jakoby, and T. Kaiser. Millimeter Wave Indoor SAR Sensing Assisted With Chipless Tags-Based Self-Localization System: Experimental Evaluation. *IEEE Sensors Journal*, 24(1):844–857, 2024.

[BCL+14] I. Bisio, M. Cerruti, F. Lavagetto, M. Marchese, M. Pastorino, A. Randazzo, and A. Sciarrone. A Trainingless WiFi Fingerprint Positioning Approach Over Mobile Devices. *IEEE Antennas and Wireless Propagation Letters*, 13:832–835, 2014.

[BD03] R. Bruno and F. Delmastro. Design and Analysis of a Bluetooth-Based Indoor Localization System. In *IFIP International Conference on Personal Wireless Communications*, 2003.

[Ble00] G. Blewitt. Basics of the GPS Technique : Observation Equations. 2000.

[BSCB04] P. Bidigare, T. Stevens, B. Correll, and M. Beauvais. Minimum radar cross section bounds for passive radar responsive tags. In *Conference Record of the Thirty-Eighth Asilomar Conference on Signals, Systems and Computers, 2004.*, volume 2, pages 1441–1445 Vol.2, 2004.

[CB04] B.G. Colpitts and G. Boiteau. Harmonic radar transceiver design: miniature tags for insect tracking. *IEEE Transactions on Antennas and Propagation*, 52(11):2825–2832, 2004.

[COTKR15] I. Cnaan-On, S. J. Thomas, J. L. Krolik, and M. S. Reynolds. Multichannel Backscatter Communication and Ranging for Distributed Sensing With an FMCW Radar. *IEEE Transactions on Microwave Theory and Techniques*, 63(7):2375–2383, 2015.

[DAMC+15] A. De Angelis, A. Moschitta, P. Carbone, M. Calderini, S. Neri, R. Borgna, and M. Peppucci. Design and Characterization of a Portable Ultrasonic Indoor 3-D Positioning System. *IEEE Transactions on Instrumentation and Measurement*, 64(10):2616–2625, 2015.

[DDG+18] Y. Dobrev, Y. Dobrev, P. Gulden, M. Lipka, T. Pavlenko, D. Moormann, and M. Vossiek. Radar-Based High-Accuracy 3D Localization of UAVs for Landing in GNSS-Denied Environments. In *2018 IEEE MTT-S International Conference on Microwaves for Intelligent Mobility (ICMIM)*, pages 1–4, 2018.

[DFV16] Y. Dobrev, S. Flores, and M. Vossiek. Multi-modal sensor fusion for indoor mobile robot pose estimation. In *2016 IEEE/ION Position, Location and Navigation Symposium (PLANS)*, pages 553–556, 2016.

[DHC+17] M. S. Dadash, J. Hasch, P. Chevalier, A. Cathelin, N. Cahoon, and S. P. Voinigescu. Design of Low-Power Active Tags for Operation With 77–81-GHz FMCW Radar. *IEEE Transactions on Microwave Theory and Techniques*, 65(12):5377–5388, 2017.

[DVC+17] Y. Dobrev, M. Vossiek, M. Christmann, I. Bilous, and P. Gulden. Steady Delivery: Wireless Local Positioning Systems for Tracking and Autonomous Navigation of Transport Vehicles and Mobile Robots. *IEEE Microwave Magazine*, 18(6):26–37, 2017.

[Eld04] Y.C. Eldar. Minimum variance in biased estimation: bounds and asymptotically optimal estimators. *IEEE Transactions on Signal Processing*, 52(7):1915–1930, 2004.

[Fit74] R. J. Fitzgerald. Effects of Range-Doppler Coupling on Chirp Radar Tracking Accuracy. *IEEE Transactions on Aerospace and Electronic Systems*, AES-10(4):528–532, 1974.

[FJ98] M. Frigo and S.G. Johnson. FFTW: an adaptive software architecture for the FFT. In *Proceedings of the 1998 IEEE International Conference on Acoustics, Speech and Signal Processing, ICASSP '98 (Cat. No.98CH36181)*, volume 3, pages 1381–1384 vol.3, 1998.

[FPEA+18] X. Fu, A. Pedross-Engel, D. Arnitz, C. M. Watts, A. Sharma, and M. S. Reynolds. Simultaneous Imaging, Sensor Tag Localization, and Backscatter Uplink via Synthetic Aperture Radar. *IEEE Transactions on Microwave Theory and Techniques*, 66(3):1570–1578, 2018.

[GDBCV21] A. Garcia-Devesa, M. A. Baez-Chorro, and B. Vidal. Comparison of computing efficiency among FFT, CZT and Zoom FFT in THz-TDS, 2021.

[Göb01] J. Göbel. *Radartechnik: Grundlagen und Anwendungen*. VDE-Verlag, 2001.

[GSBLL13] X. Gao, A. Singh, O. Boric-Lubecke, and V. M. Lubecke. Small-scale Displacement Measurement with Passive Harmonic RF Tag using Doppler Radar. In *2013 IEEE International Wireless Symposium (IWS)*, pages 1–4, 2013.

[HBBP21] S. Hansen, C. Bredendiek, G. Briese, and N. Pohl. A Compact Harmonic Radar System With Active Tags at 61/122 GHz ISM

Band in SiGe BiCMOS for Precise Localization. *IEEE Transactions on Microwave Theory and Techniques*, 69(1):906–915, 2021.

[Hül04a] C. Hülsmeyer. Verfahren, um metallische Gegenstände mittels elektrischer Wellen einem Beobachter zu melden. *Patent DE 165546*, 1904.

[Hül04b] C. Hülsmeyer. Verfahren zur Bestimmung der Entfernung von metallischen Gegenständen (Schiffen o. dgl.), deren Gegenwart durch das Verfahren nach Patent 165546 festgestellt wird. *Patent DE 169154*, 1904.

[IEE85] IEEE Standard for Binary Floating-Point Arithmetic. *ANSI/IEEE Std 754-1985*, pages 1–20, 1985.

[ISN+23] T. Iizuka, T. Sasatani, T. Nakamura, N. Kosaka, M. Hisada, and Y. Kawahara. MilliSign: MmWave-Based Passive Signs for Guiding UAVs in Poor Visibility Conditions. In *Proceedings of the 29th Annual International Conference on Mobile Computing and Networking*, ACM MobiCom '23, New York, NY, USA, 2023. Association for Computing Machinery.

[ISO94] Accuracy (trueness and precision) of measurement methods and results — Part 1: General principles and definitions (ISO 5725-1:1994). Standard, International Organization for Standardization., Geneva, CH, 1994.

[JLSV+23] M. Joshi, C. Lynch, G. Soto-Valle, A. Adeyeye, R. Bahr, and M. Tentzeris. Machine Learning-Enhanced Gyro mmID-Sensor for Virtual Reality and Motion Tracking Applications. In *2023 20th European Radar Conference (EuRAD)*, pages 127–130, 2023.

[JRM10] J. A. Jackson, B. D. Rigling, and R. L. Moses. Canonical Scattering Feature Models for 3D and Bistatic SAR. *IEEE Transactions on Aerospace and Electronic Systems*, 46(2):525–541, 2010.

[JSSEA+20] A. Jiménez-Sáez, M. Schüßler, M. El-Absi, A. A. Abbas, K. Solbach, T. Kaiser, and R. Jakoby. Frequency Selective Surface Coded Retroreflectors for Chipless Indoor Localization Tag Landmarks. *IEEE Antennas and Wireless Propagation Letters*, 19(5):726–730, 2020.

[Kay93] S. M. Kay. *Fundamentals of Statistical Signal Processing: Estimation Theory*. Prentice-Hall, Inc., USA, 1993.

[KBK+15] D. Kellner, M. Barjenbruch, J. Klappstein, J. Dickmann, and K. Dietmayer. Wheel extraction based on micro doppler distribution using high-resolution radar. In *2015 IEEE MTT-S International Conference on Microwaves for Intelligent Mobility (ICMIM)*, pages 1–4, 2015.

[KHJH88] Y.S. Kwoh, J. Hou, E.A. Jonckheere, and S. Hayati. A robot with improved absolute positioning accuracy for CT guided stereotactic brain surgery. *IEEE Transactions on Biomedical Engineering*, 35(2):153–160, 1988.

[KXW22] W. Kang, S. Xu, and W. Wu. Time-Division Multiple Tags Based Multitarget Respiration Monitoring Radar With a Single Beam. *IEEE Microwave and Wireless Components Letters*, 32(2):181–184, 2022.

[LJLC17] B. Liu, M. Jian, Z. Lu, and R. Chen. Indoor monitoring human movements using dual-receiver radar. In *2017 IEEE Radar Conference (RadarConf)*, pages 0520–0523, 2017.

[Lud98] A. Ludloff. *Praxiswissen Radar und Radarsignalverarbeitung*. Vieweg+Teubner Verlag, Wiesbaden, 1998.

[MKV11] R. Miesen, F. Kirsch, and M. Vossiek. Holographic localization of passive UHF RFID transponders. In *2011 IEEE International Conference on RFID*, pages 32–37, 2011.

[MT11] R. Mautz and S. Tilch. Survey of optical indoor positioning systems. In *2011 International Conference on Indoor Positioning and Indoor Navigation*, pages 1–7, 2011.

[NHS24] A. A. Nargund, A. Huard, and M. Sra. WaveWalker: Enabling Outdoor VR Experiences with Millimeter-wave RADAR. In *2024 IEEE International Symposium on Mixed and Augmented Reality Adjunct (ISMAR-Adjunct)*, pages 509–512, 2024.

[NVN20] N. Nourshamsi, S. Vakalis, and J. A. Nanzer. Joint Detection of Human and Object Motion Using Harmonic Micro-Doppler Radar and Harmonic Tags. *IEEE Antennas and Wireless Propagation Letters*, 19(6):930–934, 2020.

[PG01] P.F. Pellegrini and E. Giannini. Determinations of aircraft position and orientation from images of a millimetric surface

radar. In *Proceedings of the 2001 IEEE Radar Conference (Cat. No.01CH37200)*, pages 457–461, 2001.

[PKJP22] L. Piotrowsky, S. Kueppers, T. Jaeschke, and N. Pohl. Distance Measurement Using mmWave Radar: Micron Accuracy at Medium Range. *IEEE Transactions on Microwave Theory and Techniques*, 70(11):5259–5270, 2022.

[PLK12] F. Puente León and U. Kiencke. *Messtechnik : Systemtheorie für Ingenieure und Informatiker*. Springer Vieweg, 9th edition edition, 2012.

[PMC+08] D. Psychoudakis, W. Moulder, C.-C. Chen, H. Zhu, and J. L. Volakis. A Portable Low-Power Harmonic Radar System and Conformal Tag for Insect Tracking. *IEEE Antennas and Wireless Propagation Letters*, 7:444–447, 2008.

[RKDW16] F. Roos, D. Kellner, J. Dickmann, and C. Waldschmidt. Reliable Orientation Estimation of Vehicles in High-Resolution Radar Images. *IEEE Transactions on Microwave Theory and Techniques*, 64(9):2986–2993, 2016.

[RSH10] M. A. Richards, J. A. Scheer, and W. A. Holm. *Principles of Modern Radar: Basic principles*. The Institution of Engineering and Technology, 2010.

[RSV15] C. Reustle, D. Shmakov, and M. Vossiek. A 24 GHz SIMO radar tachymeter for precise transponder localization. In *2015 IEEE MTT-S International Microwave Symposium*, pages 1–4, 2015.

[SAPZ12] S. Scherr, S. Ayhan, M. Pauli, and T. Zwick. Accuracy limits of a K-band FMCW radar with phase evaluation. In *2012 9th European Radar Conference*, 2012.

[SBH+22] M. Stelzig, A. Benedikter, R. Horn, M. Jäger, M. Keller, R. Scheiber, G. Krieger, and M. Vossiek. Virtual Synthetic Aperture Radar Target Based on a Miniaturized Monostatic Digital Delay Transponder. *IEEE Microwave and Wireless Components Letters*, 32(3):249–252, 2022.

[Sch17] S. Scherr. *FMCW-Radarsignalverarbeitung zur Entfernungsmessung mit hoher Genauigkeit*. KIT Scientific Publishing, Karlsruhe, Mar 2017.

[SDCV18] Martin Schtz, Yassen Dobrev, Christian Carlowitz, and Martin Vossiek. Wireless Local Positioning with SILO-Based Backscatter Transponders for Autonomous Robot Navigation. In *2018 IEEE MTT-S International Conference on Microwaves for Intelligent Mobility (ICMIM)*, pages 1–4, 2018.

[SDM14] S. Sand, A. Dammann, and C. Mensing. *Positioning in Wireless Communications Systems*. Wiley, Hoboken, 2014.

[SE11] A. Strobel and F. Ellinger. An active pulsed reflector circuit for FMCW radar application based on the switched injection-locked oscillator principle. In *2011 Semiconductor Conference Dresden*, pages 1–4, 2011.

[SFH+17] W. Scheiblhofer, R. Feger, A. Haderer, S. Scheiblhofer, and A. Stelzer. Simultaneous localization and data-interrogation using a 24-GHz modulated-reflector FMCW radar system. In *2017 IEEE MTT-S International Microwave Symposium (IMS)*, pages 67–70, 2017.

[SHK+21] E. Sippel, M. Hehn, T. Koegel, P. Gröschel, A. Hofmann, S. Brückner, J. Geiss, R. Schober, and M. Vossiek. Quasi-Coherent Phase-Based Localization and Tracking of Incoherently Transmitting Radio Beacons. *IEEE Access*, 9:133229–133239, 2021.

[SIC24] SICK AG. *Product Data Sheet KTS-WB9114115AZZZZ*, 2024.

[SIR24] A. Sesyuk, S. Ioannou, and M. Raspopoulos. Radar-Based Millimeter-Wave Sensing for Accurate 3-D Indoor Positioning: Potentials and Challenges. *IEEE Journal of Indoor and Seamless Positioning and Navigation*, 2:61–75, 2024.

[SL10] A. Singh and V. Lubecke. A Heterodyne Receiver for Harmonic Doppler Radar Cardiopulmonary Monitoring with Body-worn Passive RF Tags. In *2010 IEEE MTT-S International Microwave Symposium*, pages 1600–1603, 2010.

[SLY+21] H.-H. Sun, Y. H. Lee, A. C. Yucel, G. Ow, and M. L. M. Yusof. Elongated Object Orientation Estimation Based on Deep Neural Networks. In *2021 IEEE International Symposium on Antennas and Propagation and USNC-URSI Radio Science Meeting (APS/URSI)*, pages 1998–1999, 2021.

[SM90] P. Stoica and R. L. Moses. On Biased Estimators and the Unbiased Cramér-Rao Lower Bound. *Signal Process.*, 1990.

[SN11] S. S. Saab and Z. S. Nakad. A Standalone RFID Indoor Positioning System Using Passive Tags. *IEEE Transactions on Industrial Electronics*, 58(5):1961–1970, 2011.

[SRB+07] A. D. Semenov, H. Richter, U. Bottger, A. V. Smirnov, and H.-W. Hubers. Distant Detection of Hidden Objects with a THz Imaging Radar. In *2007 Joint 32nd International Conference on Infrared and Millimeter Waves and the 15th International Conference on Terahertz Electronics*, pages 652–653, 2007.

[SSSW17] J. Schlichenmaier, N. Selvaraj, M. Stolz, and C. Waldschmidt. Template matching for radar-based orientation and position estimation in automotive scenarios. In *2017 IEEE MTT-S International Conference on Microwaves for Intelligent Mobility (ICMIM)*, pages 95–98, 2017.

[TE00] J. Thornton and D.J. Edwards. Range measurement using modulated retro-reflectors in FM radar system. *IEEE Microwave and Guided Wave Letters*, 10(9):380–382, 2000.

[Tex20] Texas Instruments Incorporated. *mmWave Radar Interface Control Document*, 2020.

[UC14] G. Upton and I. Cook. *Oxford Dictionary of Statistics*. Oxford University Press, 3rd edition edition, 2014.

[VG08] M. Vossiek and P. Gulden. The Switched Injection-Locked Oscillator: A Novel Versatile Concept for Wireless Transponder and Localization Systems. *IEEE Transactions on Microwave Theory and Techniques*, 56(4):859–866, 2008.

[VRH99] M. Vossiek, R. Roskosch, and P. Heide. Precise 3-D Object Position Tracking using FMCW Radar. In *1999 29th European Microwave Conference*, volume 1, pages 234–237, 1999.

[VS20] P. Vaishnav and A. Santra. Continuous Human Activity Classification With Unscented Kalman Filter Tracking Using FMCW Radar. *IEEE Sensors Letters*, 4(5):1–4, 2020.

[VWG+03] M. Vossiek, L. Wiebking, P. Gulden, J. Wieghardt, C. Hoffmann, and P. Heide. Wireless local positioning. *IEEE Microwave Magazine*, 4(4):77–86, 2003.

[WBG25] C. Waldschmidt, C. Bonfert, and T. Grebner. *Millimeter Wave Radar*. Springer Nature Switzerland, 2025.

[Whi15] E. T. Whittaker. XVIII.—On the Functions which are represented by the Expansions of the Interpolation-Theory. *Proceedings of the Royal Society of Edinburgh*, 35:181–194, 1915.

[WMB+93] F.R. Williamson, L.F. Moore, R. Brooks, J.A. Williamson, and M.C. McGee. A Coded Radar Reflector for Remote Identification of Personnel and Vehicles. In *The Record of the 1993 IEEE National Radar Conference*, pages 186–191, 1993.

[WMM93] G.S. Woods, D.L. Maskell, and M.V. Mahoney. A high accuracy microwave ranging system for industrial applications. *IEEE Transactions on Instrumentation and Measurement*, 42(4):812–816, 1993.

[WZZ+21] X. Wang, Z. Zhang, N. Zhao, Y. Zhang, and D. Huang. Indoor Localization and Trajectory Tracking System based on Millimeter-Wave Radar Sensor. In *2021 IEEE 10th Data Driven Control and Learning Systems Conference (DDCLS)*, pages 1141–1147, 2021.

Own Publications

Journal Articles

[1] **Antes, Theresa**; Backes, A.; Zwick, T.; Nuss, B.: Radar-Based 3-D Spatial Estimation Using Uniquely Identifiable Doppler Tags. In: *IEEE Transactions on Radar Systems* 4 (2026), S. 525–534

[2] **Antes, Theresa**; Schubert, P.; Zwick, T.; Nuss, B.: Identification and High-Accuracy Range Estimation With Doppler Tags in Radar Applications. In: *IEEE Transactions on Radar Systems* 3 (2025)

[3] Bekker, E.; Gramlich, G.; Valenziano, L.; Oliveira, L. G.; **Antes, Theresa**; Zwick, T.; Bhutani, A.: Broadband packaging solution in embedded wafer level ball grid array technology for D-band PMCW radar. In: *International Journal of Microwave and Wireless Technologies* 16 (2024)

[4] Longo, J. P. N.; Galvão, J. R.; **Antes, Theresa**; Santos, E. N.; Silva, J. C. C.; Martelli, C.; Sum, A. K.; Morales, R. E. M.; Silva, M. J.: Sensing Hydrates in Pipes by a Combined Electrical and Optical Fiber Sensor. In: *IEEE Sensors Journal* 20 (2020)

[5] Oliveira, L. Giroto d.; Bekker, E.; Bhutani, A.; Diewald, A.; Nuss, B.; **Antes, Theresa**; Zwick, T.: Doppler Shift Tolerance of Accumulation and Outer Coding in MIMO-PMCW Radar. In: *IEEE Microwave and Wireless Components Letters* 32 (2022)

[6] Oliveira, L. Giroto d.; Nuss, B.; Alabd, M. B.; Diewald, A.; Li, Y.; Gehre, L.; Long, X.; **Antes, Theresa**; Galinsky, J.; Zwick, T.: Discrete-Fresnel Domain Channel Estimation in OCDM-Based Radar Systems. In: *IEEE Transactions on Microwave Theory and Techniques* 71 (2023)

Conference Contributions

[7] **Antes, Theresa**; Bekker, E.; Bhutani, A.; Zwick, T.: A Flexible Data Set for Radar-Based Gesture Recognition. In: *2025 16th German Microwave Conference (GeMiC)*, 2025

[8] **Antes, Theresa**; De Oliveira, L. G.; Diewald, A.; Bekker, E.; Bhutani, A.; Zwick, T.: Velocities in Human Hand Gestures for Radar-based Gesture Recognition Applications. In: *2023 IEEE Radar Conference (RadarConf23)*, 2023

[9] **Antes, Theresa**; Kollár, Z.; Zwick, T.; Nuss, B.: Doppler-Robust High-Accuracy Range Estimation for FC-FMCW Radar. In: *2024 21st European Radar Conference (EuRAD)*, 2024

[10] **Antes, Theresa**; Kollár, Z.; Zwick, T.; Nuss, B.: High-Accuracy Range Estimation for FC-FMCW Radar Using Phase Evaluation in Static Scenarios. In: *2024 IEEE Radar Conference (RadarConf24)*, 2024

[11] **Antes, Theresa**; Oliveira, L. G.; Bekker, E.; Bhutani, A.; Zwick, T.: Doppler Robustness Analysis of Orthogonal Sequences for MIMO PMCW Radar. In: *2022 23rd International Radar Symposium (IRS)*, 2022

[12] **Antes, Theresa**; Zwick, T.; Nuss, B.: Multi-Object Identification and High-Accuracy Range Estimation Using Doppler Tags. In: *2025 22nd European Radar Conference (EuRAD)*, 2025

[13] **Antes, Theresa**; Zwick, T.; Nuss, B.: On the Accuracy of Range Estimation with Doppler Influence in FC-FMCW: Benefits and Limitations. In: *2025 IEEE Radio and Wireless Symposium (RWS)*, 2025

[14] **Antes, Theresa**; Zwick, T.; Nuss, B.: Characterizing Doppler Tags for Moving Object Identification and Range and Velocity Estimation. In: *2026 17th German Microwave Conference (GeMiC)*, 2026

[15] Bekker, E.; Bhutani, A.; Oliveira, L. G.; **Antes, Theresa**; Zwick, T.: Broadband Split Ring Resonator-Based Antennas at 140 GHz in Embedded Wafer Level Ball Grid Array Technology. In: *2022 International Workshop on Antenna Technology (iWAT)*, 2022

[16] Bekker, E.; Bhutani, A.; Oliveira, L. G.; **Antes, Theresa**; Zwick, T.: Differential Split-Ring Resonator-Based Antenna at 140 GHz in Embedded Wafer Level Ball Grid Array Technology. In: *2022 52nd European Microwave Conference (EuMC)*, 2022

[17] Diewald, A.; **Antes, Theresa**; Nuss, B.; Pauli, M.; Zwick, T.: Range Doppler Migration Synthesis for Realistic Radar Target Simulation. In: *2021 IEEE Topical Conference on Wireless Sensors and Sensor Networks (WiSNeT)*, 2021

[18] Diewald, A.; **Antes, Theresa**; Nuss, B.; Zwick, T.: Implementation of Range Doppler Migration Synthesis for Radar Target Simulation. In: *2021 IEEE 93rd Vehicular Technology Conference (VTC2021-Spring)*, 2021

[19] Klumpp, C.; **Antes, Theresa**; Zwick, T.; Nuss, B.: DoA-supported Trilateration for Position Estimation with Doppler Tags. In: *2026 17th German Microwave Conference (GeMiC)*, 2026

[20] Oliveira, L. G.; Bekker, E.; Diewald, A.; Nuss, B.; **Antes, Theresa**; Li, Y.; Bhutani, A.; Zwick, T.: Enabling Joint Radar-Communication Operation in Shift Register-Based PMCW Radars. In: *2023 20th European Radar Conference (EuRAD)*, 2023